Study of preplasma properties using time-resolved reflection spectroscopy

Dissertation

zur Erlangung des akademischen Grades

Doctor rerum naturalium (Dr. rer. nat.)

FRIEDRICH-SCHILLER-
UNIVERSITÄT
JENA

---

vorgelegt dem Rat der

Physikalisch-Astronomischen Fakultät

der Friedrich-Schiller-Universität Jena

von M. Sc. Johannes Franz Andreas Hornung

geboren am 11.05.1991 in Aschaffenburg

Gutachter

1. **Prof. Dr. Matt Zepf**
   Institut für Optik und Quantenelektronik
   Friedrich-Schiller-Universität Jena
   Helmholtz-Institut Jena

2. **Prof. Dr. Ulrich Schramm**
   Institut für Strahlenphysik
   Helmholtz-Zentrum Dresden-Rossendorf

3. **Dr. Patrick Audebert**
   Laboratoire pour l'Utilisation des Lasers Intenses
   Ecole Polytechnique

Tag der Disputation: 01.07.2021

Zusammenfassung

Seit den ersten Experimenten zur Laserionenbeschleunigung wurden viele, immer komplexere Mechanismen, auf der Grundlage von theoretischen Überlegungen mit der Unterstützung von numerischen Simulationen vorhergesagt. Ein zentraler Punkt für diese Mechanismen ist die Existenz einer optimalen Targetdicke, wobei die Toleranz dieser Dicke verhältnismäßig klein ist. Diese Mechanismen sollten im Labor mit dem derzeitgen Entwicklungsstand moderner Lasersysteme experimentell zugänglich sein. Allerdings gibt es immer noch eine hohe Diskrepanz zwischen den simulierten Erwartungswerten und den tatsächlich unter experimentellen Bedingungen erreichten Resultaten. Eine mögliche Erklärung könnte der in der Regel unbekannte Zustand und die große räumliche Ausdehnung des sogenannten Vorplasmas liefern, welcher unter dem Einfluss des Lasers vor dem Erreichen der maximalen Laserintensität entsteht. Die präzise Bestimmung dieses Zustands, auf einer Zeitskala von wenigen Pikosekunden vor dem Eintreffen des Laserpulsmaximums, stellt eine große Herausforderung dar. Diese Problematik wird zudem verschärft da die zur Verfügung stehenden Diagnostiken nur Messungen eines räumlich sehr weit ausgedehnten Plasmas zulassen, oder die Verfügbarkeit eines Kurzpulslasers im Femtosekunden Bereich voraussetzen.
Die Schließung dieser Messlimitierung und somit die Erweiterung des messbaren Bereichs mittels einer neu entwickelten Methode war Ziel dieser Arbeit. Eine Möglichkeit dafür bietet die zeitaufgelöste Messung des am Vorplasma reflektierten Laserpulses. Dessen spektrale Veränderung mit der Zeit kann dabei auf die Bewegung des Ortes der kritischen Plasmadichte zurückgeführt werden, welche zu einem Dopplereffekt führt. Diese Informationen können mit den Vorplasmaeigenschaften korreliert werden, welche zu Beginn der Wechselwirkung vorliegen.
Zur Untersuchung dieser Korrelation wurden 2D “particle-in-cell“(PIC) Simulationen zu verschiedenen Laser- und Plasmaparametern durchgeführt. Dabei wurde ein Zusammenhang zwischen der Blauverschiebung des Spektrums am zeitlichen Anfang des Laserpulses und der Expansion des Plasmas bzw. dessen Temperatur gefunden. Außerdem konnte eine Aussage über den vorliegenden Dichtegradienten des Vorplasmas, die sogenannte Skalenlänge, getroffen werden. Diese konnte mit der Beschleunigung des Reflexionspunktes in das Plasma zu Beginn der Interaktion in Verbindung gebracht werden, welche sich durch steigende Laserintensitäten und Skalenlängen erhöht. Diese Korrelation stimmt außerdem sehr gut mit einer analytischen Beschreibung der Bewegung des Reflexionspunktes überein, welche entwickelt wurde um den Einfluss der Vorplasma-Skalenlänge zu berücksichtigen. Diese Beschreibung kann außerdem genutzt werden um die maximale Rotverschiebung des Spektrums vorherzusagen, welche daraufhin einen experimentellen Zugang zur Abschätzung der Vorplasma-Skalenlänge ermöglicht.

Zur Überprüfung dieser Methode wurden zwei experimentelle Kampagnen am Petawatt High-Energy Laser for Heavy-Ion eXperiments (PHELIX) der GSI Helmholtzzentrum für Schwerionenforschung GmbH durchgeführt, welcher Laserenergien von bis zu 200 J liefert und eine Pulsdauer von 500 fs besitzt. In diesen wurden der zeitliche Kontrast mithilfe sogenannter Plasmaspiegel verbessert, um die Bildung des Vorplasmas zu unterdrücken. Die dadurch entstehenden Effekte auf den rückreflektierten Laserpuls wurden mit zeitauflösenden und zeitintegrierenden Diagnostiken untersucht.
Dabei konnten diverse Resultate der numerischen Simulationen bestätigt werden. Im Bezug auf die zeitintegrierten Messungen zeigte eine Verbesserung des Kontrastes eine Blauverschiebung des gesamten Spektrums, im Vergleich zu einer Rotverschiebung ohne Plasmaspiegel. Durch den Vergleich der maximalen Rotverschiebung des Spektrums mit den Ergebnissen der gefundenen analytischen Beschreibung konnte die Skalenlänge des Vorplasmas auf (0.18 ± 0.11) µm and (0.83 ± 0.39) µm für den Fall mit und ohne Plasmaspiegel bestimmt werden.
Es wurde gezeigt, dass diese Messmethode eine vielversprechende neue Möglichkeit darstellt, um die Vorplasmaeigenschaften vor dem Eintreffen der Maximalintensität, auf nichtinvasive Art, zu messen. Im Rahmen dieser Arbeit wurde damit eine Messung des Plasmazustandes, einigen Pikosekunden vor dem Eintreffen der Maximalintensität, demonstriert. Zukünftig kann dies, durch eine Erhöhung des dynamischen Bereichs, weiter verbessert werden.
Des weiteren wurden zwei zusätzliche experimentelle Kampagnen zur Verbesserung der Laserionenbeschleunigung am Lasersystem PHELIX durchgeführt, um höhere Protonenenergien und Teilchenzahlen zu erhalten. In diesen wurde zum einen die Absorption der Laserenergie in dem Target bei einem Einfallswinkel von 45° mittels verschiedener Methoden erhöht. Die besten Ergebnisse wurden dabei durch die Änderung der Laserpolarisation von s- auf p-Polarisation erhalten, wobei die Targetdicke so dünn wie möglich gewählt wurde ohne in den Bereich der Transparenz zu kommen. Zum anderen wurde durch die Erhöhung der Laserintensität im Breich von 8×10^{20} W/cm^2 eine maximale Protonenenergie von bis zu 93 MeV erreicht, wodurch ein neuer Rekord in Bezug auf das PHELIX-System erzielt wurde.

Abstract

Since the first experiments on laser-ion acceleration, many increasingly sophisticated mechanisms have been predicted on the basis of numerical simulations. A key issue for these mechanisms is the existence of an optimal target thickness, whereas the tolerance of this thickness is relatively small. These mechanisms should be achievable with the properties of modern laser systems. However, there is still a large discrepancy between the predicted results and those actually reached in experimental conditions. A possible explanation could be the usually unknown state and extent of the so-called preplasma, which is formed before the maximum laser intensity reaches the target. To diagnose this state on a time scale of a few picoseconds prior to the arrival of the laser pulse is a major challenge, especially since the currently available diagnostics can only be used for a very long spatial extent of the preplasma, or require the availability of a short-pulse laser in the femtosecond regime.

Therefore, the aim of this work was to develop a new method that extends the measurable range. One possibility is the time-resolved measurement of the laser pulse reflected by the plasma during the interaction. Its spectral change over time can be attributed to the motion of the critical-density position of the plasma, which results in a Doppler shift of the laser pulse. This information can be correlated with the preplasma properties that are present at the beginning of the interaction.

This dependence is investigated with 2-D particle-in-cell (PIC) simulations, by varying the laser and plasma parameters. These simulations show a correlation between the blue shift of the spectrum at the temporal beginning of the laser pulse and the expansion velocity of the preplasma, which can be used to derive the corresponding electron temperature.

In addition, a statement about the present density gradient of the preplasma, the so-called scale length, is possible. The acceleration of the reflection point into the plasma, at the beginning of the interaction, increases for higher laser intensities and longer scale lengths. The same correlation is given by an analytical description of the holeboring velocity and acceleration, which has been derived to include the effect of the preplasma scale length. This description can also be used to predict the maximum red shift of the spectrum, which enables the possibility to estimate the scale length of the preplasma with a time-integrated measurement.

To verify this method, two experimental campaigns were performed at the Petawatt High-Energy Laser for Heavy-Ion eXperiments (PHELIX) at the GSI Helmholtzzentrum für Schwerionenforschung GmbH, which is able to reach laser pulse energies up to 200 J with a pulse duration of 500 fs. The temporal contrast was enhanced using so-called plasma mirrors to suppress the formation of the preplasma. The resulting effects on the laser

pulse were investigated with time-resolved and time-integrated diagnostics.
Various results of the numerical simulations could be confirmed. With respect to the time-integrated measurements, an improvement of the contrast resulted in a blue shift of the whole spectrum, compared to a red shift without plasma mirror. By comparing the maximum red shift of the spectrum and the corresponding central wavelength with the results of the analytical description, the scale length of the preplasma was determined to be (0.18 ± 0.11) µm and (0.83 ± 0.39) µm with and without plasma mirror, respectively.
It was shown that this measurement method holds a promising possibility to measure the preplasma properties before the arrival of the maximum intensity, in an non-invasive way. In the framework of this thesis, a measurement of the preplasma state picoseconds prior to the arrival of the maximum intensity could be demonstrated. In the future, this can be further improved by increasing the dynamic range of the used diagnostics.
At last, two experimental campaigns to improve the proton energy and particle number during the laser-ion acceleration were carried out at PHELIX. In the first step, the absorption of the laser energy in the target at an angle of incidence of 45° was increased by various methods. Changing the laser polarization from s- to p-polarization, while using target thicknesses in the range of 1 µm, yielded the best results. The second step was to increase the laser intensity, which lead to the generation of protons with a maximum energy of up to 93 MeV for a laser intensity in the range of 8×10^{20} W/cm^2, resulting in a new record for the laser system PHELIX.

Contents

1 Introduction and motivation

Since the first experiments on laser-ion acceleration in the 1970s [1, 2, 3], a lot of work has been done, resulting in the acceleration of protons with energies in the tens of MeV range in 2000 [4, 5]. Since this breakthrough, many acceleration mechanisms have been proposed by theoretical investigations which were backed up by numerical simulations. Current laser systems are able to reach a sub-picosecond pulse duration and the intensities that are necessary to realize these type of schemes.
However, there is an obvious discrepancy between the kinetic energy of the ions predicted by the simulations [6, 7] and the experimental observations [8, 9]. The corresponding field of ion acceleration, focusing on the interaction of short, intense laser pulses with sub-micrometer-thick targets, has been explored extensively with the help of particle-in-cell (PIC) simulations, ranging from one-dimensional studies up to computationally expensive 3-D simulations. These simulations predict optimal conditions for the laser and target that have to be matched during the experimental implementation, with reachable ion energies that strongly depend on the considered dimensionality of the simulation.
One of the uncertainties, which might explain the discrepancy between experiment and simulation, is the condition of the target during the last instants, before the peak intensity arrives at the target [10]. The generation of such disturbances of the target, which is called preplasma, extends over a large temporal range up to nanoseconds and densities extending over several orders of magnitude [11]. Therefore, this interaction region exceeds the typical time window that is explored within PIC simulations, which is usually in the picosecond time range due to their long computation time. This leads to the necessity of treating the preplasma as an input parameter for the numerical simulations.
However, the measurement of the preplasma properties like its scale length, temperature and density distribution at such time scales is challenging. Current techniques are able to resolve some of these properties either for long scale plasmas in the range of tens of micrometers [12, 13], or require a probe beam with a very short pulse duration in the femtosecond regime [14, 15]. A novel method that extends the possible measurement ranges, which will be presented within this work, relies on the spectral analysis of the light which is reflected off the target during the laser-plasma interaction (LPI).
The idea of analyzing the light reflected by the plasma to get insight into the interaction itself has been around in the community for several years, like the measurement of Brillouin scattering [16]. This type of measurement was later adapted to measure the holeboring (HB) velocity by Zepf *et al.* [17] or the corresponding acceleration [18]. Further attempts have been made to measure the acceleration, introduced by a laser pulse with an intensity in the range of 10^{18} W/cm^2, in a time-resolved manner [19]. With the help of PIC simulations, Kingham *et al.* [20] made a first direct correlation between the phase shift of

the laser and the movement of the critical density position. Palaniyappan *et al.* [21] revisited this measurement principle to observe the relativistic transparency during the interaction of an ultra-intense laser pulse with targets in the nanometer range. An experiment that intended to measure this relativistic transparency was conducted by Wagner *et al.*, at the Petawatt High-Energy Laser for Heavy-Ion eXperiments (PHELIX) [22] at the GSI Helmholtzzentrum für Schwerionenforschung GmbH. They measured the reflected spectrum with a time-integrating spectrometer, showing strong variations for different laser parameter (Fig. 1.1).

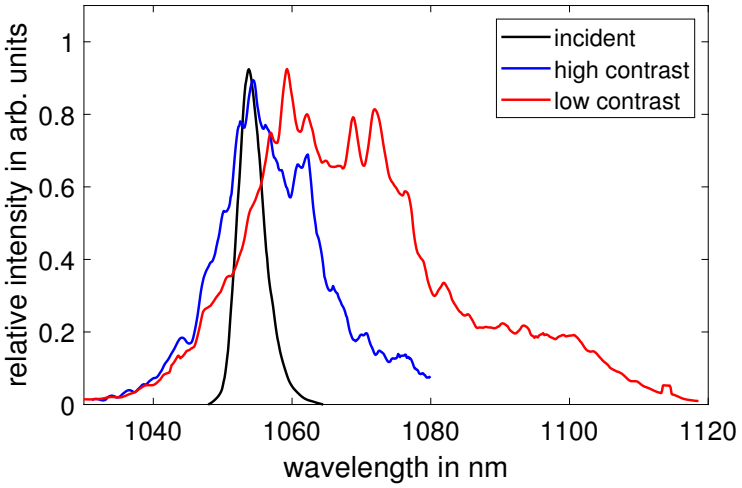

Figure 1.1: Spectrum of the reflected laser pulse, measured during an experimental campaign at the PHELIX laser, for a laser intensity of 10^{19} W/cm^2. These spectra were obtained for a high temporal contrast (blue) and low temporal contrast (red) of the laser pulse. The black line shows the spectrum of the incoming laser pulse. When the temporal contrast is reduced, the maximum red shift increases in addition to a complete shift of the spectrum to higher wavelengths [23].

The behavior of the spectrum, which seemed to depend on the used temporal contrast, could not be explained sufficiently. This lead to the main idea of this thesis: To correlate the spectral behavior of the reflected laser pulse to the conditions of the preplasma.
Therefore, the main goal of this thesis was to verify the validity of this method. For this reason, 2-D PIC simulations were performed and the resulting properties of the reflected pulse had been monitored for different preplasma scale lengths and temperatures. The findings were used to directly correlate the time-resolved spectral properties to these preplasma properties.
To explain this behavior, an analytical description for the HB velocity and acceleration was developed and compared to the simulation results. In addition to the numerical studies, two experimental campaigns have been performed to validate the correlation between

preplasma condition and the spectral properties of the laser pulse after the interaction.
Besides the experiments focusing on the preplasma conditions, two additional experimental campaigns were conducted, which focused on the enhancement of the laser-ion acceleration at PHELIX.
The presented thesis is structured as follows. Section 2 describes the interaction of intense relativistic laser pulses with matter, with an emphasis on the evolution of the laser pulse within a plasma. A description of the general properties of such a plasma are given first, followed by its generation during the interaction of a laser pulse with a target. The interaction effects are presented and the resulting consequence on the laser-ion acceleration is described. The simulation based on the method of particle-in-cell (PIC) is described and the section is completed by a discussion about the corresponding differences to the experimental observations, which might be correlated to the unknown preplasma conditions.
An overview of the currently available methods for the analysis of these preplasma conditions is given in Sec. 3, and the new method based on reflection spectroscopy is introduced. The validity of this method is studied on the basis of PIC simulations with respect to the influence of the preplasma temperature (Sec. 3.3.7) and plasma scale length (Sec. 3.3.8). The analytical description of the HB velocity and acceleration is described and compared to the simulation results.
The above-mentioned correlation between the preplasma properties and the reflected pulse is studied during two experimental campaigns which are presented in Sec. 4, including the setup and necessary steps to influence the temporal contrast. The results of both campaigns are analyzed and later compared with the numerical simulations, which is followed by a discussion.
Finally, in addition to the study of the preplasma condition, further experimental campaigns focusing on the enhancement of the laser-ion-acceleration at PHELIX are presented in Sec. 5.
The results and findings of this thesis are summarized and concluded in Sec. 6, and corresponding future prospects are presented.

2 Interaction of intense laser pulses with matter

The following sections describe the fundamentals that are necessary to understand the interaction of a intense laser pulses with matter, which form the basis for the problems to be investigated within this thesis.
When a material is irradiated with a sufficiently-high laser intensity, a transition into a plasma occurs. This transition, along with all its necessary quantities, is introduced in Sec. 2.1. Section 2.2 describes the process of laser-produced plasmas in more detail, including its generation and the interaction processes between laser and plasma. One of these effects occurring during such an interaction is the laser ion acceleration, which Sec. 2.3 first describes, followed by the introduction of the numerical tools that are often used to study such processes (Sec. 2.4). These simulations do not always reflect the observations within the laboratory, which might be correlated to the properties of the plasma that is present in experimental conditions and is mostly unknown. This difference, which is addressed in Sec. 2.5, is the central issue which is to be examined with the method that is developed in this work.

2.1 General properties of a plasma

The concept of a plasma refers to a state of matter with a high internal energy, at which the atoms are partly or fully ionized. In addition, the plasma shows a collective behavior, which means that the positive and negative charges generate electric and magnetic fields that affect other charged particles far away [24], in contrast to the solid state where atoms mainly affect the direct neighboring atoms. The collective behavior and the similar amount of negative and positive charged particles lead to an effect called quasi-neutrality, where the plasma is globally neutral, but not locally. This state emerges as the Coulomb-potential of a single charge Q is screened by surrounding charges [25]:

$$\varphi(r) = \frac{Q}{4\pi\varepsilon_0}\frac{1}{r}e^{-r/\lambda_D}. \tag{1}$$

Equation 1 describes the Debye-potential with the radial distance r between the charges, where ε_0 corresponds to the dielectric field constant and λ_D is the so called Debye length, which describes the screening length of the potential. In a quasi-neutral plasma λ_D can be expressed as a function of the surrounding electron density n_e, as well as the corresponding electron temperature T_e and is given by

$$\lambda_D = \left(\frac{\varepsilon_0 k_B T_e}{e^2 n_e}\right)^{1/2}, \tag{2}$$

with the electron charge e and the Boltzmann constant k_B [24]. If the distance between the charged particles is in the range of the Debye length, the potential is rapidly weakened and regions farther away from a test charge ($r >> \lambda_D$) are effectively field free. These properties are especially important for so-called particle-in-cell (PIC) simulations which will be later described in Sec. 2.4. This assumption is only valid if enough particles are within the Debye sphere to effectively screen the potential. The corresponding number of particles N_D that are contained in a sphere of the radius λ_D, the so-called Debye sphere, should be much larger than 1 [24]:

$$N_D = \frac{4}{3}\pi n_e \lambda_D^3. \tag{3}$$

Otherwise an effective screening of the potential can not be assumed. This assumption might not be valid for a high-density low-temperature plasma, because the Debye length increases with temperature and decreases for higher densities.

Since the main topic of this thesis focuses on the analysis of electromagnetic (EM) waves, an important property is the electron plasma frequency ω_p, which has a strong influence on the behavior of such EM-waves within a plasma. It describes the oscillation frequency of the electrons, when experiencing a small displacement from their rest position. The plasma frequency is then defined as [25]:

$$\omega_p = \sqrt{\frac{e^2 n_e}{\varepsilon_0 m_e}}. \tag{4}$$

It depends on the electron density n_e and electron mass m_e, as well as the electron charge e and the dielectric field constant ε_0.

This plasma property can be used to describe the dispersion relation of an EM wave in a plasma, which is obtained when solving the Maxwell-equations. The resulting relation is given by [26]

$$\omega_L^2 = \omega_p^2 + k^2 c^2 \tag{5}$$

with the speed of light c and the wavenumber k of the laser. Those EM waves that fulfill $\omega_L > \omega_p$ can propagate in a plasma. Likewise, for a given laser frequency ω_L the electron density needs to be low enough for the plasma to remain transparent. At the threshold of $\omega_L = \omega_p$, a maximum electron density n_c can be defined which can not be passed by the incident laser:

$$n_c = \frac{\varepsilon_0 m_e \omega_L^2}{e^2} \approx 1.1 \times 10^{21} \left(\frac{\mu m}{\lambda_L}\right)^2 cm^{-3}. \tag{6}$$

This density is called the critical density and is mainly determined by the wavelength λ_L of the incoming EM wave. A plasma can therefore be split in two different regions where the

electron density is lower ($n_e < n_c$), or higher ($n_e > n_c$) than the critical density, described as either underdense or overdense, respectively. An example for these regions, on the basis of an expanded plasma density profile, is shown in Fig. 2.1.
This definition in combination with Eq. 4 and Eq. 5 can be used to describe a density-dependent index of refraction for the EM wave [27]

$$\eta = \sqrt{1 - \frac{\omega_p^2}{\omega_L^2}} = \sqrt{1 - \frac{n_e}{n_c}}. \tag{7}$$

Equation 7 becomes imaginary if $\omega_p > \omega_L$ or $n_e > n_c$ and implies that an exponentially decaying field penetrates into the overdense region. The penetration distance is given by the skin depth [24]

$$L_s = \frac{c}{\sqrt{\omega_p^2 - \omega_L^2}}, \tag{8}$$

with the speed of light c, the laser angular frequency ω_L and the plasma frequency ω_p. A schematic of this exponential decay is shown in Fig. 2.1, given by the red curve in the overdense region of the plasma.

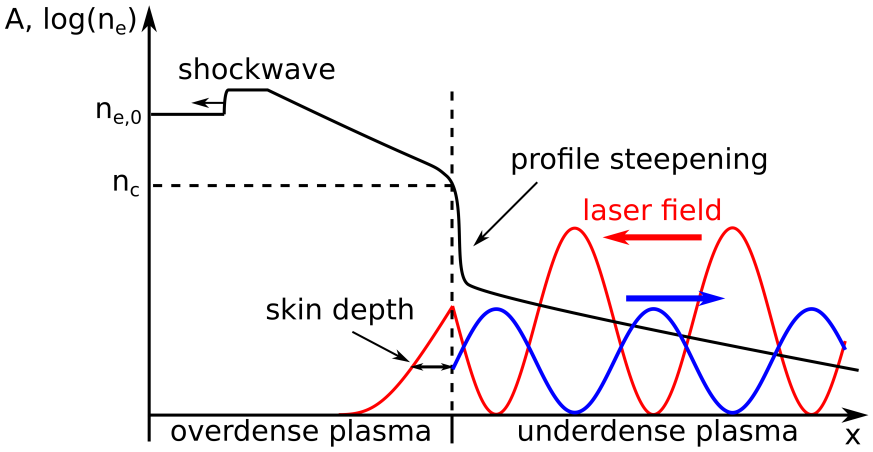

Figure 2.1: Schematic of the spatial density distribution (black solid line) and corresponding plasma regions, separated by the critical plasma density n_c into an underdense and overdense region. The expanding plasma creates a shock wave that propagates into the overdense region of the plasma. The laser (red) can propagate within the underdense region up to the position of the critical density, given by the dashed lines. At this position, an exponentially decaying field reaches into the overdense region of the plasma. During this interaction, a fraction of the laser pulse is reflected (blue) at the critical density. The interaction of the laser pulse with the critical density leads to a steepening of the density profile, which is described in Sec. 2.2.4.

It describes the depth from the critical surface at which the amplitude of the field drops to the fraction of 1/e, which increases if the difference between laser- and plasma frequency decreases. When reaching the threshold of equal frequencies, the skin depth approaches infinity and the plasma becomes transparent.
The mentioned properties correspond to an ideal plasma which can be described by the pressure and number density of the ions and electrons, as well as one common temperature. The corresponding particle velocities can be described by a Maxwellian distribution and the ionization degree is given by the Saha equation [25]. If there are no radiation losses, which means that every radiation process is balanced by an absorption process, the plasma is in a thermodynamic equilibrium [28]. Even if this equilibrium is not given for the entire plasma and radiation losses are not negligible, like in nanosecond laser induced plasmas, there can still be regions where the assumptions hold true. This is called a plasma in local thermal equilibrium. In the case when the electrons and ions cannot be described by a single temperature, this description is valid if the variations in space and time are small and the collision processes are more important than dissipative radiative processes [25, 28].
Both assumptions are not valid anymore if the timescales of interaction are in the picosecond range, like during the interaction of a high-power laser with a plasma. Therefore such an interaction is examined in the following section.

2.2 Laser-produced plasmas and interactions

Since the focus of this work is on the investigation of the laser-plasma interaction (LPI), the generation of a plasma with a relativistic laser pulse will be introduced for completeness reasons. During the interaction of the laser pulse with such a plasma, various effects occur which influence both the plasma and the pulse itself. These effects will be described, with an emphasis on the ones that are necessary for the method based on reflection spectroscopy.

2.2.1 Ionization

The common process of ionizing matter with low intensity EM waves is the absorption of photons with an energy that exceeds the ionization energy of the material. This energy is typically in the range of a few electron Volt (eV) to tens or hundreds of eV, depending on the material [29]. The energy of a photon, which is given by $E_p = \frac{\hbar c}{\lambda}$, only amounts to 1.18 eV for an exemplary wavelength of 1053 nm, which is much smaller than one of the lowest ionization energies of 3.89 eV [29].
Nevertheless, the process of ionization can still occur if the intensity of the laser pulse, and

therefore the field strength, is high enough to trigger one of different intensity-dependent ionization processes. The simplified general principle of the three most important processes is schematically presented in Fig. 2.2, showing the behavior of an electron within the radial dependent coulomb potential of an atom, indicated by the black solid line. The ionization energy E_{ion} is indicated by the dashed black line and the laser field potential, which is assumed to be linear within the extent of an atom, is shown in green [30].

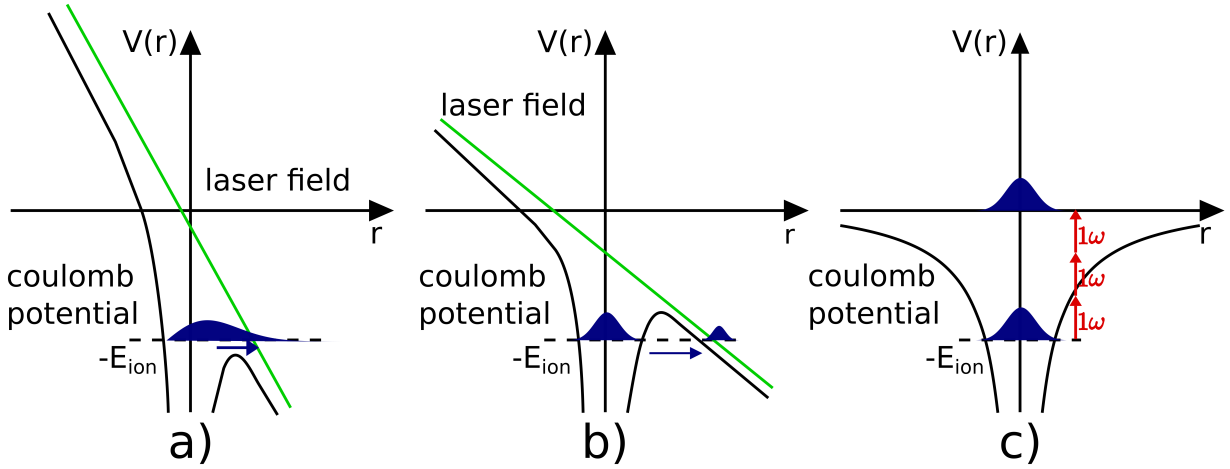

Figure 2.2: Schematic description of the mechanisms that are responsible for ionizing matter with a high-intensity laser pulse. The radial dependent coulomb potential of an atom is given by the black solid line, and the corresponding ionization energy of the electron is indicated by the dashed line. The green lines correspond to the field of the incident laser pulse and the electron distribution within the coulomb potential is indicated in blue. The main ionization mechanism for high laser intensities is the barrier-suppression ionization (a) which is replaced by the tunnel ionization (b) and multi-photon ionization (MPI) when the laser intensity is reduced.

The main process occurring at high laser intensities, and therefore in the presence of high field strengths, is the mechanism of barrier-suppression (Fig. 2.2a). The laser field distorts the coulomb potential of the atom until the energy-barrier is reduced below the needed ionization energy of the electron. The necessary laser intensity I_L can be estimated for a given ionization energy E_{ion} [27]

$$I_L \simeq 4 \times 10^9 \left(\frac{E_{ion}}{eV}\right)^4 Z^{-2}\,\mathrm{W/cm^2}, \tag{9}$$

which results in $\approx 1.4 \times 10^{14}\,\mathrm{W/cm^2}$ in case of a hydrogen ion.
At lower laser intensities, the coulomb potential is not fully suppressed but deformed by the laser field. This leads to a local reduction of the potential in certain regions (Fig. 2.2b). The electron now has the possibility to overcome the barrier because of the tunneling

effect, whereby the probability increases with the strength of the applied electric field [27]. At even lower laser intensities in the range of 10^{10} to 10^{12} W/cm^2, the dominating process becomes MPI [27, 30], shown in Fig. 2.2c. Under such conditions, the photon flux is high enough to absorb multiple photons at the same time. The resulting combined energy of the photons can be high enough to excite the electron past the coulomb potential.
Another ionization process that occurs over a large range of laser intensities below 10^{14} W/cm^2 [30] is the collisional ionization, which is responsible for a pre-ionization of the target material, even for low laser intensities. In the presence of a plane EM wave an unbound electron can follow the oscillation of the laser field. During this adiabatic movement the laser field does not transfer energy to the electron, but in the presence of further atoms the electron can collide with the bound electrons, which leads to the ionization of further atoms [30]. A more detailed description of the ionization mechanisms is found in [27, 30].

2.2.2 Relativistic effects

The movement of the released electrons during the ionization processes follow the oscillation of the incident laser field. The corresponding velocity can be correlated to the present amplitude of the laser field E_0. The classical velocity of the electron can be described by [25]:

$$v_{e,class} = \frac{eE_0}{m_e \omega_L}, \tag{10}$$

with the electron mass m_e and charge e, in addition to the laser angular frequency ω_L [25]. If the field amplitude is sufficiently high, this classical velocity would exceed the speed of light. Therefore, the so-called dimensionless field amplitude a_0 is introduced, which describes the ratio of the electron velocity (Eq. 10) and the speed of light [27]:

$$a_0 = \frac{eE_0}{m_e \omega_L c} = \sqrt{\frac{2e^2 I_0 \lambda_L^2}{c^5 m_e^2 n \varepsilon_0 (2\pi)^2}} \approx \sqrt{\frac{I_0[\mathrm{W/cm^2}]\, \lambda_L^2[\mu\mathrm{m}^2]}{1.37 \times 10^{18}}}. \tag{11}$$

Since the field amplitude and laser intensity are correlated with $I = \frac{1}{2} c n \varepsilon_0 |E|^2$ [30], it can be rewritten for a given laser intensity I_0 and laser wavelength λ_L. For intensities approaching 10^{18} W/cm^2 and a wavelength of 1 µm, the field amplitude is in the order of 1 and relativistic effects have to be taken into account. In particular, the mass of the electrons has to be adjusted for increasing laser intensities, which is included in the Lorentz factor $\gamma = 1/\sqrt{1 - v_{el}^2/c^2}$. This can also be expressed by the dimensionless field amplitude, by averaging over one laser cycle which, for the case of a linear polarized field, results in [27]:

$$\bar{\gamma} = \sqrt{1 + \frac{a_0^2}{2}}. \tag{12}$$

One consequence is the correction of the critical density n_c by the Lorentz factor, with the help of Eq. 11 and Eq. 12:

$$n_{c,rel} = \bar{\gamma}\, n_c = 1.1 \times 10^{21} \sqrt{1 + \frac{I_0[\mathrm{W/cm^2}]\, \lambda_L^2[\mu\mathrm{m}^2]}{2.74 \cdot 10^{18}}} \left(\frac{\lambda_L}{\mu\mathrm{m}}\right)^{-2} \mathrm{cm}^{-3}. \tag{13}$$

This shows that the laser can reach higher plasma densities with increasing intensity or reducing wavelength. If the density of the whole plasma drops below the relativistic critical density, but is still above the classical critical density, the plasma becomes transparent for the EM wave, which is called relativistic transparency [31].

2.2.3 Laser absorption

The electrons that are oscillating in the laser field can now trigger several effects that lead to an energy transfer from the laser to thermal plasma energy. The higher the velocity of the electrons, the greater the distance that can be covered during an oscillation period, reaching the micrometer range for sufficient intensities in the range of 10^{20} W/cm^2 when using Eq. 10. This distance changes the interaction with the surrounding plasma, leading to different absorption mechanisms depending on the laser intensity, which will be described in the following section.

One of the mechanisms for laser absorption is inverse bremsstrahlung which describes the absorption of a photon by an electron during the collision with an ion or electron, also known as collisional absorption. The frequency of such a collision with an ion ν_{ei} can be described by a kinetic theory, which depends on the ion density of the material n_i and the corresponding electron temperature T_e [32]:

$$\nu_{ei} \propto \frac{n_i}{T_e^{3/2}}. \tag{14}$$

An increased frequency of collisions increases the absorption, which reaches its maximum at the critical density, since the laser can not further penetrate the plasma into higher density regions. If the laser intensity increases, the electron temperature rises accordingly, which leads to a reduction of the absorption. Therefore, the intensity regime at which collisional absorption becomes relevant is limited to intensities below 10^{15} W/cm^2 [25].

When increasing the laser intensity beyond this threshold, other mechanisms start to dominate the absorption. One of these is resonance absorption, occurring for an incidence angle between laser and the plasma surface which is different from zero, under the condition of a field component with p-polarization [33]. With these conditions fulfilled, the

electric field can resonantly drive an electron plasma wave at the critical density, which can transfer energy to the plasma by collisional or collisionless damping effects [32]. For a laser irradiance beyond 10^{16} W/cm^2 the main fraction of energy transfer to the electrons is achieved either by Brunel- or j x B-heating [25].

Brunel heating, or initially named "not-so-resonant resonant absorption" [34], occurs for the same conditions as resonance absorption, but becomes more efficient for large density gradients. The electrons at the critical surface density are dragged into the vacuum or underdense plasma region during the first oscillation period of the laser field and sent back into the overdense region during the next period, in the presence of a steep density gradient. Since the laser field cannot penetrate the plasma beyond the critical density, the electron is accelerated into the plasma. Therefore, this effect is also referred to as vacuum-heating [34, 35].

A further mechanism is $\vec{j} \times \vec{B}$-heating which contributes to the total absorption for relativistic intensities, at which the influence of the magnetic field can not be neglected. Since the movement of the electrons is parallel to the electric field, the direction of the $\vec{v} \times \vec{B}$ component of the Lorentz force can be described by $\vec{E} \times \vec{B}$, which is parallel to the k-vector of the wave. Therefore, a force in the propagation direction of the EM wave is introduced which accelerates electrons into the target even at a normal incidence angle [26, 36].

When the spatial intensity variation of the laser pulse is considered, which is typically approximated by a Gaussian distribution, another possibility to transfer energy to the electrons arises. While following the oscillation of the EM field, the electrons move into regions of lower intensity during the first half of the laser cycle. When the direction of the field changes during the second half of the oscillation, the electron experiences a reduced field strength because of the lower intensity. This leads to an effective force towards reduced laser intensities. The so-called ponderomotive force f_p can be described by [27]:

$$f_p = -\frac{e^2}{4 m_e \omega_L^2} \nabla |E(r)|^2, \tag{15}$$

with the charge e and mass m_e of the electron, the laser angular frequency ω_L and the radially changing field amplitude E(r). This leads to the acceleration of electrons in the direction of the spatial field-gradients.

The described absorption mechanisms result in a heating effect of the electrons up to energies in the range of keV to MeV [27]. The generation of such highly-energetic electrons on short, sub-picosecond time scales leads to the occurrence of various effects during the LPI, which will be described briefly in the following sections.

2.2.4 Radiation pressure and holeboring

An important effect occurring during the LPI is the so-called holeboring (HB), introduced by the pressure of the laser pulse P_L onto a reflecting surface, which is given by [37]

$$P_L = \frac{I_L}{c}(1 + R). \tag{16}$$

It depends on the laser intensity I_L, the speed of light c and the reflectivity of the surface R. The ponderomotive force of the laser pulse pushes the electrons into laser direction, leading to a pile-up of the electrons within the skin depth if the pondoromotive pressure is comparable to the plasma pressure [30]. The charge separation creates a quasi-static field that is sufficiently strong to impact the much heavier ions. The ions follow the movement of the electrons, which results in the formation of a density discontinuity that is traveling into the target [27]. A schematic of this effect, also denoted as profile steepening, is shown in Fig. 2.1. The velocity v of this movement can be derived by balancing the pressure of the laser with the momentum flux of the plasma mass flow [37]:

$$2n_i M v^2 = (1 + R)\frac{I_L}{c}, \tag{17}$$

with the mass M and density n_i of the ions. Solving this equation with respect to the possible momentum transfer, including absorption η_a and angle of incidence of the laser θ, the HB velocity v_{hb} can be expressed by [17, 27]

$$v_{hb} = c\left(\frac{n_c}{n_e}\frac{Zm_e}{M}\frac{(2 - \eta_a)\cos(\theta)}{4}\frac{I_L\lambda^2}{1.37 \times 10^{18}}\right)^{1/2}. \tag{18}$$

The velocity depends on the speed of light c, electron density n_e and critical density n_c, in combination with the ionization degree Z and the mass M of the ions. Additionally, the velocity increases with increasing laser intensity I_L, given in W/cm^2, and wavelength λ in µm. The momentum transfer reaches its maximum if the laser is completely reflected ($\eta_a = 0$) at normal incidence, which decreases the velocity if the laser absorption or the incidence angle are increased. However, Eq. 18 only holds true for non-relativistic HB velocities. The relativistic description has been derived by Robinson *et al.* [38], which takes into account that the laser intensity in the moving frame is not equal to the intensity in laboratory frame. Using the relativistic gamma factor γ, this changes the initial equation of the pressure balance to [38]

$$2\gamma^2 n_i M v^2 = \frac{I_L}{c}\left(\frac{1 + v/c}{1 - v/c}\right). \tag{19}$$

Solving this equation leads to a description of the relativistically corrected HB velocity:

$$v_{hb} = c\frac{\sqrt{\Sigma}}{1+\sqrt{\Sigma}}, \tag{20}$$

where $\Sigma = I_L/(Mn_ic^3) = I_L/(\rho c^3)$ is the so-called dimensionless piston parameter, which depends on the density of the material ρ. Since the laser can only propagate up to the critical density of the plasma, these equations represent the corresponding velocity of n_c. Equation 18 and Eq. 20 do not take any density profile or pressure of the plasma into account, which is assumed to change the behavior of the HB velocity [39].
As long as the light pressure exceeds the pressure of the plasma, the area of the critical density is pushed into the target. Since the plasma density shows a spatial gradient, the laser pulse may, at some point, enter a region where the plasma pressure overcomes the light pressure and the HB process stops. This is called the HB limit with the corresponding density limit n_s, which can be analytically described under the assumption of an exponential density distribution [40]:

$$n_s = 4\varepsilon^2 a_0^2 n_c \left(1 + R - \frac{(1-R)}{\beta_h \alpha}\right). \tag{21}$$

The density limit depends on the velocity of the hot electrons $\beta_h = v_{e,h}/c$, and the geometrical factor $\alpha = ir/2$, where r indicates the momentum distribution of the electrons ($r = 1$ for non-relativistic Maxwell distribution and $r = 2$ for the relativistic case) and $i = 1, 2$ or 3 describes the dimensionality of the interaction. Looking at Eq. 21, the density limit increases for higher laser intensities, meaning that the laser pulse can penetrate deeper into the plasma.
For an imperfect reflectivity $R < 1$ the density limit decreases with rising electron velocities and interaction dimensionality, which results in a lower density limit in the three-dimensional case compared to a one-dimensional interaction. The dimensionality might also change the HB interaction, resulting from an additional degrees of freedom for the lateral energy diffusion [40], which would slow down the dynamic and therefore lead to a reduced HB velocity if the interaction is not purely one-dimensional.

2.2.5 Doppler shift at a moving reflection point

The effect of HB, in combination with the reflective nature of the critical density, leads to generation of a moving reflective mirror for the interacting laser pulse.
At such a moving interface, the laser pulse is influenced by the Doppler effect which alters the initial wavelength λ_0 of the incoming pulse depending on the movement direction and velocity of the mirror. The resulting wavelength for a velocity of $\beta = v/c$, where c corresponds to the speed of light, is given by [41]

$$\lambda_s = \lambda_0 \left(\frac{1 - 2\beta\cos(\alpha) + \beta^2}{1 - \beta^2} \right)^{-1}. \tag{22}$$

The wavelength λ_s additionally depends on the laser incidence angle α, which reduces the effective velocity for increasing incidence angles on the reflective surface [41].
This effect is of utmost importance for this thesis because the spectral shift that is introduced by the Doppler effect is correlated to the movement of the critical density position.

2.3 Laser-ion acceleration

One of the most utilized effect that results from the interaction of a relativistic laser pulse with a plasma is laser-ion acceleration. The acceleration of mainly protons and mid-Z ions has become a major topic within the field of LPI. Since the first experiments in the 1970s [1, 2, 3], laser-ion acceleration is more and more drifting from being a research topic to an application oriented field [42, 43, 44, 45].
Unlike the acceleration of electrons by the ponderomotive force of the laser fields, a direct acceleration of protons and heavier particles by a laser pulse is currently not possible. This becomes obvious considering Eq. 10, which can also be adapted for protons by replacing the electron mass with the proton mass:

$$v_p = \frac{eE_0}{m_p \omega_L}. \tag{23}$$

This leads to a decrease of the dimensionless field amplitude for protons by the electron-proton mass ratio:

$$a_{0p} = \frac{m_e}{m_p} a_{0e} = \frac{a_{0e}}{1836}. \tag{24}$$

The corresponding distance that is covered by the proton during one laser cycle is in the sub-nanometer range, compared to the much higher micrometer range of the electrons. Triggering similar interaction effects as for the relativistic electrons requires to increase this interaction range. To reach these relativistic regions with protons, the laser intensity needs to be six orders of magnitude higher resulting in an intensity in the range of 10^{24} W/cm^2, which exceeds the currently reachable intensities of the available laser systems with intensities in the range of 10^{22} to 10^{23} W/cm^2 [46].
Therefore, the creation of static fields during the interaction needs to be exploited to accelerate heavier particles. This can be achieved by different mechanisms which will be described in the following sections.

2.3.1 Target normal sheath acceleration

One of the most studied mechanisms of laser-ion acceleration is the so called "Target-Normal Sheath Acceleration" (TNSA), which has been first described in 2000 [4, 5]. The main acceleration-process can be divided into four steps which are visualized with the help of a simplified scheme, shown in Fig. 2.3.

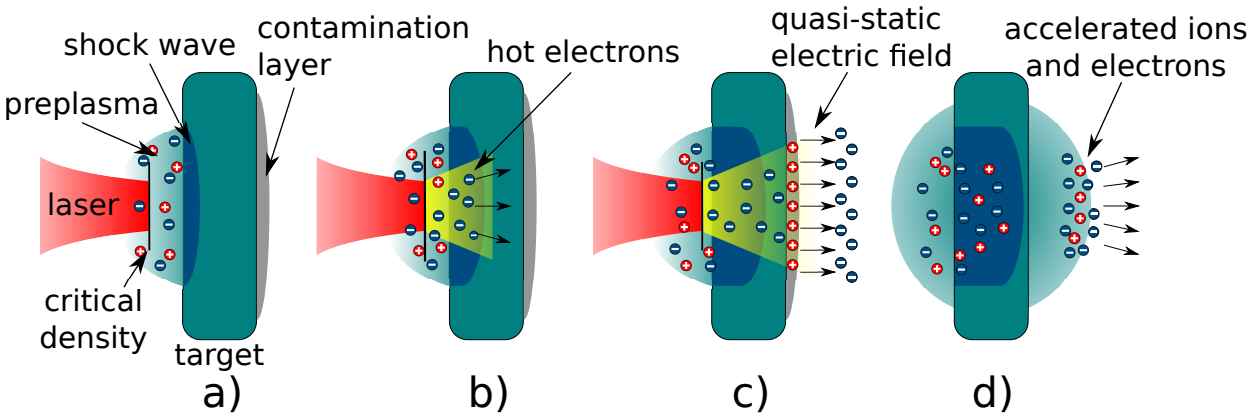

Figure 2.3: Scheme of the TNSA-mechanism which is divided in four steps. A preplasma is formed, creating a shock wave propagating through the target. The laser penetrates this preplasma up to the critical density (a). Electrons are heated by the laser-matter interaction and accelerated into the target (b). These hot electrons leave the target at the back side, forming an electric field that ionizes the contamination layer at the rear side (c). These accelerated ions and electrons co-move into the vacuum (d).

A laser pulse, with an intensity exceeding 10^{18} W/cm^2, is focused onto a thin target with an extent of 1 - 100 µm [47, 48]. The laser pulse penetrates the plasma up to the position of the critical density (Fig. 2.3a). During this phase, the laser pulse accelerates electrons into the target because of the ponderomotive force and different absorption mechanisms, which were described in Sec. 2.2.3 [49]. These fast electrons propagate through the target and exit the rear side with an increased divergence angle, due to scattering processes and recirculating electrons (Fig. 2.3b).
A quasi-static electric field forms at the rear side, normal to the target surface, due to the charge separation between the ions and the electron sheath. The amplitude A of this field depends on the electron energy and extend of the sheath $A \propto E_e/d$, and reaches TV/m [47] for electron energies $E_e = k_B T_e$ in the keV to MeV range and an extent of the electron sheath in the range of the Debye length [6].
These fields are strong enough to ionize the rear surface of the target and directly accelerate the corresponding ions (Fig. 2.3c). The accelerated ions originate mostly from a thin contamination layer from the back side, containing water and hydrocarbons, with a thickness in the nanometer range (Fig. 2.3a) [48]. After the laser irradiation, the directed

beam which is formed by electrons and ions is moving into the vacuum (Fig. 2.3d).
A model which describes the velocity evolution of the accelerated ions was introduced by P. Mora [50]. This model correlates the velocity of the resulting ions v_i to the ion sound speed $c_{s,i} = \sqrt{Zk_BT_e/m_i}$, where Z and m_i corresponds to the charge state and mass of the ion, with the electron temperature T_e and the Boltzmann constant k_B. The maximum reachable ion energy depends on the temperature of the electrons and acceleration time [50]:

$$E_{max} = 2m_ic_{s,i}^2\ln(\tau + \sqrt{\tau^2+1})^2 = 2Zk_BT_e\ln(\tau + \sqrt{\tau^2+1})^2 \tag{25}$$

The time t is used to form a dimensionless acceleration time $\tau = \omega_{pi}t/\sqrt{2e}$, whereas ω_{pi} corresponds to the ion plasma frequency and e to the Euler's number. Equation 25 shows that the maximum ion energy increases for a rising electron temperature and acceleration time. With the description of the maximum reachable ion energy, the corresponding particle spectrum can be derived, which describes the amount of particles per unit energy [50]:

$$\frac{dN}{dE} = \frac{n_{i0}c_{s,i}t}{\sqrt{2EE_0}}\exp\left(-\sqrt{\frac{2E}{E_0}}\right), \tag{26}$$

which is increasing with time t and the initial ion area density n_{i0} at the rear side. Such an exponential spectrum is typical for the TNSA mechanism and the slope depends on the constant $E_0 = Zk_BT_e$, with the charge state of the ions Z, the Boltzmann constant k_B and the electron temperature T_e. Since this model does not take any energy transfer from the fast electrons to the ions into account, the accelerating charge-separation field does not decrease, which would result in infinitely high ion energies for long acceleration times [51]. Experimentally, one observes a well-defined energy cut-off at the higher end of the energy spectrum [5, 4]. This observation was the motivation for an improved model for the expected particle energy and spectrum by Schreiber *et al.* [52], taking the interaction time into account which is correlated to the laser pulse duration.
The model is also based on the principle of a confined surface charge at the target rear side that is created by a bunch of laser-accelerated electrons. In contrast to the model of Mora, the formed potential between ions and electrons stays finite. This results in a maximum possible energy of the accelerated ion when its distance to the target surface approaches infinity. Under the assumption of an infinitely long acceleration process by a laser with the power P_L, which experimentally depends on the laser pulse energy and the conversion efficiency from laser energy into hot electron energy η, the maximum ion energy is given by

$$E_{i,\infty} = 2q_im_ec^2(\eta P_L/P_R)^{1/2}. \tag{27}$$

The reachable energy depends on the charge state of the ion q_i, the electron mass m_e, the speed of light c and the relativistic power unit $P_R = m_e c^3/r_e$, where r_e correspond to the classical electron radius. However, due to the exponentially decaying energy spectrum, only very few particles occupy this maximum energy. This ion energy reduces when including the finite electron bunch duration, which is correlated to the laser pulse duration τ_L [52].
The resulting ion energy has been approximated by Zeil *et al.*, simplifying the reduction from the pulse duration, which is given by [53]:

$$E_{max} = E_{i,\infty} \tanh^2\left(\frac{\tau_1}{2\tau_0}\right). \tag{28}$$

Within this approximation, the quantity $\tau_0 = R/v_\infty = R/(2E_{i,\infty}/m_i)^{1/2}$ describes the time of an ion to remain in the vicinity of the accelerating surface charge [53]. The corresponding ion source size $R = r_L + d\tan(\theta)$ depends on the laser focal spot size r_L, the target thickness d and the divergence angle θ of the electrons which are propagating through the target. The presence of a short laser pulse duration with $\tau_1 << \tau_0$ leads to a linear dependency between the maximum proton energy and the laser power ($E_{max} \propto P_L$).
On the contrary, for longer laser pulses which fulfill $\tau_1 >> \tau_0$, the maximum proton energy is proportional to the square root of the laser power ($E_{max} \propto \sqrt{P_L}$) [53]. These cases differentiate if the acceleration time is either given by the pulse duration itself ($\tau_1 << \tau_0$) or the reference time τ_0 when the fast proton leaves the accelerating field before the interaction with the laser pulse ends ($\tau_1 >> \tau_0$).
Since the maximum ion energy is proportional to $1/\tau_0$, which depends on the size of the ion source at the rear side of the target, a reduction of the latter would lead to an increasing ion energy. This is achieved by reducing the target thickness which lowers the resulting electron spot-size at the rear side and the electron-energy loss within the target and therefore increases the strength of the accelerating field.
A counteracting effect, that limits the further reduction of the target thickness, is given by the shock wave which is formed at the beginning of the LPI and propagates through the target [54]. If the target is too thin, the shock wave reaches the rear side before the acceleration time ends. This would either lead to a disturbed surface, which would be imprinted into the spatial distribution of the accelerated particles, or break the target which would stop the acceleration process [54].
Depending on the laser intensity and corresponding temporal contrast, this limits the thickness of the targets to the micrometer range. Another advantage of an increased target thickness is the possibility to create an extended preplasma, which enhances the energy absorption within the plasma, as described in Sec. 2.2.3, and therefore increases the electron temperature [55].

Even though a lot of effort has been invested to find the optimal target thickness for TNSA, different facilities report maximum proton energies for targets with a thickness ranging from hundreds of nanometers to a few micrometers [56, 57, 58, 51]. This shows that, even though no clear specification of optimal parameters can be given, the TNSA mechanism is a robust scheme for the laser-ion acceleration, working for a wide range of laser and target parameters, with a currently maximum reachable proton energy up to 85 MeV [12]. One possibility for these different optimal conditions could arise from the preplasma properties which might differ for the various laser facilities and therefore results in a wide range of optimal parameter, which again emphasizes the need for a diagnostic method that is able to resolve these properties. During the extensive investigation of the TNSA mechanism, more advanced and more promising acceleration schemes [59, 60, 61] have been proposed, which in turn are considerably more sensitive to the precise preplasma conditions.

2.3.2 Acceleration in the relativistic transparency regime

More promising results in terms of higher attainable ion energies are predicted in the regime of relativistic transparency, mentioned in Sec. 2.2.2, which starts to occur for relativistic laser intensities in the range of 10^{20} W/cm^2 to 10^{21} W/cm^2 [59, 60]. Within this regime, the accelerating fields are created within the bulk of the target, in contrast to the TNSA mechanism, where the fields occur at the rear side. Two mechanisms with different optimal target parameters, are the "Relativistically Induced Transparency Acceleration" (RITA) [62] and the "Breakout Afterburner" (BOA) [59]. The latter mechanism is explained with the help of the simplified scheme, shown in Fig. 2.4 [7, 59, 63].
The initial stage is similar to the TNSA mechanism, leading to an acceleration of the ions within the contamination layer (Fig. 2.4a). With increasing intensity and rising relativistic critical density, the laser can penetrate deeper into the target while re-heating the re-fluxing electrons to even higher energies. These hot electrons increase the field strength at the rear side of the target, resulting in an enhanced phase of TNSA (Fig. 2.4b).
At the point when the relativistic critical density exceeds the density of the material, the skin depth tends towards infinity (Eq. 8) and the target becomes relativistically transparent. This induces a volumetric heating of the bulk electrons while generating a strong longitudinal field due to charge separation. This field is co-moving with the ions which leads to a further acceleration of the ions (Fig. 2.4c) until the target breaks and the ions move into the vacuum (Fig. 2.4d). Phase c) is often referred to as "Breakout Afterburner" (BOA) [59]. It is assumed that the charge separation and therefore efficient energy transfer from the electrons to the ions occurs because of the so-called Bunemann instability [64], which transfers the drift energy of the electrons to the ions [65]. The acceleration stage

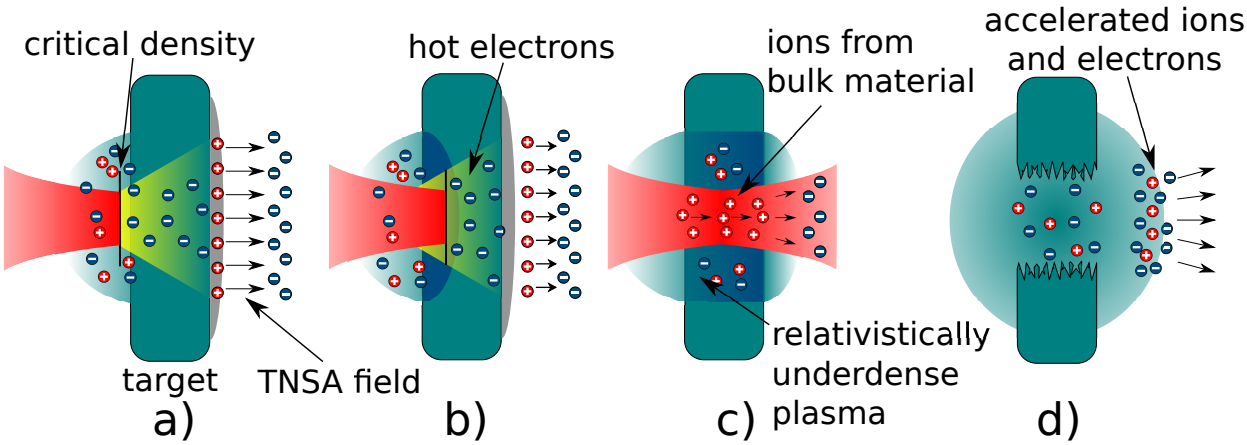

Figure 2.4: Scheme of the acceleration in the relativistic transparency regime. The first step is similar to the TNSA mechanism (a). When the laser intensity rises, the relativistic mass-increase of the electrons leads to a higher critical density, which enables a further propagation of the laser into the target (b). If the critical density exceeds the density of the plasma, the target becomes relativistically transparent and the longitudinal fields created by the charge separation accelerate electrons and ions from the bulk material (c). Afterwards the bunch of electrons and ions propagates into the vacuum (d).

of TNSA leads to the generation of a ion beam in target-normal direction, in combination to a beam that is generated by the BOA in laser direction [66].
Contrarily to the thin targets in the range of the skin depth, the mechanism of RITA relies on a pre-expanded target with a certain extent. The laser pulse propagates through the plasma up to the position of the critical density. As the intensity increases and the relativistic critical density rises, the laser can propagate further into higher density regions. The propagation is accompanied by a pile-up of the electrons behind the critical density, due to the ponderomotive force of the laser pulse.
On these short interaction times the ion movement is very small which are therefore assumed to be immobile. As a result, a strong electrostatic potential is co-moving with the electron pile-up. Positive charged ions, which are initially located deeper inside the target, can be reflected from this potential, resulting in an acceleration up to twice the velocity of the density pile-up [62].
Even though the acceleration in the regime of relativistic transparency has been observed in many experiments [60, 66, 67, 68], with varying optimal target thicknesses ranging from tens to hundreds of nanometers, it is not quite clear which laser and plasma parameter results in the best outcome of the acceleration within the relativistic transparency regime. These acceleration processes have been extensively studied with the help of numerical simulations, which predict a maximum proton energy in the GeV range [7, 59, 60]. However, the maximum reachable ion energies from these mechanisms currently only reach

a similar energy range as given by TNSA [60, 66, 67], even though some research groups claim proton energies of 160 MeV [68]. A possible explanation for this could be the need for a optimal density distribution of the plasma, which enables an interaction at the boundary between a fully opaque interaction and the relativistic transparency, which is difficult to match and control in experimental conditions.

2.3.3 Radiation pressure acceleration

Another advanced acceleration mechanism, which has also been extensively studied with the help of numerical simulations, is "Radiation Pressure Acceleration" (RPA) [61], which occurs during the interaction of a circular polarized laser pulse with very thin targets that stay opaque during the complete LPI. The process of RPA can be divided in different stages, which are shown in Fig. 2.5. The incident laser pulse pushes electrons from the front surface into the target due to the ponderomotive force and light pressure (Fig. 2.5a). A quasi-static electric field forms, which can efficiently transfer energy to the ions (Fig. 2.5b). This quasi-neutral slab, which can be treated as a co-propagating reflecting mirror, is further accelerated by the radiation pressure of the laser (Fig. 2.5c-d) [69].

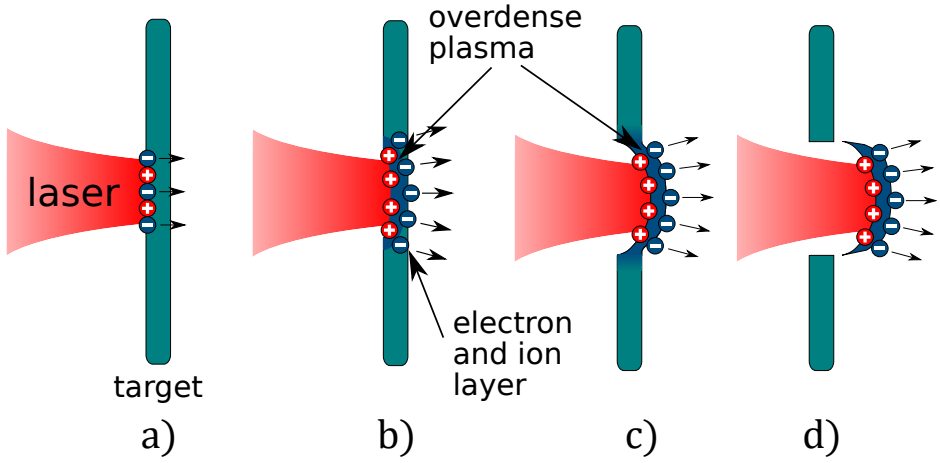

Figure 2.5: Simplified scheme of the radiation pressure acceleration. The electrons are accelerated because of the ponderomotive force of the laser (a). The formation of a quasi-static electric field transfers energy to the ions (b). The quasi-neutral slab of ions and electrons are co-propagating with the laser field and the ions are accelerated (c-d).

The maximum reachable velocity of the accelerated ions strongly depends on the light pressure of the laser (Eq. 16) which increases with the laser intensity and the reflectivity of the plasma. For a reflectivity of R = 1 the maximum ion velocity for a given laser intensity I_L can be described by [69]:

$$v_{max} = \frac{2I_L}{c}\frac{1}{\rho d}\tau_L, \tag{29}$$

with the mass-density of the material ρ and the target thickness d. The maximum velocity increases with the acceleration time τ_L which is correlated to the pulse duration. This leads to a scaling of the maximum reachable ion energy which is proportional to the square of the laser intensity [70], in contrast to the TNSA mechanism with a linear or even square-root scaling, which leads to the expectation of maximum reachable proton energies in the GeV range [71]. However, the scaling with I_L^2 only holds true for the non-relativistic regime with $v_{max} << c$. A relativistic treatment of the maximum reachable ion energy is given by Robinson *et al.* [72]:

$$E = m_i c^2 \left(\frac{2\Sigma}{1 + 2\sqrt{\Sigma}} \right), \tag{30}$$

where Σ is the relativistic piston parameter introduced in Sec. 2.2.4, which is proportional to the laser intensity, the ion mass and density, as well as the speed of light. This leads to reduced scaling for increased intensities, down to a scaling of $I_L^{1/3}$ in the ultra-relativistic regime.

Similar to the acceleration in the transparency regime, RPA occurs for very thin targets in the range of the skin depth [73] and, as seen in Eq. 29, increases with reduced target thickness. To ensure that the electrons are not fully removed from the target and therefore ensure a stable acceleration, the laser field strength in direction of the charge separation must not exceed the strength of the charge-separation field [74]. This leads to a constraint for the usable target thickness d for a given field amplitude a_0:

$$a_0 < \frac{n_e}{n_c} \frac{2\pi d}{\lambda}, \tag{31}$$

with the laser wavelength λ and the ratio of electron density to critical density n_e/n_c [74]. The consequence is that, in contrast to BOA, the target has to stay opaque during the interaction. Since the critical density increases if the electron energy approaches the relativistic regime, which therefore leads to relativistic transparency, the electron temperature has to be kept as low as possible. This is usually achieved by using a circularly polarized laser [61], that reduces the efficiency of many absorption mechanisms [69], and also reduces the formation of sheath fields that are responsible for the TNSA mechanism, which disturb the RPA process [61].

For RPA to be stable and efficient, the target not only has to be thin, but also its plasma scale length must not exceed 0.1 λ to suppress the generation of hot electrons [69]. While these conditions are easy to implement within simulations, the experimental conditions are not as precisely known or controlled, mostly due to the imperfect laser pulse conditions.

This leads to a difficult realization of the necessary experimental conditions, which is why this effect has only been reported once by Kim *et al.* [70], with a maximum proton

energy of 93 MeV, far below the predicted energies, reaching hundreds of MeV. The measurement of such small scale lengths, which are necessary for this type of acceleration mechanism, are challenging. The method to measure the preplasma properties which will be presented in this work might be able to resolve these temperature and scale length regions. This might help to understand the discrepancy between the numerical expectations and the experimentally achieved maximum proton energies.

2.4 Particle-In-Cell simulation

All of the above-mentioned mechanisms of laser-ion acceleration rely on the interaction of a relativistic laser pulse with a solid target or plasma. Such a complex system, consisting of many particles and strong fields, can often not be described by analytical models. This leads to the necessity of utilizing numerical simulations to perform detailed studies of these interactions. One of such methods for simulating the kinetics of a collisionless plasma is the approach of particle-in-cell (PIC), which has been developed in the 1960s [27].
In this approach, one so-called macro particle with a fixed charge q_i and mass m_i represents a large number of particles, which strongly reduces the necessary computational resources. The distribution $f(x_i, v_i, t) = f_i$ of such a particle, in the presence of electric and magnetic fields with the strength E and flux density B, is described by the Vlasov equation [75]:

$$\frac{\partial f_i}{\partial t} + v_i \frac{\partial f_i}{\partial x} + \frac{q_i}{m_s}\left(E + v_i \times B\right)\frac{\partial f_i}{\partial v} = 0. \tag{32}$$

The movement of the charged particles generates electric and magnetic fields. Using the charge density ρ_j and currents J_j, these fields can be calculated by solving the Maxwell equations [75]:

$$\nabla \cdot E = \frac{\rho_j}{\varepsilon_0}, \qquad \nabla \times E = -\frac{\partial B}{\partial t}$$
$$\nabla \cdot B = 0, \qquad \nabla \times B = \mu_0 J_j + \frac{1}{c^2}\frac{\partial E}{\partial t},$$

where μ_0 corresponds to the magnetic permeability, ε_0 to the vacuum permittivity and c to the speed of light. The resulting fields, in combination with external fields, determine the force on the particles and their respective new positions. To implement the calculations, the fields are defined on a discrete grid, in contrast to the position of the particles [35]. This leads to the need for interpolation between both domains. The scheme of a complete cycle for the calculation of the field and particle movement is shown in Fig. 2.6.

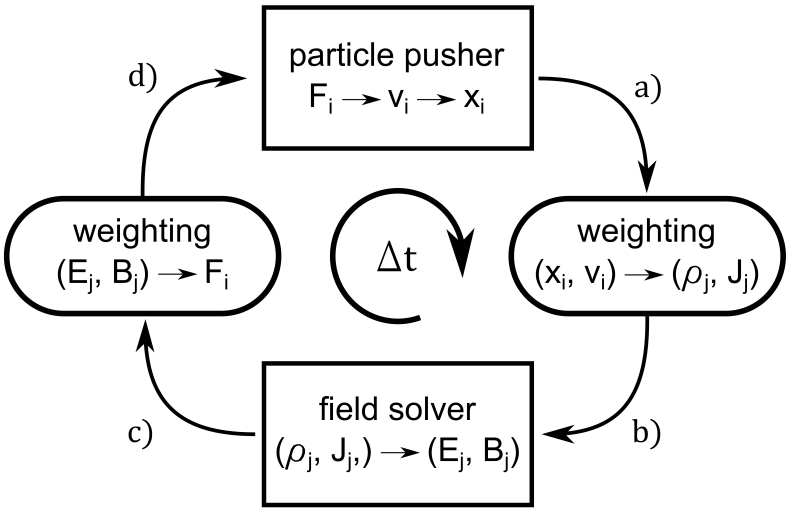

Figure 2.6: Schematic illustration of a calculation cycle of the particle-in-cell algorithm.

The position and velocity of the particles are weighted onto the field-grid to obtain the corresponding charge density and current (a), which is used to calculate the corresponding fields by solving the Maxwell equations (b). Afterwards, the force that acts on the particles is calculated and transferred to the domain of the particles (c), which leads to a variation of the corresponding velocity and position (d) [27]. These calculations become more elaborate for an increasing amount of particles and necessary spatial and temporal resolution and cannot take every interaction effect into account. An example for such an effect is the collision between particles, which is implemented in a very simplified manner in many PIC codes [76], since these usually focus on the simulation of collisionless plasmas.

Another limit to this type of simulation is given by the necessary resolution, which should be lower than the Debye length (Eq. 2) of the plasma to reduce the effect of numerical heating [76], which artificially increases the energy of the simulated system. Since the Debye length increases with $\sqrt{T_e/n_e}$ the simulations are best suited for low electron densities n_e and high temperatures T_e. As an example, the Debye length reaches 1 nm for an electron temperature of 7 keV and an electron density of 3.8×10^{23} 1/cm^3, which corresponds to a hot plasma at solid density. For studying the process of laser-ion acceleration, the simulation has to deal with high densities, low temperatures and long interaction times. This increases the complexity and the computational resources that are necessary to perform such PIC simulations. As an example, the simulation described in Sec. 3.3.1, which requires a resolution in the nanometer range, with $\approx 5 \times 10^8$ grid cells, $\approx 10^9$ macro particles and a simulation time of 2 ps, requires a total computation time of 86.000 CPU hours. To still perform the simulations within a limited time frame, the numerical simulations that are presented during this thesis, are performed with the relativistic particle-in-cell code EPOCH [76] on the Kronos cluster at the GSI Helmholtzzentrum für Schwerionen-

forschung GmbH.

2.5 Discrepancy of initial plasma conditions in simulations and experiments

As mentioned in Sec. 2.3, the outcome of the laser-ion acceleration strongly depends on the initial condition of the target. This condition is not known most of the time in LPI experiments, due to the imperfect temporal profile of the laser pulse. The description of the temporal laser pulse intensity is often idealized by a truncated Gaussian intensity distribution.
While this ideal condition might hold true for times close to the peak intensity, the pulse shape strongly deviates from this model at longer times, in the picosecond to nanosecond range. The ratio of the intensity at an arbitrary time prior to the main pulse $I(t = \tau)$ and the maximum intensity $I(t = 0)$ defines the temporal contrast, whereas different definitions arise for different reference times τ. An example for a temporal pulse profile present in experimental conditions can be seen in Fig. 2.7, showing the evolution of the normalized laser pulse intensity over time.

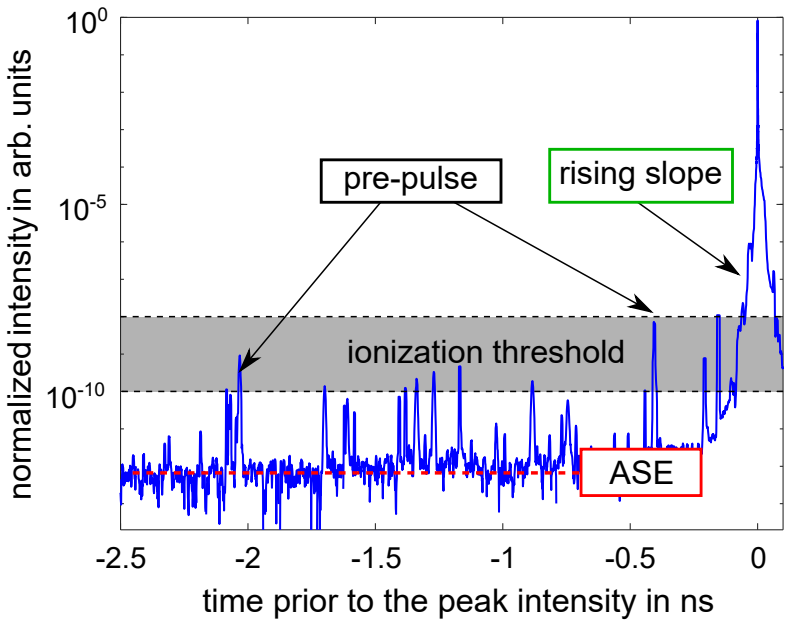

Figure 2.7: Example of the temporal pulse profile of the PHELIX laser system, nanoseconds prior to the peak intensity, which is normalized to the maximum intensity of the laser pulse. The red dashed line indicates the amplified spontaneous emission (ASE) plateau which contains some prepulses, indicated in black. The intensity gradually increases a few hundred picoseconds up to the pulse maximum, known as the rising slope. The rough intensity threshold for ionization of matter is indicated by the grey area.

The profile contains different regions which are created at various stages of a chirped-pulse amplification (CPA) [77] laser system [78, 79]. The long plateau of roughly constant intensity, which occurs nanoseconds to few hundred picoseconds prior to the pulse peak, is created by the amplified spontaneous emission (ASE) within the amplifiers of the system. The ratio between this plateau and the maximum intensity is called ASE-contrast or ns-contrast because of its temporal location.
This plateau often contains local intensity peaks called prepulses, which are pulse replica created by unwanted reflections within the amplification chain [78]. The ratio of the maximum prepulse intensity and the maximum intensity is defined as prepulse contrast.
Close to the pulse peak, the intensity gradually rises until reaching the maximum intensity. This rising slope of the laser pulse extends over a timescale of several hundred times the pulse duration, given by the full width at half maximum (FWHM). This intensity increase is significantly slower than the bandwidth of the laser would allow. Its origin likely lies within the stretcher [80] and it is a signature found at all laser facilities using CPA as an amplification scheme.
When the ionization threshold of the material is reached, the corresponding intensity at this point leads to the creation of a plasma before the peak intensity arrives at the target. This threshold depends on the target material and typically occurs at 10^9 W/cm^2 to 10^{12} W/cm^2 [27, 30]. The time at which this ionization threshold is reached defines the extent and properties of the formed preplasma.
Especially for modern high power laser systems, which are able to reach intensities in excess of 10^{21} W/cm^2 [81], the mentioned ionization threshold can already be exceeded on the nanosecond scale in the presence of a prepulse. It has been shown by many groups that the ionization of the target due to an insufficient prepulse- or ASE-contrast is responsible for the creation of long-scale plasmas [11, 12, 82].
A key parameter of such a preplasma is the electron temperature T_e, which is correlated to the expansion velocity and the plasma scale length L_c [10]. The latter quantity describes the steepness of the plasma density and is given by the ratio of electron density n_e to the spatial derivative of the density at a certain position, which is usually the critical density n_c [27]:

$$L_c = n_e \left(\frac{dn_e}{dx} \right)^{-1} \Bigg|_{n_e = n_c} . \tag{33}$$

The scale length indicates how far a plasma is extended into space, which means that a plasma with a higher scale length experienced a higher expansion. In the assumption of an exponential density profile with $n_e(x) = n_0 \exp(-x/L_c)$, the scale length also corresponds to the distance at which the density has changed by 1/e. A simplified scheme of such a pre-expanded plasma is shown in Fig. 2.8a, where the scale length increases with

expansion time.

Samir *et al.* [83] introduced a simple model, which describes the evolution of a one-dimensional exponential preplasma with a given initial electron temperature T_e into the vacuum. This model assumes an initially quasi neutral plasma slab at which the hot electrons move into vacuum. This creates a quasi-static field that influences the heavier ions and results in a rarefaction wave, moving into the target with the ion sound speed $c_{s,i}$. The expansion velocity linearly rises with increasing distance from the rarefaction point. However, a certain density surface expands with a constant velocity, which can be used to determine the expansion velocity of the critical density position n_c [83]:

$$v_{exp} = c_{s,i}\left[\ln\left(\frac{n_0}{n_c}\right) - 1\right] = \sqrt{\frac{Zk_BT_e}{M_i}}\left[\ln\left(\frac{n_0}{n_c}\right) - 1\right], \tag{34}$$

where n_0 corresponds to the initial maximum electron density. The ion sound speed additionally depends on the charge state Z and mass M_i of the ions and the Boltzmann constant k_B. The assumption of a one-dimensional expansion is only valid if the longitudinal extent of the plasma is much smaller than the transverse size of the plasma, which is often similar ot the size of the laser focal spot.

In reality the density distribution differs from this exponential assumption as it is shown in Fig. 2.8b, and the description becomes more complex. The data is obtained by 2-D hydrodynamic simulations, performed by Bagnoud *et al.* [84].

Even if the mentioned ASE and prepulses could be removed, the rising slope of the laser pulse still leads to the creation of a preplasma. The ionization close to the peak intensity, on the hundreds of picosecond scale, creates a plasma with relatively short scale lengths in the micrometer to sub-micrometer.

The corresponding extent is important for the assumption of a quasi one-dimensional interaction of the laser pulse with the plasma. This is only valid if the movement of the critical density surface during the interaction is small compared to the transverse size of the laser focus. Since the considered scale lengths of the plasmas and the movement of the critical surface is much lower than the focal spot size of 6 µm FWHM, this assumption should be valid within the presented numerical studies. However if the extent of the preplasma is much larger, which could be possible within experimental conditions, this assumption might not necessarily be fulfilled.

All of the presented ion-acceleration mechanisms predict an optimum of the process for different target conditions, ranging from cold and unperturbed targets up to a necessary pre-expansion. As seen in this section, the formation of a preplasma and the corresponding unknown properties, which are present in experimental conditions, lead to a deviation between the predicted and observed outcome. Therefore, a measurement of the preplasma properties close to the maximum of the laser intensity is necessary over a wide

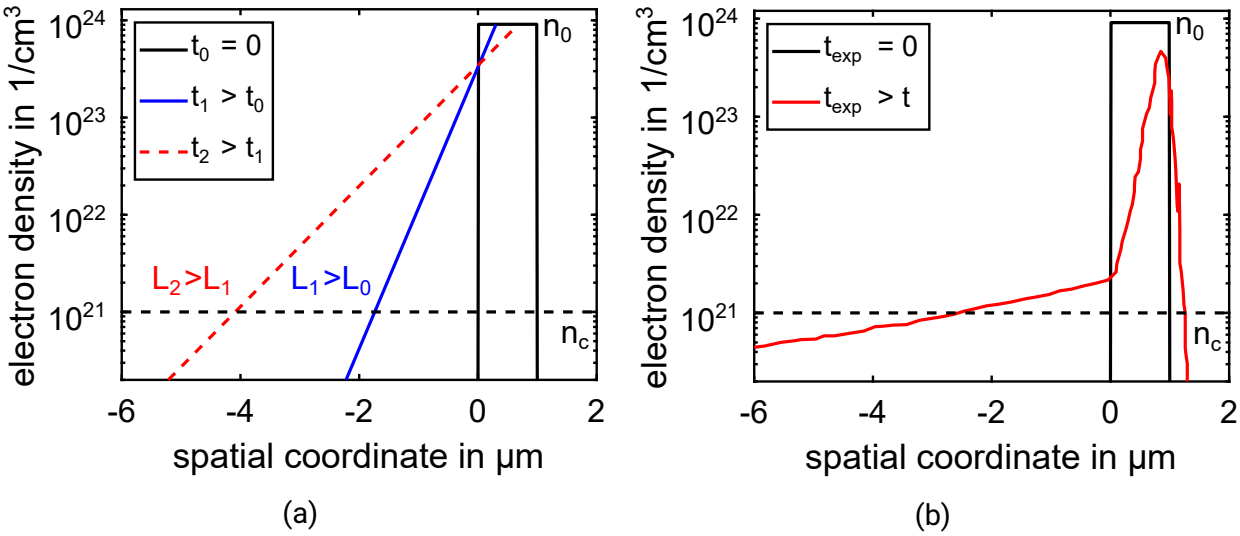

Figure 2.8: (a) Simplified scheme of the spatial electron density distribution with an exponential decay for an expansion time t > t_0, shown in a logarithmic scale. The colors indicate the electron density profile at different expansion times, showing an increasing scale length as the plasma expands. In reality the density distribution cannot solely be described by an exponential function and the preplasma close to the maximum of the laser intensity might correspond to (b). The data is obtained from hydrodynamic simulations done by Bagnoud *et al.* [84].

range of parameters. The possible methods to measure such properties in experimental conditions will be presented in the upcoming section.

3 Preplasma characterization

As shown in the previous sections, the properties of the preplasma are very important for the outcome of the LPI, especially in the case of the advanced laser-ion acceleration schemes. The short time scales of the interaction and strong density gradients make a measurement of the preplasma condition challenging. Most of the current techniques are restricted to plasma conditions with very high density scale lengths, or require additional short-pulse probe beams.
The most used techniques for both conditions will be briefly explained, including the corresponding limitation to the measurements. After that, a complementary method will be presented which is based on the measurement of the reflected light during the LPI, which closes the gap between the current available techniques. This section focuses on the explanation of this method and the corresponding study with the help of numerical 2-D particle-in-cell simulations. The findings will be discussed and summarized at the end of this section.

3.1 Preplasma diagnostics - State of the art

Most of the currently-used standard methods perform either time-integrated measurements or rely on the measurement of a mean density distribution over a certain spatial region of the preplasma. These type of techniques like the side-viewed shadowgraphy and interferometry are used by many facilities and groups [12, 85, 86, 87].
Both methods use a short-pulse probe beam which propagates through the plasma, parallel to the initial target surface, that is created by the driving laser pulse. A snapshot at different interaction times can be taken by temporally delaying the probe pulse with respect to the main pulse. Since the refractive index depends on the plasma density, the effect of different density regions are imprinted into the probe beam. This means that the laser is either blocked when reaching an overcritical region, or accumulates a phase shift while propagating through sub-critical plasma densities. In case of shadowgraphy, only the evolution of the overcritical region is analyzed, which is achieved by imaging the target surface and probe beam onto a camera. The difference of the opaque region at each corresponding probe-pulse delay can be used to calculate the velocity of the expanding plasma.
In contrast to this, interferometry uses the phase shift which is accumulated during the propagation in the undercritical plasma. The probe beam is split up in two parts after the interaction and the region of the beam which passed through the plasma is overlapped with an unaffected region. This creates an interference pattern with a constant fringe spacing if the phase difference between both pulses is constant. The interference fre-

quency changes in case of an accumulated phase-shift, which can be used to calculate the density of the plasma for the undercritical region [85]. With this, the general evolution of the plasma can be determined in contrast to the critical density evolution when using shadowgraphy.
As a matter of illustration, Fig. 3.1 shows a possible implementation for this type of measurement together with the resulting image, which I used during one of the experimental campaigns. The right-hand-side image shows a measurement of a preplasma that is created by an intentionally introduced picosecond prepulse, showing the modulation of the interference pattern, which directly indicates a resolution in the micrometer range. The setup can be adapted to shadowgraphy by removing the interferometer in front of the camera.

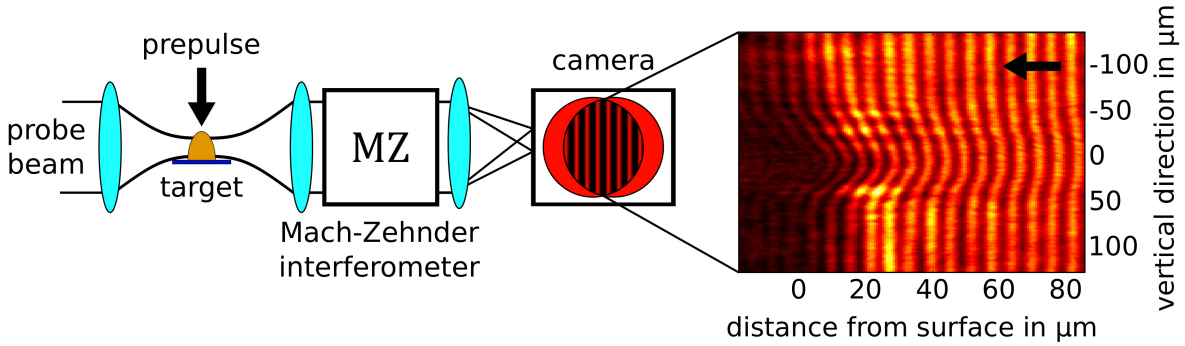

Figure 3.1: Schematic setup of the interferometry at which the probe beam is incident on the plasma, parallel to the initial target surface. The interaction region is imaged onto a camera after passing a Mach-Zehnder interferometer, which leads to an interference pattern. An example for such a measurement is shown on the right hand side, showing a modulation of this created interference pattern. The black arrows indicate the direction of the plasma-creating laser pulse.

Such a side-viewed measurement leads to a temporal averaging of the expansion over the probe beam's pulse duration and an integration of the spatial extent of the preplasma with respect to the propagation direction of the probe beam.
Both methods enable the possibility to directly determine the expansion velocity of the plasma with multiple measurements. An improvement to this can be achieved by including time-resolved information about the evolution, when using a temporally chirped probe beam. This spreads the spectral components of the pulse over the temporal evolution, which enables the direct correlation of a distinct time to a certain wavelength.
Therefore, every spectral component of the probe beam can be correlated to a specific interaction time between the plasma and the pulse. This leads to an imprint of the temporal evolution of the plasma into the spectrum of the chirped probe pulse. By resolving this pulse with a two-dimensional spectrometer, the wavelength axis can be correlated to

the interaction time and the perpendicular axis corresponds to the spatial extent of the plasma.
A general difficulty with this type of measurement arises from the large background signal which is created during the interaction of the main laser pulse with the plasma. This can occur because of the scattering of the main beam or the generation of higher harmonics, whose effect can be decreased when using an off-harmonic probe beam and interference filters [88].
The biggest limitation for this type of measurement arises from the spatial resolution. The best resolution that is reachable by an optical imaging system is limited by the wavelength of the used probe beam, which is in theory in the micrometer to sub-micrometer range. This is far from being present within the experimental realization due to different effects that alter the resolution. One of these is related to the limited depth of field, which leads to a blurring effect due to the 3-D geometry of the target, especially when foil targets with a transverse extent in the millimeter range are used.
Another effect that arises from small scale lengths, is a lowering of the accessible plasma density. Strong gradients cause a deflection of the beam, which reduces the collection of the light by the first optic of the imaging system. As a result, the edge of the shadow does not correspond to the critical density anymore, which makes the interpretation of the data difficult. Therefore, shadowgraphy and interferometry, with a resolution in the micrometer range [12, 13], are adapted to large scale lengths and are therefore best suited to detect plasmas generated by nanosecond lasers.
Another possibility to measure the preplasma scale length is given by the method of frequency-domain interferometry [14], which requires a probe pulse with a short pulse duration in the femtosecond range. Figure 3.2 shows the schematic of the measurement principle to characterize a plasma that is created by a prepulse with the pulse duration t_{pp}. As a first step, a reference pulse is generated from the probe pulse with a specific delay Δt_{range} between the pulses. These two pulses, with a much larger spot size than the prepulse, are sent onto the target. The general idea is to temporally position the double pulses such that the reference pulse (red) irradiates the target before the prepulse, and the second pulse (blue) probes the created plasma. The reference and probe pulses are now imaged onto the entrance slit of a spectrograph, and the signal is recorded by a camera. The pulses create an interference pattern $I(\omega)$, depending on the time delay between both pulses Δt_{range} and the angular frequency of the laser pulse ω, which can be described by [14]:

$$I(\omega) = I_0(\omega)[1 + R + 2\sqrt{R}\cos(\omega\,\Delta t_{range} + \Delta\varphi)]. \tag{35}$$

During the interaction with the plasma, the intensity of the probe pulse reduces by the factor R and the plasma imprints a spatially varying phase shift $\Delta\varphi$, which changes the oscil-

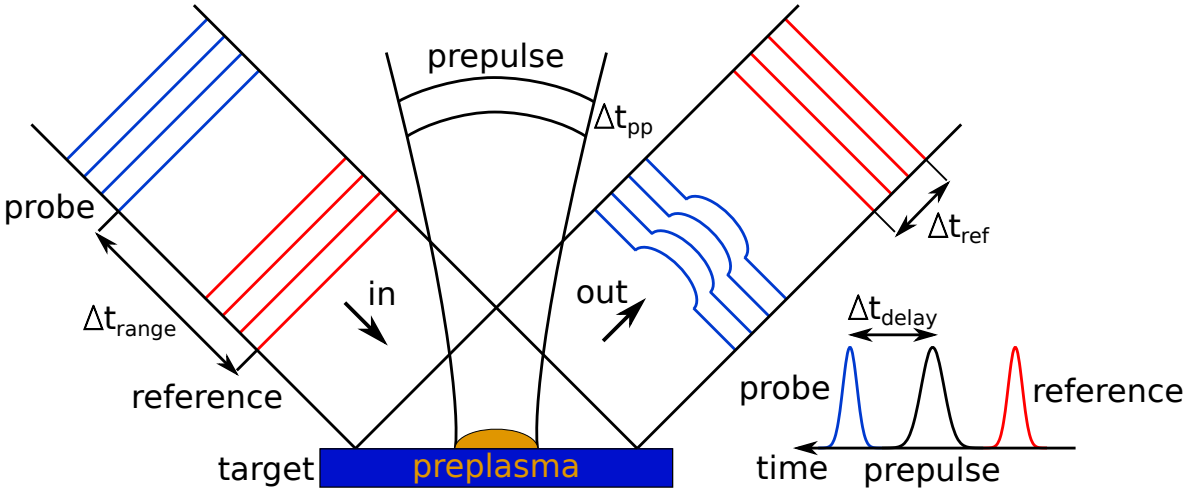

Figure 3.2: Schematic principle of frequency-domain interferometry, at which a short reference and probe pulse are sent onto a target that is irradiated by a prepulse. The two pulses are temporally positioned such that the prepulse interacts with the target after the reference pulse is reflected, but before the probe pulse arrives at the target. The spatial modulation by the preplasma is now imprinted into the probe beam.

lation frequency. By performing the inverse Fourier-transform, this shift can be extracted from the spectrogram, which corresponds to the shift of the critical density position at a given time Δt_{delay}. This time is determined by the difference between the prepulse and the probe beam, and the expansion of the plasma can be monitored by varying this time difference.
The information about the expansion of the preplasma is averaged over the probe pulse duration Δt_{ref}, showing the need for a very short pulse duration. This method has been used by Kahaly *et. al.* [15] to determine the scale length of an induced preplasma and the corresponding influence on the generation of surface high harmonics.
The described measurement techniques are either able to measure long scale length preplasmas or require the access to a short-pulse probe beam, which is not present at every laser facility. For this reason a new approach to measure the preplasma properties has been developed.

3.2 Principle of the reflection measurement

The previously-cited techniques cover either the measurement of long plasma scale lengths, or require a probe beam with a pulse duration in the femtosecond regime, which is not accessible at every laser system. A promising principle to determine the preplasma properties in the short scale-length region is the spectral measurement of the reflected light during the LPI. The central idea explored in the following is that a strong correlation

between the plasma scale length and the movement of the critical plasma density position exists. In addition, the corresponding velocity imprints a Doppler shift to the reflected light, which can be measured using a time-resolved laser-pulse diagnostic. The principle of this non-invasive method which does not require any further probe beams will be briefly presented.

A heuristic representation for this velocity evolution of the critical plasma density during the interaction of a relativistic laser pulse with a pre-expanded target is shown in the upper graph of Fig. 3.3. Regions below and above the solid horizontal line correspond to a movement towards the laser and away from the laser, respectively. The intensity at the critical density for the different interaction times can be seen in the lower graph. The pressure of the laser pulse and the plasma is indicated by the red and yellow lines respectively.

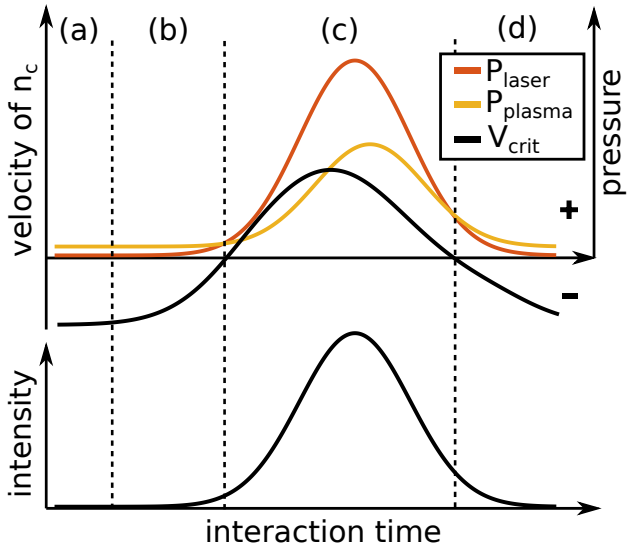

Figure 3.3: Schematic representation of the velocity evolution of the critical density n_c (black upper graph) during the interaction with a laser pulse (lower graph). The pressure of the laser pulse and the plasma, with opposing sign, are indicated by the red and yellow lines. The different amplitude of the laser and plasma pressure at different times results in a movement of the critical density. The different resulting regions can be distinguished, from the free plasma expansion (a) to the onset of HB (b). The HB increases up to a maximum velocity until the plasma pressure starts to increase (c). When the density limit is reached, the pressure again overcomes the light pressure (d).

At early times, when the light pressure is low compared to the pressure of the expanding plasma, the critical density moves towards the laser, which results in a negative velocity (Fig. 3.3a). This expansion velocity is compensated when the laser intensity starts to increase (Fig. 3.3b), until the laser enters the HB phase when the intensity is sufficient to overcome the plasma pressure (Fig. 3.3c). This accelerates the critical density in laser-direction until it reaches the maximum HB velocity. After this the increasing pressure of

the heated plasma slows down the HB process until the density limit, described in Eq. 21, is reached. At this point the plasma pressure overcomes the radiation pressure, again resulting in a movement towards the laser (Fig. 3.3d).
Since the laser pulse is reflected at the critical density, which introduces a Doppler shift, its movement is imprinted into the interacting laser pulse. However, this effect is only directly visible if there are no further sources of spectral distortions that interfere with the spectral changes introduced by the Doppler effect.
Another spectral shifting and modulation process, which is not correlated to the movement of the critical surface, is the (relativistic-) self-phase modulation (SPM). This effect is introduced because of a phase-change of a laser pulse in the presence of a time dependent index of refraction [89], which is given by Eq. 7 in the presence of a plasma. Since the critical density changes with the intensity (Eq. 13) and the plasma density varies during the interaction, the index of refraction is also temporally varying.
The resulting electron density distribution $n_e(x,t)$ and the corresponding position of the critical density x_c, up to which the laser can propagate, can be used to describe the temporal phase of the laser pulse:

$$\varphi(t) = \frac{\omega}{c}\int_0^{x_c} \eta(x,t)\,dx = \frac{\omega}{c}\int_0^{x_c}\sqrt{1-\frac{n_e(x,t)}{\gamma(t)n_c}}\,dx. \tag{36}$$

Here, ω corresponds to the angular frequency of the laser with the speed of light c, and the relativistic critical density $\gamma(t)n_c$ [90]. Since the temporal phase and spectrum of the laser pulse are connected, this temporally varying phase leads to a spectral modification [89]. Only if this effect is negligible compared to the Doppler effect, the spectral change of the laser pulse during the interaction is dominated by the moving critical density. Using intensities of 5×10^{19} W/cm^2 and a density profile that was calculated using hydrodynamic simulations, Ping *et al.* [39] showed that this effect is at least 3 times smaller than the spectral modulation from the Doppler shift.
With this important assumption, which is addressed in Sec. 3.3.6, the movement of the critical surface can be directly extracted from the laser pulse after the interaction. According to the schematic movement, shown in Fig. 3.3, this results in a blue-shifted laser spectrum for the regions (a), (b) and (d) and a red-shifted spectrum in during region (c). Especially at the onset of the interaction, when the movement is plasma-dominated and marginally influenced by the laser pulse, the spectral properties contain information about the preplasma properties.
Such type of measurement yields a non-invasive method which is relatively easy to set up, since only the reflected pulse during the interaction has to be measured in a temporally-resolved manner. Therefore, no secondary probe-beams are needed for this type of diagnostic. The mentioned correlation between the preplasma properties and spectral behav-

ior is verified by performing numerical simulations, with emphasis placed on the study of the influence on the regions (a) and (b) from Fig. 3.3 with respect to the interaction conditions given by the laser and preplasma parameters.

3.3 Numerical study of laser interaction with high-gradient plasmas

This section focuses on the description of the two-dimensional numerical simulations and the following analysis of the reflected spectra. At first, the simulated scenario will be introduced, followed by a description of the chosen simulation parameters. In Sec. 3.3.4, the general analysis of the reflected laser field is presented, including the necessary tools. The correlation between the movement of the critical density and the spectral changes is shown and the effect of different laser and plasma parameters on this spectral changes are studied. The findings of this section are afterwards discussed in Sec. 3.3.10.

3.3.1 Description of the simulation

The simplified scheme of the 2-D simulations is shown in Fig. 3.4, whereas the upper half represents the top view and the lower half shows the intersection on the laser axis. A laser pulse is focused onto a target with different preplasma properties, whereas the incidence angle is varied. During the interaction, a part of the laser pulse is reflected at the critical density, which is analyzed later on. The general scenario of the simulation is kept throughout this thesis, whereas only certain laser and plasma parameters are changed between each simulation. For a later comparison with the performed experiment, the properties of the laser pulse were kept as close as possible to the experimental conditions present at PHELIX (Sec. 4), whereas the differences are discussed in Sec. 3.3.3.
The s-polarized laser pulse with a central wavelength of 1053 nm, a pulse duration of Δt = 250 fs (FWHM) and varying intensity ranging from 10^{18} W/cm^2 to 10^{21} W/cm^2 is focused to a spot size of D = 6 µm (FWHM). The laser pulse, which propagates parallel to the x-axis, interacts with an opaque target of solid density. The target, consists of carbon (C) and hydrogen (H) with a corresponding C:H ratio of 1:2 and has an initial peak electron density of $n_{e,0} = 4 \times 10^{23}$ cm^{-3} and a target thickness of d = 1 µm. The incidence angle Θ between laser and target is chosen between 0° or 30°, which also changes the direction of the reflected laser pulse after the interaction.
To account for different expansion states and therefore scale lengths of the target, the initial electron distribution is assumed to have a uniform temperature $T_{e,ini}$, which is varied between 10 eV and 7 keV, whilst still assuming a fully ionized CH_2 target. This assumption is used to avoid the influence of different ionization states, which will be discussed in Sec. 3.3.10. The coldest target only showed a minor effect of numerical heating [76], which

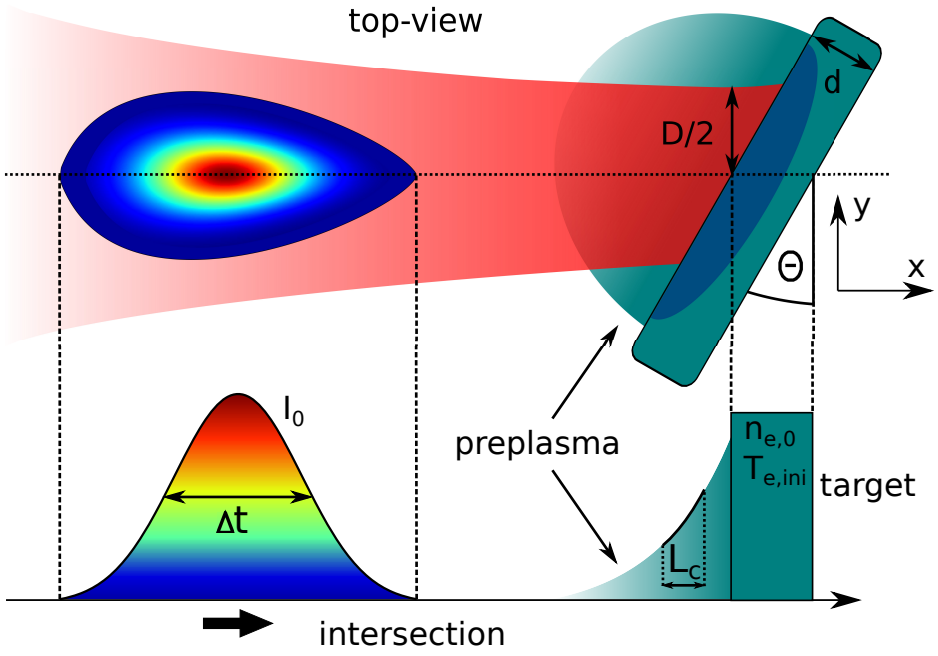

Figure 3.4: Schematic of the interaction of a laser pulse with a target of different expansion states, identifying key simulation parameters. The upper half of the image shows the top view and the lower half represents the intersection on the laser axis. A laser pulse with a given intensity I_0 and pulse duration Δt is focused to spot size D onto the target surface. The target with an initial thickness d, electron density n_e and temperature $T_{e,ini}$ is rotated by an angle Θ with respect to the laser propagation direction. The initial temperature leads to the formation of a preplasma with a certain scale length, which affects the LPI.

increased the temperature by only 5 % at the vacuum-density boundary. Due to the time difference between simulation start and the arrival of the pulse at the target surface, the initial density distribution expands into the vacuum, while increasing the effective target thickness and scale length L_c in dependence on the initial temperature. The laser and target parameters chosen to perform the simulations are summarized in Tab. 1.

I_L in W/cm^2	λ_0 in nm	Δt in fs	D in µm	d in µm	$T_{e,ini}$ in eV	$n_{e,0}$ in cm^{-3}
10^{18}-10^{21}	1053	250	6	1	10 - 7000	4×10^{23}

Table 1: Laser and target parameter for the 2-D PIC simulations

The described simulation principle and the constraints to the laser and plasma is transferred to the 2-D PIC simulation. The exact parameters used for the simulation will be described in the following section.

3.3.2 Particle-in-Cell simulation and parameters

The simulations were performed with the 2-D-PIC code EPOCH [76] on the Kronos cluster at the GSI Helmholtzzentrum für Schwerionenforschung GmbH. As mentioned in Sec. 2.4 the Debye length of the system should be resolved by the simulation. In presence of a high electron density and sometimes very low temperatures, the Debye length can reach the picometer range, which would require a very high amount of cells within the simulation, which would extend the simulation time beyond the current possibilities. To find the best trade-off between resolution and computational resources while ensuring a physically reliable simulation, a 1-D convergence test was done prior to the simulation, which is described in detail in Sec. A. 1, indicating that a resolution of 12 nm in laser direction is sufficient.
As mentioned in the previous section, the incidence angle between laser and target is varied. To ensure that the electric field after the interaction does not escape the simulation box and is completely contained within the boundaries, the extent and resolution of the simulation is adapted, depending on the interaction angle. The parameters, including the different expansion times and dynamic ranges of the incoming laser, are shown in Tab. 2. These parameters are kept for the simulations throughout this thesis. The change of any simulation parameters will be mentioned at the appropriate point.

angle	grid cells x,y	extent [x],[y] (µm)	resolution (nm)	$I(t = 0)/I_{max}$	t_{arr}
0°	27500×8912	[-320,10] , [-80,80]	12×19.5	10^{-4}	1150 fs
30°	17000×27648	[205,30] , [-50,250]	12.1×10.9	10^{-6}	600 fs

Table 2: This table shows the different simulation parameters depending on the chosen incidence angle between laser and target, showing the grid size in x and y direction, with the corresponding window size and resolution. The intensity ratio of the incoming laser pulse at the time t = 0 is given by $I(t = 0)/I_{max}$ and the time of arrival at the target surface and therefore the expansion time corresponds to t_{arr}.

In case of normal incidence (0°) the simulations are performed with a spatial resolution of 12 nm in the direction of the initial laser propagation, and 19.5 nm perpendicular to it. This leads to a simulation box containing 27500 x 8192 cells and a spatial window ranging from -320 µm to 10 µm in x- and -80 µm to 80 µm in y-direction, where x = 0 and y = 0 corresponds to the focus position of the laser pulse. When increasing the angle to 30° the resolution of the y-axis is increased to 10.9 nm, resulting in 17000 x 27648 cells which adds up to a spatial window that ranges from -175 µm to 30 µm in x- and -50 µm to 250 µm in y-direction. The total amount of macro particles within the simulation box was kept constant for every type of simulation with $\approx 2 \times 10^9$. The number of cells in Y-direction

was always chosen to be divisible by 1024, corresponding to the number of cores that were usable for each simulation, which results in different resolutions.
The truncated Gaussian laser pulse enters the described simulation box at the negative x-border, with an initial intensity ratio $I(t = 0)/I_{max}$ of 10^{-4} to 10^{-6}, depending on the conducted simulation, at the simulation time t = 0 fs. Since the intensity jumps from zero up to the mentioned intensity ratio at the beginning of the simulation, this dynamic range defines which times of the laser pulse can be used for the analysis described in Sec. 3.3.4.
The laser pulse itself is described by a Gaussian beam, which is focused to a spot size of 6 µm (FWHM) at the target front surface, initially located at x = 0 µm. The converging Gaussian beam within the simulation is described by [91]

$$E(y,x) = E_0 \frac{w_0}{w(x)} \exp\left(-\frac{y^2}{w(x)^2}\right) \exp\left(i\left[\zeta(x) - kx - k\frac{y^2}{2R(x)}\right]\right), \tag{37}$$

$$\text{with} \quad w(x) = w_0 \sqrt{1 + \left(\frac{x}{x_R}\right)^2},$$

$$\text{and} \quad R(x) = x\left(1 + \left(\frac{x_R}{x}\right)^2\right),$$

with the initial field strength E_0 which is proportional to $\sqrt{I_0}$. The waist of the beam at the focus position and at every longitudinal position, depending on the Rayleigh length $x_R = \pi w_0^2/\lambda$ for a given laser wavelength λ, is given by w_0 and $w(x)$ respectively. The parameter R(x) describes the radius of curvature of the wavefront at every position with a given wave-number $k = 2\pi/\lambda_0$ and the Gouy-phase $\zeta(x)$. Depending on the extent of the simulation box, the laser impact occurs at $\approx$1150 fs for normal incidence and $\approx$ 600 fs for an incidence angle of 30°.
As already mentioned, the time difference between simulation start and laser impact leads to a pre-expansion of the target and therefore changes the initial density distribution. An example for the resulting electron density distributions at an incidence angle of 0°, an expansion time of 1150 fs and different initial electron temperatures $T_{e,ini}$ are shown in Fig. 3.5. It is visible that the scale length L_c of the preplasma increases for higher electron temperatures due to the increased expansion velocity.
During the interaction with the plasma, a part of the laser pulse is reflected at the critical density, whereas the angle of reflection is given by approximately twice the reflection angle Θ. The simplified representation of the reflected laser pulse is proposed in Fig. 3.6 with the corresponding intersection in specular direction.
The specular direction defines the region of the reflected laser pulse, which is used to extract the temporal resolved Doppler shift from the field data that is generated by the PIC simulation. Since only the central region of the reflected beam in specular direction is

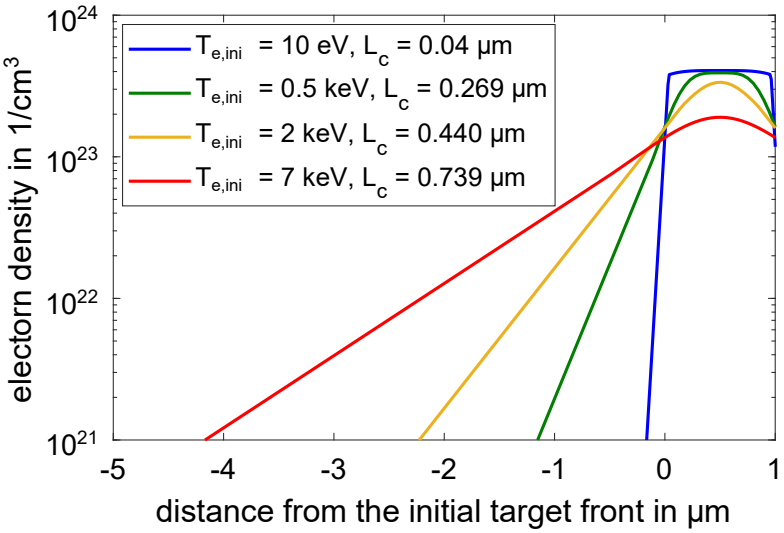

Figure 3.5: The colored lines show the lineout of the electron density distribution, in direction of the target normal, which is obtained for an expansion time of 1150 fs and different initial electron temperatures. This leads to different expansion states and preplasma scale lengths depending on the expansion time and temperature.

accessible experimentally, this direction has been chosen to directly compare the results to the experimental conditions.

3.3.3 Difference between the numerical and experimental conditions

As already mentioned, I chose the parameters for the 2-D PIC simulation that are as close as possible to the experimental ones. Besides the reduced dimensionality of the interaction, not every condition can be met within the simulation. An exception is made in case of the laser pulse duration, which is reduced to 250 fs in comparison to a pulse duration of 500 fs in experimental conditions.
Lowering the pulse duration also reduces the time and resources needed for the simulation, since an increase of the pulse duration by a factor of two, would increase the simulation time by the same amount. In addition, the size of the simulation box has to be doubled to completely contain the electric field after the interaction, which further increases the computation time by at least a factor of 4. In total, this increases the computation time at least by a factor of 8, resulting in $\approx$ 350.000 CPU hours, which would exceed the currently utilizable time of the computing cluster by over a factor of 2. Since the reduced pulse duration is still of the same order of magnitude, the principal behavior of the interaction should not change, but only accelerate the dynamics, which will be discussed in Sec. 3.3.10. In addition to the reduced pulse duration, the laser pulse is also truncated at low intensities, as mentioned in the previous section, which is not the case in realistic

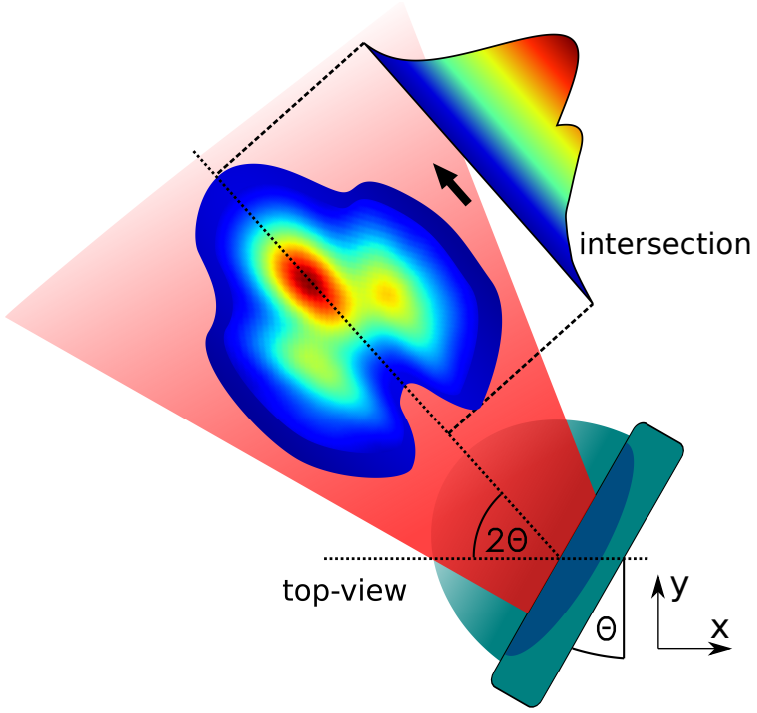

Figure 3.6: Simplified scheme, showing the top view of the reflected laser pulse after the interaction with the plasma. The specular direction of the reflected pulse is indicated by the dashed line, which is approximately given by twice the angle of incidence Θ.

conditions where the intensity distribution transitions into the rising slope and eventually into the ASE plateau of the laser pulse profile on the nanosecond scale (Sec. 2.5).
The interaction of these intensity regions with a cold target requires the simulation of different absorption mechanisms, like inverse bremsstrahlung (Sec. 2.2.3) that rely on collisional mechanisms, which are not included within the performed simulation, and would have to be simulated over time scales of nanoseconds. This is the reason why the initial plasma parameters have to be initially set within the simulation, resulting in a correlation between initial temperature and scale length, which is a further difference between the simulation and experimental conditions.
The preplasma scale length and initial electron temperature are coupled within the simulation and effects like profile steepening are neglected, which might occur during the preplasma creation. This limits the accessible range of parameters that are studied with the conducted PIC simulations. The coupling of scale length and temperature is not necessarily given in experimental conditions, which shows that it is absolutely necessary to measure the temperature and scale length of the preplasma separately.
Additionally, the expansion of the plasma is assumed to be one-dimensional with a uniform density in the direction normal to the initial target surface. This assumption is valid in experimental conditions if the transverse extent of the plasma is much longer than the extent in laser direction, or if the laser spot is much larger than the skin depth [25].

With these differences in mind, the simulation results can be studied by analyzing the field obtained from the simulation. The analysis, including the necessary tools, will be described in the following sections.

3.3.4 Characterization of the time-resolved Doppler shift

To correlate the temporal and spectral changes of the laser pulse during the interaction, the temporal phase has to be extracted from the electric field. This procedure will be explained in the following section, including the mathematical description of the laser field. The simulation returns a two-dimensional electric field, where the wave nature of the field can be recognized in areas of low plasma densities, i.e. far away from the target surface. This real oscillation can be transformed into the complex domain to treat the amplitude and oscillation of the field separately. The resulting 2-D complex amplitude $E(\vec{r}, t)$ can be described by

$$E(\vec{r}, t) = \sqrt{I(\vec{r}, t)}\, e^{i(\vec{k}\cdot\vec{r}+\omega_0 t-\varphi(t))}, \tag{38}$$

with the intensity $I(\vec{r}, t)$ and the temporal phase with the central angular frequency ω_0 and a temporally-varying term $\varphi(t)$. If the distance of the pulse from the focal region is bigger than the Rayleigh length and the laser pulse has left the plasma, a propagation of the wave vector simply corresponds to a shift in time. Therefore, the spatial and temporal components of Eq. 38 can be separated and the field along the specular direction can be taken. The resulting field can now be described by a temporally-varying plane wave, which is given by:

$$E(t) = \sqrt{I(t)}\, e^{i(\omega_0 t-\varphi(t))}, \tag{39}$$

with the time-dependent intensity $I(t)$, the central angular frequency ω_0 and the phase term $\varphi(t)$, which describes the temporal development of the laser frequency. Similar to the temporal description, the pulse can also be defined in the spectral domain by a Fourier transform of the complex temporal electric field

$$\tilde{E}(\omega) = N \int_{-\infty}^{\infty} E(t) e^{-i\omega t} dt, \tag{40}$$

with the normalization factor of the Fourier transform N. The pulse can now be described by its spectrum $S(\omega)$ and the corresponding spectral phase $\varphi(\omega)$:

$$\tilde{E}(\omega) = \sqrt{S(\omega)} e^{i\varphi(\omega)}. \tag{41}$$

Even though both descriptions contain the same information about the laser pulse, the temporal phase will mainly be used in the further analysis to calculate the frequency evo-

lution within the pulse. This so-called instantaneous frequency is given by the temporal derivative of the phase [89]

$$\omega_{inst} = \omega_0 - \frac{d}{dt}\varphi(t), \tag{42}$$

which describes the deviation from the central wavelength at every point in time within the pulse.

This temporal behavior can be visualized by the Wigner-Ville distribution (WVD) [92], a time-frequency representation of the complex laser field, which maps the frequency and time of a laser field in an intuitive way. This is given by the Fourier-transform of the autocorrelation function of the signal, whereas in contrast to the regular autocorrelation, both signals are temporally delayed against each other [92].

$$W(t,f) = \int_{-\infty}^{\infty} E(t+\frac{\tau}{2})E^*(t-\frac{\tau}{2})e^{-2\pi i\tau f}d\tau \tag{43}$$

This represents the spectral density of the signal at each time. An example for the absolute of such a distribution can be seen in Fig. 3.7a, showing a pulse with a quadratic spectral phase, leading to a linear rising wavelength with time and a cubic spectral phase in Fig. 3.7b, leading to a more complex change of the frequency over time.

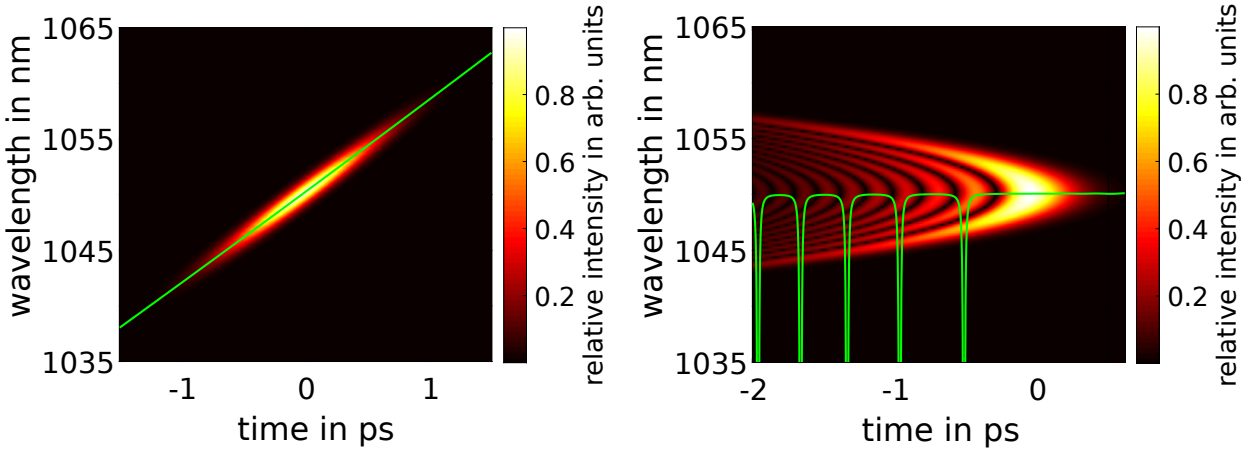

Figure 3.7: (a) An example of the absolute of the WVD for a laser pulse with a quadratic spectral phase, leading to a linear rising wavelength with time, indicated by the instantaneous wavelength calculated directly from the laser field (green). (b) A laser pulse with a cubic spectral phase in combination with the corresponding instantaneous wavelength is shown. Since two frequencies occur at the same time a beating effect occurs which leads to an ambiguous instantaneous wavelength. In this case the WVD is more meaningful than the instantaneous wavelength.

The instantaneous frequency can also be extracted from the WVD by calculating the first moment of the spectral density for each time step, which is similar to calculating the instantaneous frequency from Eq. 42. The corresponding transformed instantaneous wavelength is indicated by the green lines in Fig. 3.7. In case of a more complex phase, where two different frequency components occur at the same time, a beating effect occurs which leads to an ambiguous instantaneous wavelength. In this case, the instantaneous wavelength is only of limited use and the complete WVD reveals more information about the temporal change of the spectrum.

3.3.5 Filtering of the electric field

Before the electric field from the simulation can be used to calculate the instantaneous wavelength or WVD, the spectrum has to be filtered.
This is necessary if the field contains noise, for example introduced by a hard intensity-cutoff within the simulation or higher harmonics, which results in fast oscillations in the phase and amplitude. An example for the complete spectrum after the interaction with a plasma is shown by the blue curve in Fig. 3.8.

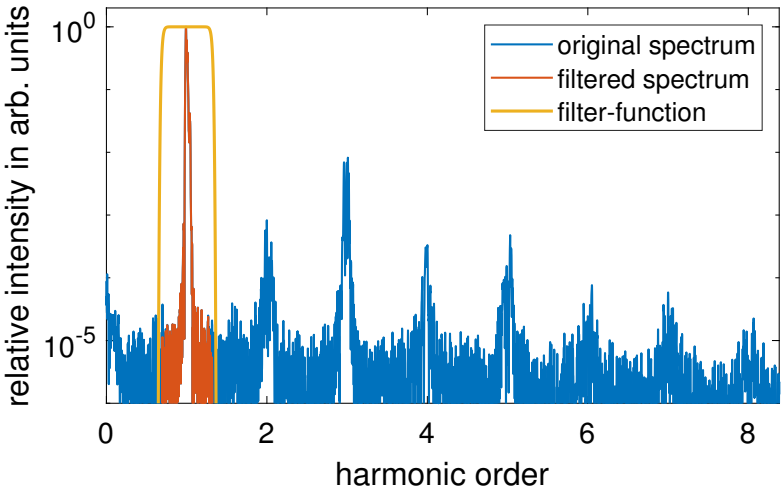

Figure 3.8: The spectrum of the field extracted from the simulation containing noise and additional components introduced by higher harmonics (blue). A spectral band-pass filter with a super Gaussian form (yellow) is used to only retain the signal around the central angular frequency of $1\,\omega$ in a range of $\pm\,0.4\,\mathrm{fs}^{-1}$.

To remove such features, the temporal phase and amplitude of the pulse are either smoothed by using a moving average in the temporal domain, or by using a spectral band-pass filter to suppress the higher harmonics. Such a band-pass filter, as it is used in the later analysis, is shown in Fig. 3.8. Both operations are equivalent if the window shapes are chosen accordingly.

After removing the noise and higher harmonics, the field can be used for the further analysis of the simulation.

3.3.6 Correlation between critical-surface velocity and Doppler shift

The first step is to correlate the movement of the critical density with the introduced spectral shift by the Doppler effect, which has been shown by Thaury *et. al.* [93] with a slightly different approach as presented here. The first step is to monitor the density change throughout the simulation. This is done by drawing a density lineout normal to the target surface for every time step, which has to be done because of the two-dimensional nature of the simulation. An example for the temporal change of the density for an incidence angle of 0° is shown on the left-hand side in Fig. 3.9, whereby the temporal axis has been interpolated for a better visibility.

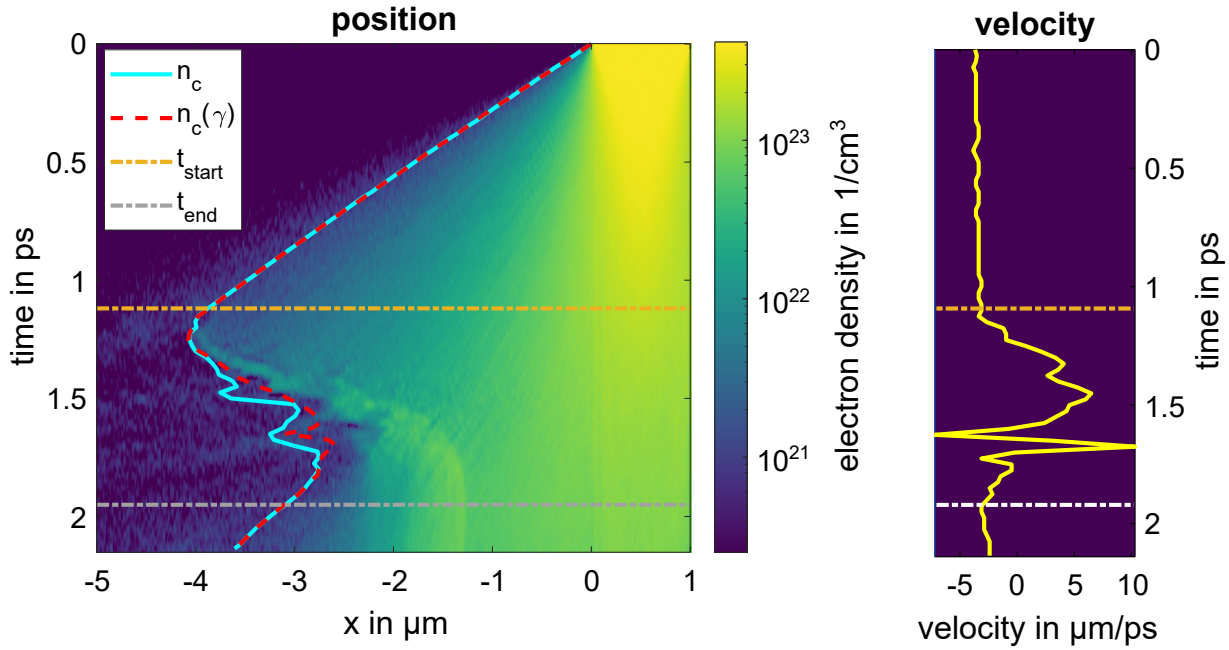

Figure 3.9: Temporal density change during the simulation, normal to the initial target surface (left). The light-blue line shows the movement of the classical critical plasma density and the red dashed line shows the gamma-corrected movement, depending on the laser-intensity. The start and end of the LPI is indicated by the dashed orange and dashed gray line respectively. The right-hand side shows the corresponding velocity evolution of the relativistic critical density over simulation time. The simulation has been performed for a peak laser intensity of 10^{20} W/cm^2, with a intensity of 10^{16} W/cm^2 at the beginning of the interaction and an electron temperature of 7 keV. The temporal axis of the density evolution has been interpolated for a better visibility.

The vertical axis corresponds to the simulation time and the horizontal axis corresponds

to the spatial coordinate with respect to the initial target surface at x = 0 µm. The laser hits the plasma from the left-hand side at ≈1.1 ps (orange dashed line) and ends at ≈1.95 ps (gray dashed line). The light-blue line describes the position of the classical critical plasma density and the red dashed line is corrected by the relativistic gamma-factor, calculated with the laser intensity that is present at this time and position. The critical density is moving in laser direction during the expansion phase of the hot plasma. Shortly after the arrival, the laser pulse overcomes the pressure of the plasma and therefore pushes the critical density into the target. This occurs until the light pressure is not sufficient to further penetrate the plasma, which corresponds to the HB density limit. After this point the critical density again moves towards the laser because of the increased pressure of the heated plasma. The velocity of the critical point at every time step can be calculated from this position change. This is shown on the right-hand side in Fig. 3.9, revealing a similar behavior as already shown in Fig. 3.3.
The method of using only the density lineout on-axis is error prone to possible fluctuations within the density which can occur due to the movement of macro particles from outer regions into the analyzed path. The impact can either be seen by the small oscillations in the expansion velocity or strong velocity changes like the ones shown at ≈1.6 ps. This effect is reduced, but not eliminated, when calculating the mean movement over a transverse region, which is smaller than the focal spot size, around the target-normal axis. To show that the frequency change is indeed caused by the moving critical density, the induced Doppler shift, that a wave would experience during the reflection at this position, can be calculated from the velocity of the critical density by using Eq. 22.
An example of a resulting wavelength change for an initial electron temperature of 7 keV, a laser intensity of 10^{19} W/cm^2 and an incidence angle of 0° can be seen in Fig. 3.10, which is indicated by the blue dots. Each point corresponds to an analyzed time step of the simulation, which limits the number of velocity points that can be calculated directly from the position of the critical plasma density. The corresponding uncertainty is given by the fluctuation of the velocity during the expansion phase and is kept for the complete interaction time, even though the uncertainty might be larger during the interaction with the laser pulse.
This shift introduced by the critical point is compared to the instantaneous wavelength of the reflected laser pulse, which is given by the red line in Fig. 3.10 for a peak laser intensity of 10^{19} W/cm^2 (black line) and an initial electron temperature of 7 keV. The vertical dashed orange and gray line again correspond to the approximate start and end of the LPI. It can be seen that the behavior of both shifts is similar, confirming that the instantaneous wavelength can be used to represent the velocity change of the critical position.
This correlation is visible for all performed simulations, independent of the used scale lengths and laser intensities, which leads to the conclusion that the complete movement

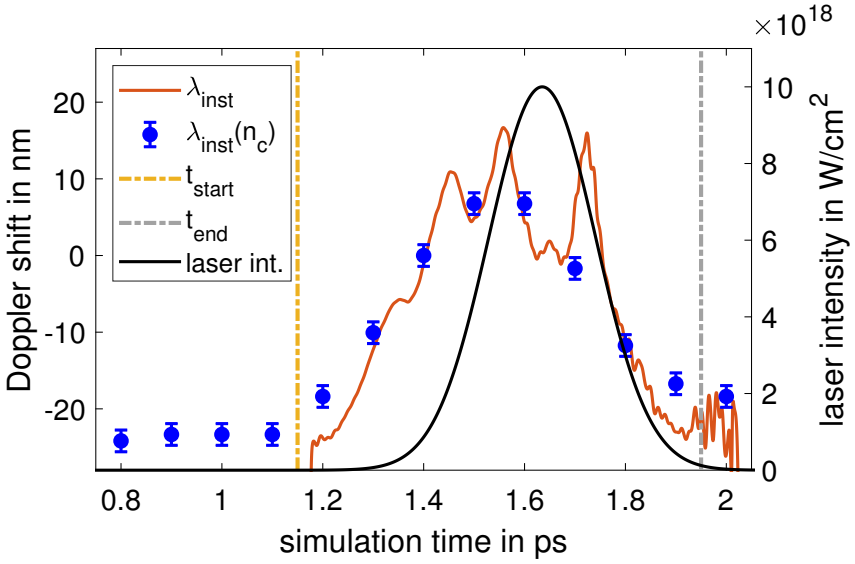

Figure 3.10: Comparison of the expected Doppler shift calculated from the velocity of the critical density location during the simulation (blue dots) and the instantaneous wavelength of the laser pulse which is reflected during the interaction (red). The vertical dashed orange and gray line indicate the approximate start and end of the interaction with the incoming laser pulse (black).

can be approximately reconstructed by analyzing the reflected laser pulse and the effect of SPM plays a minor role for the chosen parameter set. This might not be given for laser intensities that exceed 10^{21} W/cm^2 or longer-scale plasmas, whereby the determination of the exact limit for these parameters is part of future work.
This finding in combination to the continuous movement of the critical density should not allow for the creation of two frequencies at the same interaction time, and therefore suppress the behavior shown in Fig. 3.7b which is leading to an ambiguous instantaneous wavelength. Therefore, sudden jumps in the instantaneous wavelength or beating effects could only be caused by effects like a local relativistic transparency of the density.
The correlation between the movement of the critical density and the Doppler-shift-affected instantaneous wavelength leads to the consequence that a lot of information about the behavior of the plasma can gathered by just analyzing the time-resolved spectral shift of the reflected pulse. The influence of different preplasma properties on the Doppler shift, for the case of a normal incidence angle, is discussed in the following sections. In addition, the possibility of extracting the electron temperature and the plasma scale length from the laser pulse is discussed.

3.3.7 Influence of the preplasma temperature on the Doppler shift

As mentioned in the previous section, the movement of the critical density point can be correlated to the instantaneous wavelength of the reflected laser pulse. Knowing this movement behavior, information about the parameters of the preplasma at the time of the laser pulse arrival can be deduced.
Especially at early times, when the pressure induced by the laser pulse is small compared to the plasma pressure, the wavelength shift is purely dominated by the plasma expansion. This means that the initial wavelength shift corresponds to the expansion of the formed preplasma, and the corresponding velocity can be calculated by the inverse function of Eq. 22.
An example of this behavior is visible in Fig. 3.11, showing the expansion velocity of the plasma for different initial electron temperatures that has been extracted either from the movement of the critical density (blue dots) or from the Doppler shift at the beginning of the reflected pulse (red dots) for a laser intensity of 10^{18} W/cm^2. The simulations were performed for an interaction of normal incidence.

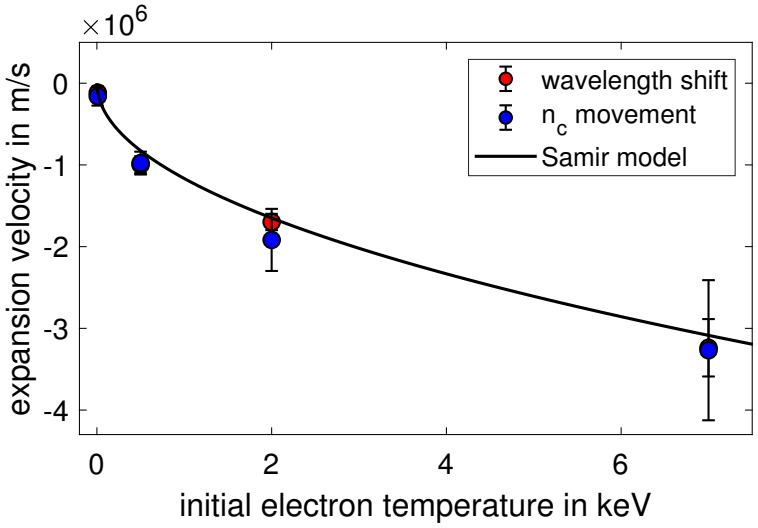

Figure 3.11: The expansion velocity of the preplasma for different initial electron temperatures which are extracted from the simulation either by the velocity calculation of the critical surface (blue) or calculated from the initial blue shift of the instantaneous wavelength (red). The uncertainty is given by the peak to valley (PTV) of the respective minimum and maximum velocity at the beginning of the interaction. The black line corresponds to the calculated expansion velocity by the Samir model (Eq. 34), for the preplasma properties described in Sec. 3.3.1.

The velocity, which is extracted from the Doppler shift, fits the initial velocity of the preplasma quite well in the range of the simulated initial temperatures. This indicates the possibility to use this expansion velocity for extracting an electron temperature. A model

that describes the correlation between the temperature and velocity of an expanding preplasma is given by the Samir model (Eq. 34), introduced in Sec. 2.5.
The resulting expansion velocities for the target parameters described in Sec. 3.3.2 and a constant maximum electron density n_0, is given by the black line in Fig. 3.11. A good agreement between to the extracted velocities is visible. This correlation between temperature and velocity is in good approximation independent of the laser intensity as long as the dynamic range is high enough to observe the region of the undisturbed expanding preplasma.
With the assumption of a one-dimensional expansion of the plasma, this correlation can be used to calculate the electron temperature by rearranging Eq. 34 with respect to the expansion velocity of the preplasma:

$$T_e = \frac{v_{exp}^2 M_i}{Z_i k_B \left[\ln\left(\frac{n_0}{n_c}\right) - 1\right]}. \tag{44}$$

One could think about extracting this initial blue shift from the time-integrated spectrum after the interaction, but the contribution to the total spectrum after the interaction is very small. In addition, the simulations show that this early blue shift can be strongly exceeded by the expansion of the preplasma at late interaction times. This prohibits the use of the lowest wavelength component of the spectrum for the calculation of this expansion velocity, showing the necessity of a time-resolved measurement.
All in all, I believe that a time-resolved measurement of the initial Doppler shift is able to estimate the electron temperature of the plasma, picoseconds prior to the interaction of the peak intensity with the plasma independently from the scale length of the preplasma. To the best of my knowledge, no other measurement technique offers this possibility.

3.3.8 Influence of the preplasma scale length on the Doppler shift

Besides information about the temperature of the preplasma, the spectral properties additionally contain information about the scale length of the plasma, which is described by Eq. 33. As a reminder, a long scale length corresponds to a low density gradient of the plasma, and a short scale length to a large density gradient, which usually corresponds to a plasma with a long or short extent.
The correlation of preplasma temperature and initial wavelength shift is given if the light pressure is low compared to the plasma pressure. If the laser intensity increases, the plasma pressure is overcome which inverts the sign of the instantaneous wavelength change, resulting in a red shift.
This transition between the plasma-dominated and laser-dominated regimes can be observed, similar to the determination of the temperature, at the temporal front of the re-

flected laser pulse. Since the pressure is higher in case of a short scale length the maximum HB velocity, and therefore the maximum red shift is additionally decreased.
An example for this can be seen in Fig. 3.12, showing the extracted velocity from the temporal phase of the pulse after the interaction with a plasma of different scale lengths. The simulation is conducted with a laser intensity of 10^{19} W/cm^2 and an intensity ratio of 10^{-4}. The temperature of the preplasma is kept at T_e =10 eV to avoid any further pre-expansion of the plasma and to neglect the potential effect of the expansion velocity. Only the extent of the preplasma is changed to achieve the shown scale length. Positive velocities correspond to the HB velocity and therefore a red shift. The maximum velocity is higher when the scale length of the preplasma increases and this maximum is reached much faster, which indicates an increased acceleration of the critical surface into the plasma.

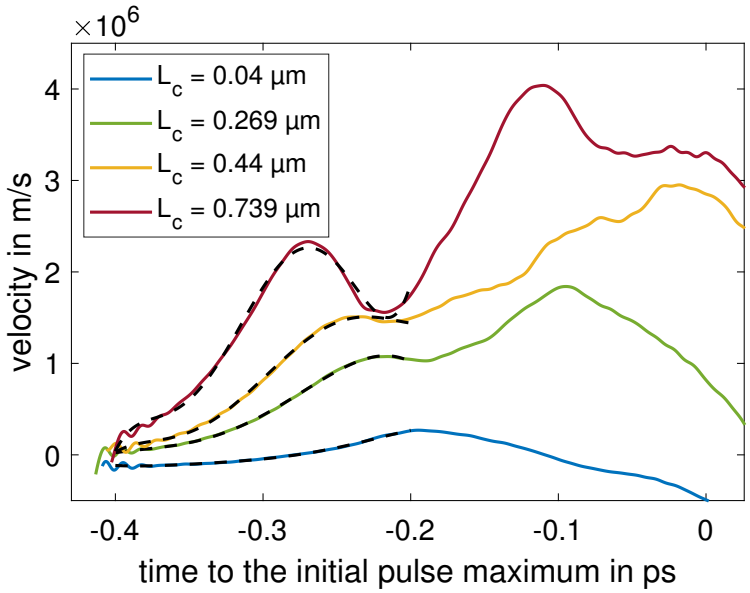

Figure 3.12: Example for the velocity change of the critical surface with the simulation time, whereas the colors indicate different preplasma scale lengths. The initial temperature of the plasma was set to T_e = 10 eV to avoid further expansion and the peak intensity of the laser pulse was kept constant. The maximum HB velocity is higher in case of a long scale length plasma, which indicates a higher acceleration of the critical density. The dashed black lines correspond to a 5th-order polynomial fit which is used to determine the maximum acceleration at the beginning of the interaction, which is determined between 400 fs and 200 fs prior to the initial pulse maximum.

The different curves should reach the same velocity at early times, because of the low initial electron temperature. Since this is not the case for an increasing scale length, this indicates that a dynamic range of 10^{-4} is not sufficient to resolve the plateau introduced by the expansion of the preplasma, which has been introduced in Sec. 3.3.7.

To verify the correlation between acceleration of the critical density surface into the plasma and scale length, the maximum acceleration is extracted from the phase of the laser pulse at the beginning of the interaction, between 400 fs and 200 fs prior to the initial laser pulse maximum, which results in an intensity ratio of 10^{-3} to 10^{-1}. When oscillations in the instantaneous wavelength are present, a second temporal differentiation leads to strong acceleration spikes, which distort this method. Therefore, the velocity extracted from the instantaneous wavelength is fitted by a fifth order polynomial and the corresponding function is used for the further calculations. Examples for the resulting fits are shown by the dashed black lines in Fig. 3.12.
The extracted maximum acceleration for different peak laser intensities and scale lengths is shown in Fig. 3.13, whereas the error is given by the averaged difference between the acceleration from the fit and the derivative of the instantaneous velocity. The color of the dots represents different peak laser intensities from 10^{18} W/cm^2 to 10^{21} W/cm^2.

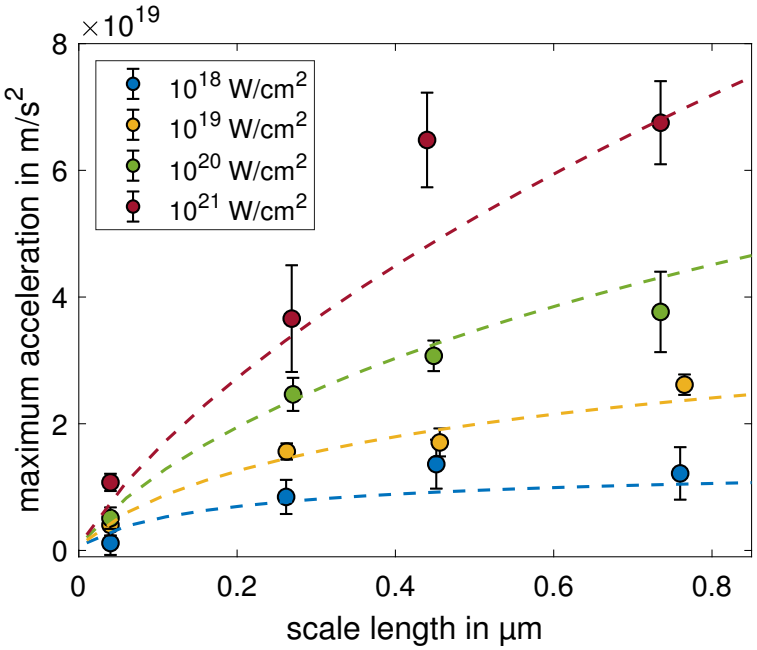

Figure 3.13: Maximum acceleration of the critical density, deduced from the beginning (400 fs to 200 fs prior to the initial laser pulse maximum) of the interaction as a function of the scale length. The color of the dots represents different initial peak laser intensities and the dashed colored lines correspond to the maximum acceleration that is calculated using Eq. 51, for the same scale lengths and laser intensities.

This shows a clear correlation between the maximum HB acceleration at the beginning of the interaction and the preplasma scale length.
Removing the influence of the laser intensity on the correlation between scale length and acceleration, enables a direct correlation. This can be achieved by calculating the temporal derivative of the analytical HB velocity (Eq. 18) for low intensities to determine the

intensity scaling at the beginning of the interaction. For a Gaussian intensity distribution and a one-dimensional interaction, a proportionality of $\sqrt{I}$ can be found, which is described in detail in the appendix A. 2. The resulting intensity-scaled acceleration is shown in Fig. 3.14a, including the same intensities and scale lengths as in Fig. 3.13.

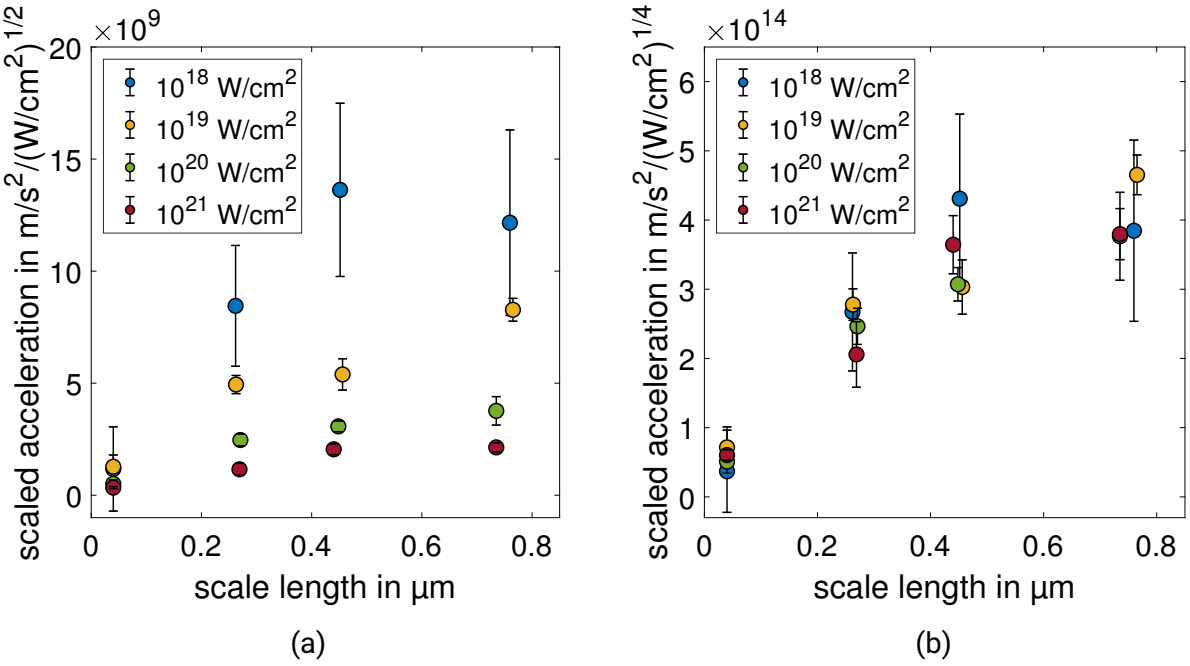

Figure 3.14: (a) Maximum acceleration of the critical density, deduced from beginning of the interaction in dependence of the plasma scale length, which is scaled to the peak laser intensity $\sqrt{I_{max}}$ of each simulation. The color of the dots represent the peak laser intensity of the simulation and the colored dashed lines the corresponding linear fit. (b) A better agreement is given for an intensity scaling of $I_{max}^{1/4}$ which results in a similar slope for all of the intensity data sets.

It can be seen that this scaling overcompensates the laser intensity and does not reduce the spread of data points. Contrarily to the assumption of a square-root scaling, the lowest variance of the deduced acceleration for each scale length and simulation is found for an intensity scaling of $I^{1/4}$, which is shown in Fig. 3.14b. As mentioned in Sec. 2.2.4, the description of the HB velocity by Wilks *et al.* [32] does not take any density gradient into account. Ping *et. al.* [39] already assumed that the electron density gradient of the preplasma influences the movement of the critical density, by slowing down the HB process. For this reason I developed a description of the HB velocity during a one-dimensional interaction with the laser pulse, in the presence of an electron density gradient. The assumption of a quasi one-dimensional interaction is justified for the 2-D simulations since the movement of the critical density surface is below 2 µm, which is much smaller than the focal spot size of 6 µm.

A similar approach has been used by Kemp *et. al.* [94], to calculate the position of the critical density. The derivation is briefly introduced, whereas a detailed description is given in A. 3. The only requirement is that the plasma stays overcritical during the interaction and the temporal derivative of the electron density follows:

$$n_e'(t) = v(t)\frac{dn_e(x(t))}{dx}, \text{whereas} \quad x(t) = \int_{-\infty}^{t} v(t')dt'. \tag{45}$$

At the start, the pressure balance between laser and density flux, given by Eq. 17,

$$2n_i(t)M_i v(t)^2 = (1+R)\frac{I(t)}{c} \tag{46}$$

is used and the ion density is replaced by the spatially and temporally varying electron density $n_i(x(t)) = n_e(x(t))/Z$, including the charge state Z of the ions. The goal is now to find a description of the velocity v(t), which can be achieved by calculating the temporal derivative of Eq. 46. After some rearrangements, this results in a differential equation:

$$v'(t) - \frac{v(t)}{2}\frac{I'(t)}{I(t)} + v(t)^2\frac{1}{2n_e(x(t))}\frac{dn_e(x(t))}{dx} = 0. \tag{47}$$

Solving this equation results in a time-dependent description of the HB velocity v(t):

$$v(t) = \sqrt{I(t)}\left(\int_{-\infty}^{t}\frac{1}{2n_e(x(t'))}\frac{dn_e(x(t'))}{dx}\sqrt{I(t')}dt' + c_1\right)^{-1} \tag{48}$$

To find the integration constant c_1, one can use the assumption that the velocity at early times can be described by the HB velocity of Wilks and the electron density at $t \to -\infty$ is given by the initial density of the interaction, the critical density n_c. This results in the integration constant of $c_1 = \sqrt{2cn_cM/[(1+R)Z]}$, and the velocity can be described by:

$$v(t) = \sqrt{I(t)}\left(\int_{-\infty}^{t}\frac{1}{2n_e(x(t'))}\frac{dn_e(x(t'))}{dx}\sqrt{I(t')}dt' + \sqrt{\frac{2cn_cM_i}{(1+R)Z}}\right)^{-1}. \tag{49}$$

Equation 49 can be even more simplified when assuming an exponential density profile with the scale length $L_c = n_e(dn_e/dx)^{-1}$, which does not change over time:

$$v(t) = \sqrt{I(t)}\left(\frac{1}{2L_c}\int_{-\infty}^{t}\sqrt{I(t')}dt' + \sqrt{\frac{2cn_cM_i}{(1+R)Z}}\right)^{-1}. \tag{50}$$

In the limit of a long scale length L_c, this description again results in the well known HB velocity equation, with the constant critical density.

Calculating the temporal derivative of Eq. 50 results in a description of the corresponding HB acceleration:

$$a(t) = L_c \frac{\frac{I'(t)}{2\sqrt{I(t)}}\left(\int \sqrt{I(t')}dt' + 2L_c\sqrt{\frac{2cn_cM_i}{(1+R)Z}}\right) - I(t)}{\left(\int \sqrt{I(t')}dt' + 2L_c\sqrt{\frac{2cn_cM_i}{(1+R)Z}}\right)^2}. \quad (51)$$

Using the same parameter as for in the PIC simulation, e.g. a Gaussian pulse with a pulse duration $\Delta t = 250fs$, the same maximum laser intensity and scale lengths of the initial plasma, a calculation of the maximum HB acceleration is possible. An example for this process is found in A. 3. Figure 3.13 shows the results of these calculations for a reflectivity of R = 1, given by the colored dashed lines for the respective maximum laser intensity, which are in very good agreement with the simulation. Therefore, the scaling change of the maximum HB velocity and acceleration from $I^{1/2}$ to $I^{1/4}$ simply arises from the dynamic of the interaction with the density profile.

This shows that the scale length of the preplasma, that is present close to the peak intensity, can be deduced, just by measuring the acceleration of the critical density position into the plasma at the beginning of the LPI, in combination to the maximum laser intensity. As already mentioned, the scale length also influences the maximum reachable HB velocity, which can be retrieved from the measurement of the complete reflected spectrum, which was already shown by Zepf *et. al.* [17].

Therefore, a simpler way of achieving information about the scale length of the plasma is also given by the analysis of the time-integrated spectrum. The simulations show an increased maximum red shift and therefore HB velocity in the presence of a preplasma with a long scale length. Therefore, instead of analyzing the initial acceleration, a measurement of the maximum HB velocity can be done, which can then be correlated to the scale length of the preplasma.

In contrast to the blue shift of the spectrum, which can either be created by the initial preplasma expansion or the expansion of the plasma at the end of the interaction. The PIC simulations show that the red shift is created by the maximum HB velocity only, which results from the comparison with the movement of the critical density. The highest wavelength component within the spectrum of the reflected pulse then corresponds to the maximum HB velocity. The derived description of the HB velocity, given by Eq. 50, shows that the presence of a short-scale-length plasma reduces the HB velocity. Reducing the scale length results in a lower maximum HB velocity and therefore leads to a reduced red-shifted spectrum.

To verify this assumption, the spectra of the reflected pulses for different laser intensities and preplasma conditions are extracted from the simulations and analyzed in terms of central wavelengths, given by the first moment of the spectrum, and the maximum wavelength at 5 % of the maximum spectral intensity. The results are shown in Fig. 3.15a, with

the maximum wavelength of the incoming spectrum given by the dashed black line and the calculated maximum wavelength, using the velocity from Eq. 50, which is additionally shifted by the initial expansion velocity for the different scale length plasmas.

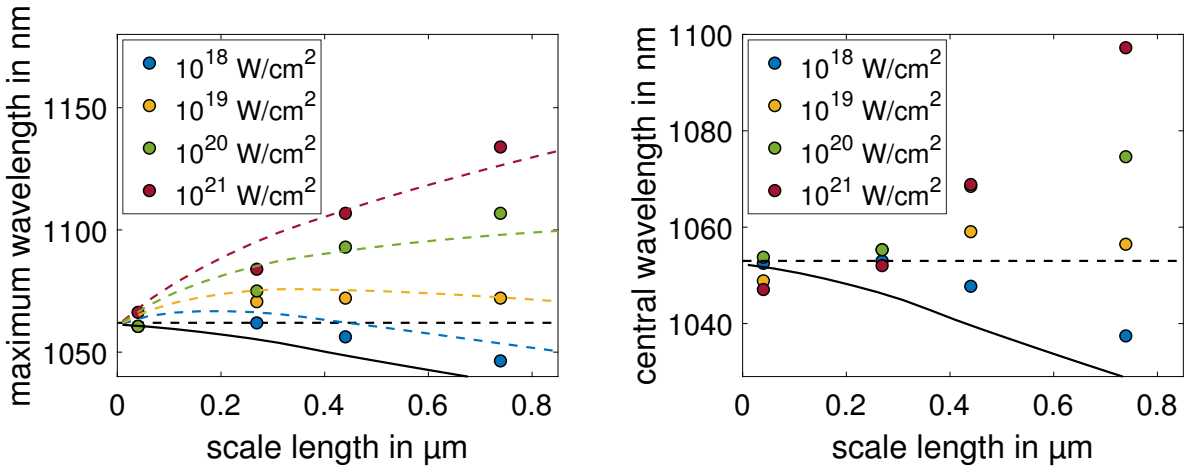

Figure 3.15: (a) The maximum red shift at 5 % of the spectral intensity for different laser intensities (colors) and different scale lengths are shown in, whereas the black dashed line corresponds to the highest spectral component of the incoming pulse. The dashed colored lines show the calculation of the maximum wavelength shift using Eq. 50, which is additionally corrected by the initial-expansion shift of the plasma. (b) The corresponding central wavelength of the reflected pulse for different laser intensities and scale lengths is shown in, whereas the black dashed line corresponds to the initial central wavelength of the pulse before the interaction. The solid black lines indicate the shift that would be introduced by the initial expansion of the preplasma.

It can be seen that the maximum wavelength increases for higher laser intensity. Above laser intensities of 10^{19} W/cm^2 the maximum wavelength additionally increases for higher scale lengths. In case of the lower intensities, the light pressure is not sufficient to compensate the initial expansion pressure of the preplasma which leads to a decreasing maximum wavelength and therefore a complete blue-shifted spectrum.
This case might not be reachable in experimental conditions since the presented long scale length is directly correlated to a high electron temperature, which should not be present if the laser intensity is low.
A similar behavior is seen by analyzing the central wavelength of the pulse after the interaction, which is shown in Fig. 3.15b. It is visible that the central wavelength reduces when a low scale length preplasma is present, which increases for rising laser intensity. One reason for this could be an increased heating of the target which increases the plasma pressure and therefore leads to a stronger blue-shifted spectrum, which depends on the

initial temperature of the plasma. At a threshold scale length, close to the simulations with $L_c \approx 0.27\,\mu m$, the spectrum either shifts towards higher wavelengths when the HB dominates for high laser intensities, or towards lower wavelengths if the laser intensity is too low. A comparison of the analytical description with the central wavelength is not possible, since the deduced model does not take any plasma pressure into account, which leads to a blue shift of the spectrum after reaching the peak laser intensity. It should also be possible to include the effect of the plasma pressure in the description of the HB velocity, which is part of future work.
The use of both quantities allows to determine the region of the scale length by just measuring the spectrum of the pulse after the interaction. This direct correlation might only be valid if the target is opaque during the interaction and relativistic transparency does not occur, which could be verified by a measurement of the transmitted light. The latter case would introduce a much stronger red-shifted spectrum, which might not permit a direct correlation to the initial scale length.
In combination with the measurement of the expansion velocity, most of the preplasma parameters are extracted, just by temporally resolving the reflected laser pulse during the LPI. Even when just measuring the time-integrated spectrum these information are partially obtainable. This qualifies the measurement of the reflected pulse after the interaction as a promising method to get insight into the present preplasma conditions close to the arrival of the peak laser intensity. So far, only the case of normal incidence has been studied, which will be expanded to higher incidence angles in the next section.

3.3.9 Influence of the incidence angle on the Doppler shift

An aspect which has to be examined is the dependency on the incidence angle for the LPI. As already mentioned, the shown simulations and corresponding analysis were performed with an incidence angle between laser axis and target-normal of 0°, leading to an expansion of the plasma on the laser axis. When increasing the interaction angle, the effective expansion velocity with respect to the propagation axis changes. This effect is already indicated by the cosine-term in Eq. 22.
Therefore additional simulations for an intensity of $10^{20}\,W/cm^2$ were performed with an increased incidence angle of 30°. The verification is done in the same way as in the previous section. First the correlation between the movement of the critical density and the instantaneous wavelength is cross-checked. The comparison to the density surface movement, normal to the target surface, for an initial electron temperature of 2 keV is shown in Fig. 3.16, showing a good agreement between the movement of the critical density and the instantaneous wavelength.
This indicates that the presented method of the temperature measurement is also valid

for non-zero incidence angles. However, it should be noted that the time-resolved correlation is only given for an s-polarized laser pulse and might not be applied to a p-polarized laser field at large angles [20]. The projection of the expansion velocity on the laser axis due to the interaction angle has to be taken into account when calculating the temperature of the preplasma. Besides the impact on the temperature measurement, the effect of increasing interaction angles on the measurement of the scale length must be investigated. Therefore, the central wavelength and maximum red shift after the interaction has been extracted from the spectrum and compared to a simulation with an incidence angle of 0° and the same laser intensity of 10^{20} W/cm^2. The results of the maximum wavelength and central wavelength is shown in Fig. 3.17.

The behavior of the maximum wavelength seems to be similar for both incidence angles. When comparing the central wavelength of both cases, a slight discrepancy, especially in the lower scale length regime, is visible. This deviation might correspond to a varying reflection angle during the interaction in case of an oblique incidence, which would change the angular-spectral behavior of the reflected beam. This might change the central wavelength of the laser pulse after the interaction, depending on the analyzed angle.

However, since both interaction angles show a similar impact on the spectral properties of the reflected pulse, the mentioned method is still viable to estimate the scale length of the preplasma. The maximum acceleration at the beginning of the interaction can be calculated, analogously to Sec. 3.3.8. To enable a direct comparison to the analytical description (Eq. 51), the interaction angle θ has to be taken into account, which is done by

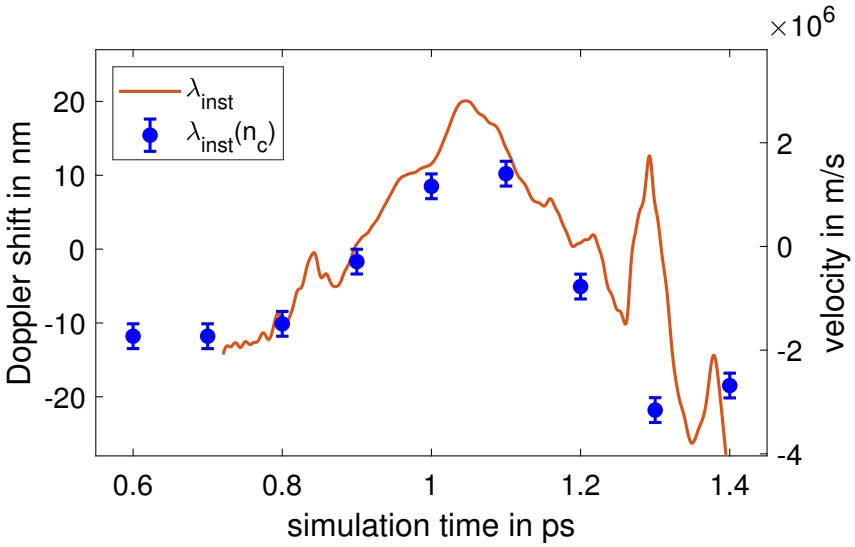

Figure 3.16: This figure shows a comparison of the Doppler shift introduced by the velocity of the critical density during the simulation (blue dots) and the instantaneous wavelength of the laser pulse which is reflected during the interaction (red) for an incidence angle of 30°.

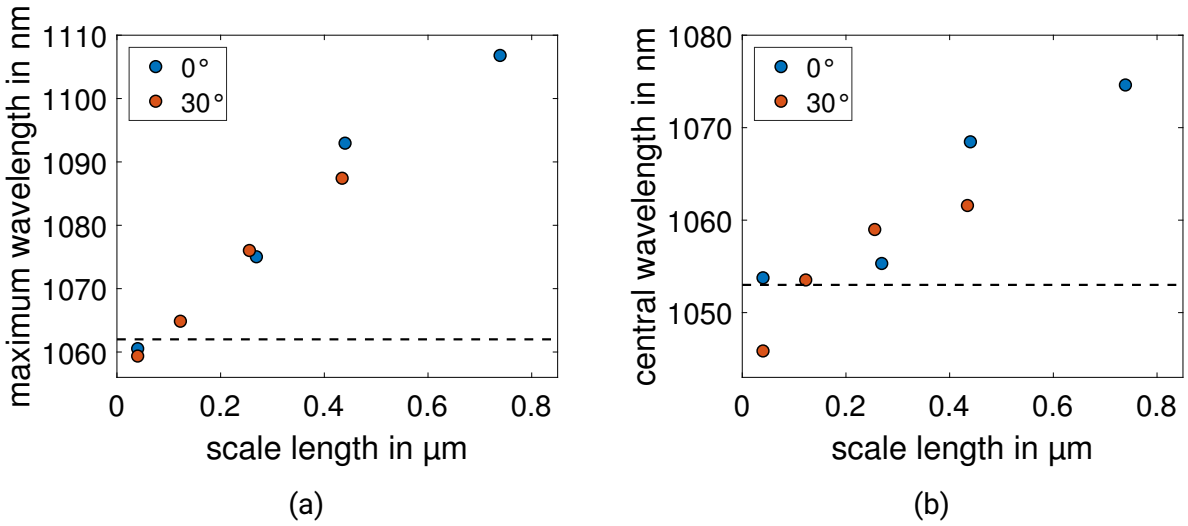

Figure 3.17: (a) The maximum red shift at 5 % of the spectral intensity for an incidence angle of $\Theta = 0^\circ$ (red) and $\Theta = 30^\circ$ (blue) for different scale lengths are shown, whereas the black dashed line corresponds to the highest spectral component of the incoming pulse. (b) The corresponding central wavelength of the reflected pulse for different incidence angles and scale lengths is shown, whereas the black dashed line corresponds to the initial central wavelength of the pulse before the interaction. Despite the different interaction angle, the spectral behavior is similar for both cases.

reducing the momentum of the light pressure, given by Eq. 46, by $\cos(\theta)$. This changes the integration constant in Eq. 48 to $c_1 = \sqrt{c n_c M_i/[(1+R)Z\cos(\theta)]}$. In addition, the laser pulse interacts with a longer scale length, because of the one-dimensional expansion of the plasma, which has also been taken into account. Figure 3.18 shows the results of the simulations for an incidence angle of $\theta = 30°$, different scale lengths, with respect to the direction in target normal, and laser intensities, including the adapted analytical description which is given by the dashed lines.
This shows that the model and the method to extract the preplasma properties from the laser pulse after the interaction can also be adapted for an oblique incidence angle.
However, there are still some limitations of this method and possible influences which have not been considered so far, which will be discussed in the following section.

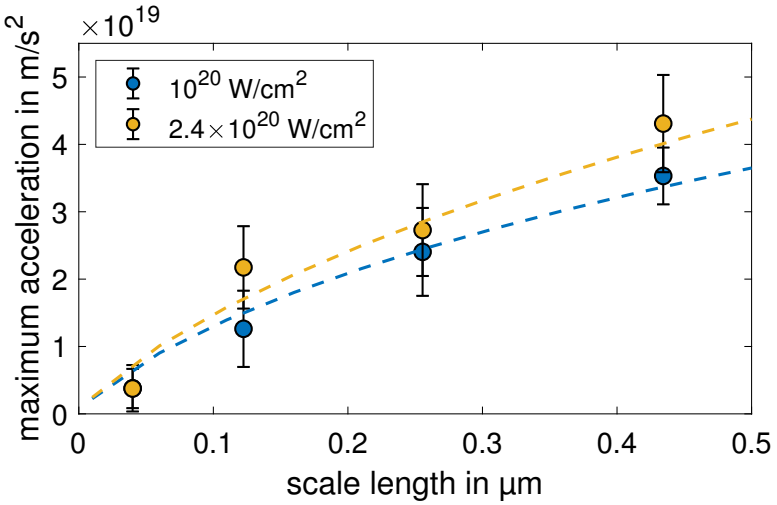

Figure 3.18: This figure shows the maximum HB acceleration for different plasma scale lengths and different laser intensities for an incidence angle of 30°. The dashed colored lines show the calculated acceleration for the different scale lengths and laser intensities, while taking the increased incidence angle into account.

3.3.10 Discussion

The described way of determining the preplasma properties relies on several assumptions and is restricted to certain laser and plasma parameters. Therefore, the laser and plasma parameter outside of the so far investigated range might disturb the extraction of the preplasma information from the spectrum and phase of the laser pulse, which will be discussed in the following section.

Effect of self-phase modulation

One of the key requirements for the presented method is the correlation of the Doppler shift to the movement of the critical density while neglecting the frequency changes introduced by SPM. As indicated by Eq. 36 the impact on the phase increases in case of high laser intensities or a very short pulse duration which both increase the magnitude of the temporal intensity derivative and therefore increases the impact of SPM [90]. This effect has even more impact if the laser pulse propagates through a long near-critical preplasma, which is present in case of a very long scale length. This implies a possible upper limit for the measurable preplasma scale length if the effect of SPM starts to dominate the spectral behavior. Additional studies have to be done when including ionization, which temporally changes the electron density and therefore leads to further self-phase modulation [95]. It is also problematic that the presence of a strong SPM might not be directly visible within the spectrum or the time-resolved measurement, which makes it difficult to determine such a limit.

Effect of the dynamic range

As already mentioned in the previous section, it is necessary to resolve the region where the critical density movement is dominated by the plasma pressure. In experimental conditions, this is given by the dynamic range of the measurement. Within the simulation, this is given by the definition of the laser pulse, since the EM field starts and ends with a rapid rise and drop from 0 to a certain defined intensity-ratio and vise versa. The effect of different intensity-ratios of such a cutoff can be seen in Fig. 3.19, showing the instantaneous wavelength of a laser pulse with the intensity of 10^{20} W/cm^2 after the interaction with a plasma of $T_{e,ini}$ = 2 keV at normal incidence. The instantaneous wavelength at the beginning of the pulse is shown for an intensity cutoff at 10^{-2} (blue) and 10^{-5} (red) of the maximum intensity. In the case of a lower dynamic range the plateau from the initial Doppler shift, introduced by the expansion of the preplasma, can not be measured with a contrast of 10^{-2}. The reduction of the intensity-ratio could lead to a wrong estimation of the initial Doppler shift and therefore an error-prone calculation of the preplasma temperature. Especially in experimental conditions, where the level of noise is much higher than during the simulation, this restriction might limit the possibility of the temperature and scale length measurement.

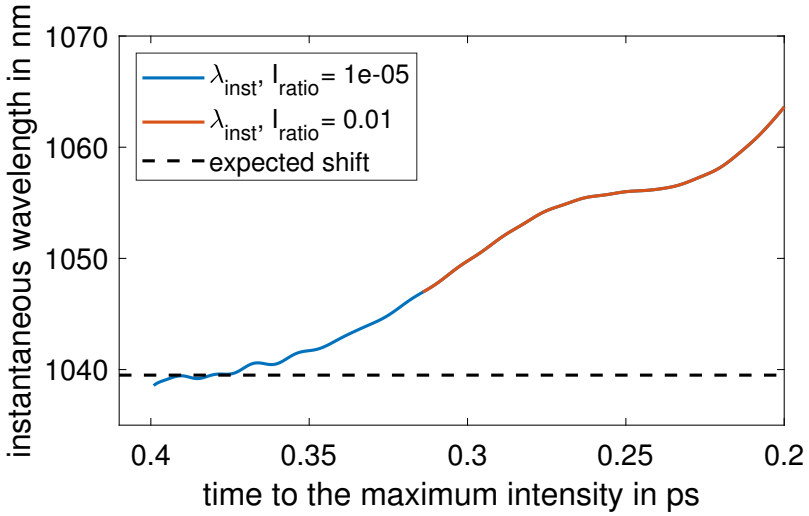

Figure 3.19: Influence of the laser-cutoff intensity on the determination of the initial spectral shift.

Effect of the ionization state

A further assumption that is used for the simulation, which is also needed for the temperature measurement is the ionization state of the ions within the preplasma. According to Eq. 44 the charge state affects the correlation between the expansion velocity and

the temperature of the preplasma. For a given temperature and a reduced charge state from Z = 6 to Z = 3, the velocity decreases, resulting in a reduced blue shift.
If the charge state is unknown, which is usually the case for a preplasma at such timescales, it must either be estimated or determined by hydrodynamic simulations. A wrong estimation would lead to a large uncertainty within the measurement of the preplasma temperature, due to the scaling between temperature and charge-state of $T_e \propto 1/Z$.

Effect of the laser-pulse duration

One aspect which still needs to be studied is the dependency on the pulse duration, especially for short laser pulses in the range of tens of femtoseconds. Small spectral shifts that are introduced by the initial plasma expansion might not be visible in case of these broadband pulses. Therefore, a short laser pulse duration might be a limit to the field of application for this method. In addition to this, the interaction dynamics strongly changes in this regime, leading to a much shorter HB duration and therefore a stronger acceleration. Analytically calculating the maximum HB acceleration for different pulse durations using Eq. 51 leads to an empirical scaling of $\approx \Delta t^{3/2}$. This can be cross-checked by performing a simulation with a laser intensity of $2.4 \times 10^{20}\,\mathrm{W/cm^2}$, a scale length of L_c = 0.48 µm, and a reduced pulse duration of Δt = 125 fs, which is a factor of 2 lower than the other simulations. This results in an acceleration of $(1.74 \pm 0.25) \times 10^{20}\,\mathrm{m/s^2}$, which is in rather good agreement with the results obtained for a pulse duration of Δt = 250 fs, multiplied by $2^{3/2}$, which results in $(1.42 \pm 0.21) \times 10^{20}\,\mathrm{m/s^2}$.

3.4 Conclusion

The previous sections have shown that the laser pulse, reflected during the interaction with a plasma, contains plenty of information about the preplasma and the interaction dynamics. This study has been carried out by performing 2-D PIC simulations for various laser and plasma parameters. With the help of a time-resolved analysis of the Doppler shift, the movement of the critical density can be tracked throughout the interaction.
The temporally resolved analysis of the laser pulse shows a clear correlation between spectral laser-pulse properties and the preplasma parameters, despite some dependencies that have to be investigated, like the dependency of the HB acceleration and maximum velocity on the dimensionality of the interaction.
At early interaction times, where the light pressure is smaller or comparable to the pressure of the expanding plasma, the pulse contains information about the preplasma state picoseconds prior to the arrival of the peak intensity. The initial blue shift of the pulse

spectrum can be correlated to the expansion velocity and to the corresponding electron temperature, assuming that the preplasma expansion is one-dimensional and follows the Samir model [83]. In addition to the temperature, information about the scale length of the preplasma can be extracted from this region, when the light pressure slowly overcomes the plasma pressure. The initial acceleration of the critical density position increases in case of higher laser intensities as well as in the presence of longer scale length plasmas. An analytical description of the HB velocity, which included the assumption of a density change during HB, and the corresponding acceleration was derived which enabled the possibility to calculate the maximum HB acceleration between 400 fs and 200 fs prior to the initial peak intensity. The resulting dependence of the acceleration on the laser intensity as well as the scale length is in very good agreement with the 2-D PIC simulation results. This shows that measuring the temporally resolved spectral shift, which is created at early interaction times, can be used to get insight into the preplasma properties. With this analytical model, the preplasma properties might be directly deduced from the measurement of the time-resolved spectrum. Therefore, the simulations indicate that this non-invasive single-shot method, which does not require any secondary probe beam, might be able to measure scale length regimes currently not reachable by other types of diagnostics.

Even when only the time-integrated spectrum after the interaction is measured, the scale length can be estimated by the maximum occurring wavelength, which could also be derived from the presented equation for the HB velocity, in combination to the corresponding central wavelength. An increased maximum red shift in combination with a red-shifted central wavelength indicates a higher scale length of the preplasma. On the contrary, a blue-shifted central wavelength in combination to a low maximum red shift shows the presence of a plasma with a strong density gradient.

While this study establishes the presented method as a diagnostic for preplasma properties, these findings have to be experimentally verified. The realization of such an experiment will be presented in the next section.

4 Experimental Validation

In the previous section several findings, which imply a direct correlation between plasma parameters and the spectral evolution of the reflected laser pulse, have been deduced from numerical simulation of the LPI and the developed analytical model. This includes the study of the initial blue shift of the instantaneous wavelength and the acceleration of the critical density into the plasma, at the beginning of the interaction. The corresponding spectral properties of the complete reflected laser pulse are correlated to the different preplasma conditions.
To observe these correlations during experimental conditions and therefore validate the measurement principle, I conducted two experiments at the PHELIX facility [22]. This facility provides laser intensities up to $5 \times 10^{20}\,\mathrm{W/cm^2}$, while using a F/1.7 focusing parabola, with maximum pulse energies of 180 J on target and a pulse duration of (500 ± 75) fs [96]. Additionally, the system ensures a high temporal ASE contrast of 10^{-12} on the nanosecond-to-100-picosecond time scale [78], which is necessary to reduce the pre-expansion of the target as much as possible. Therefore, PHELIX offers optimal conditions to perform such a study, which will be presented in this section.
In the following, Sec. 4.1 describes the setup of the experimental campaigns, including the difference of the temporal contrast for both experiments, which influences the state of the preplasma. In particular, the diagnostics that play a central role deserve to be put in focus in Sec. 4.2. Then, Sec. 4.3 and Sec. 4.4 proceed with the analysis of the time-integrated and time-resolved data, which is the basis for the subsequent discussion. At last, Sec. 4.5 deals with the comparison of the experimental and numerical results.

4.1 Experimental setup

I gathered the data that is analyzed in this thesis during two experimental campaigns in December 2018 and June 2020, during which I acted as experiment coordinator (EC). My main tasks and contribution to the experiment were the technical planning and implementation of the proposed setup after consultation with my supervisor, as well as the team coordination before and during the experiment. During the technical planning, I was responsible for the design and procurement of the plasma-mirror and target mount, as well as the diagnostics. During the execution of the experiment, I was additionally involved in carrying out the shot procedure and the data acquisition.
The validation of the measurement principle for the preplasma properties, which has been described in Sec. 3, is the main goal of these experiments. The simplified scheme of the setup, shown in Fig. 4.1, is kept similar for both beamtimes. The laser pulse enters the target chamber and is focused onto a, by 30° rotated, thin foil target using a F/1.7 off-axis

parabola. The foil is placed on a Plexiglas frame, which is mounted on a specifically-designed Delrin holder to reduce the electromagnetic pulse (EMP) that is created during the LPI. This would otherwise disturb the online measurement of the reflected pulse. To capture the beam after being reflected by the target, a sub-aperture of it is coupled out using an uncoated mirror. This sub-aperture covers only an opening angle of 3° in specular direction to reduce further nonlinear effects in following optical components. To ensure a measurement of the pulse in the focal region and increase the stability from shot to shot, the beam is relay-imaged onto the diagnostics outside the chamber.

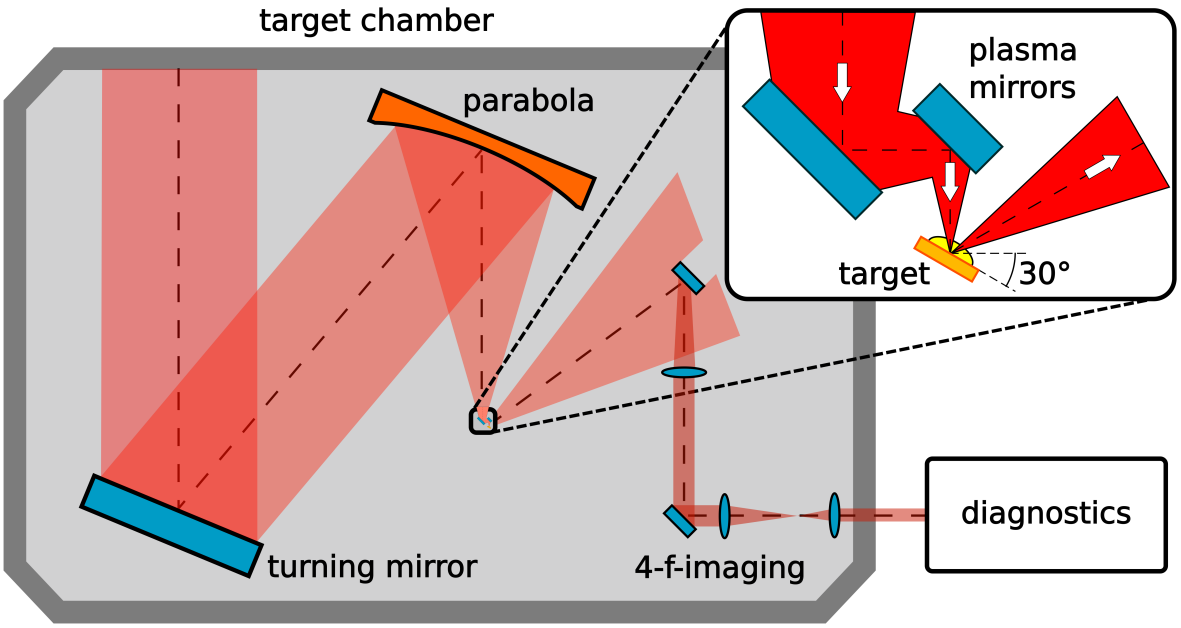

Figure 4.1: Simplified scheme of the experimental campaigns. The beam is focused onto the target using a F/1.7 off-axis parabola. A part of the reflected beam is imaged onto the diagnostics, which are placed outside of the chamber. To enhance the temporal contrast, a plasma mirror (PM) can be implemented, which is indicated by the inlet.

The imaging onto the diagnostics is crucial for the stability of the measurement. During the initial alignment of the beam path a mirror has to be put into the exact focus position of the laser beam. A vertical or horizontal tilt, with respect to the intended target surface orientation, will change the direction of the reflected beam and therefore changes the sub-aperture that is measured by the diagnostics. While the reflection angle only affects the direction that is measured, an offset in the position of the mirror leads to a pointing error during the shot and a misalignment of the diagnostic path. This is much more detrimental to the measurement method than the rotation. Since most optical diagnostics are very alignment-sensitive, a changed path of the reflected beam would lead to an altered or wrong measurement, underlining the importance of a precise imaging of the reflected beam.

To verify the model presented in Sec. 3.3, the conditions of the preplasma have to be varied to enable different scale lengths and temperatures. To achieve these conditions, including an unperturbed and cold plasma when the peak intensity arrives at the target, the contrast of the laser pulse is manipulated. This is done by placing two plasma mirror (PM) into the focusing beam, which is indicated by the inlet in Fig. 4.1. This increases the temporal contrast on the nanosecond scale up to 2-3 orders of magnitude and steepens the rising slope of the laser pulse close to the peak intensity [97]. Depending on the angle of incidence and the polarization of the laser pulse, a single PM is able to reflect up to 80 % of the incident energy [98]. During the experimental campaigns, both a single and double PM setup have been used to increase the temporal contrast.
To better understand the effect of the PMs on the laser beam, a simplified scheme of the setups is shown in Fig. 4.2, whereas the focused laser pulse is shown in red, the PMs in blue and the target in yellow. The laser is either directly focused on the target to study the interaction without any contrast improvement (a), reflected by one PM which changes the direction of the beam by 90° (b), or is reflected by two PMs (c). The last configuration does not change the direction of the beam, but introduces a spatial offset to the focal position. Therefore, switching from configuration (a) to (c) is possible within a short time frame of a few hours, whereas the setup (b) would require a new setup of the reflection beamline and was therefore conducted in a separate campaign.

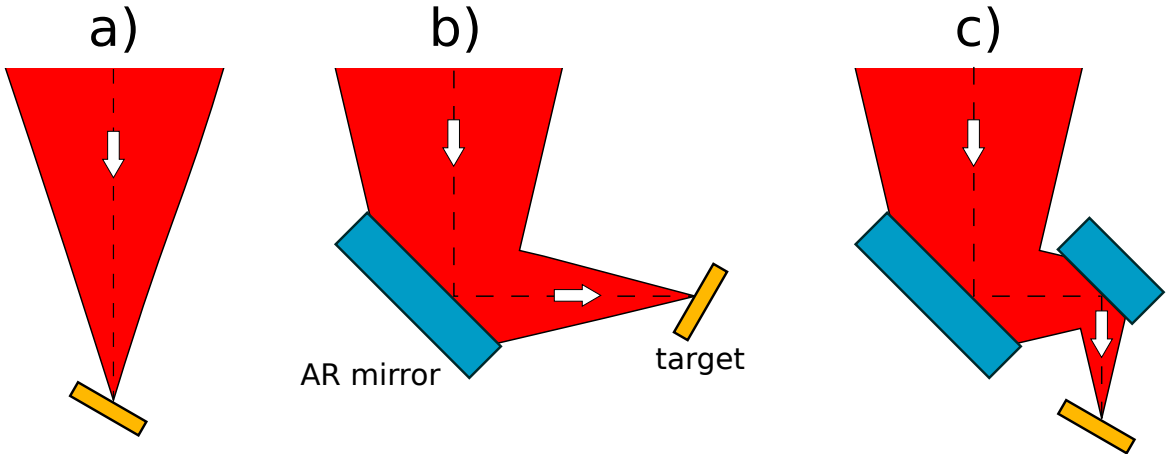

Figure 4.2: A simplified scheme of the setups used during the experimental campaigns. The laser is either directly focused onto the target (a), reflected by a single PM (b), or reflected by a double PM (c).

Both PM configurations were characterized during the experiments by measuring the reflectivity for different incident pulse energies, while keeping the pulse duration constant. The reflectivity of the single and double PM setup was measured to be ≈ 68 % and ≈ 55 %, for the maximum possible laser energy of 120 J and 160 J respectively. A more detailed description about the characterization and properties of the used PM, including the re-

flectivity curve for different angles of incidence, can be found in Sec. A. 4. Setup (c) used standard commercial coatings, whereas the coating for setup (b) was optimized for a large range of incidence angles, which are present in the converging beam of the focusing parabola. The resulting theoretical contrast, which is calculated with the response curve of each setup and the respective measured temporal contrast, is shown in Fig. 4.3. For a better differentiation, the earlier campaign which uses the double PM is referred to as experiment A and the latter with only one PM is referred to as experiment B.

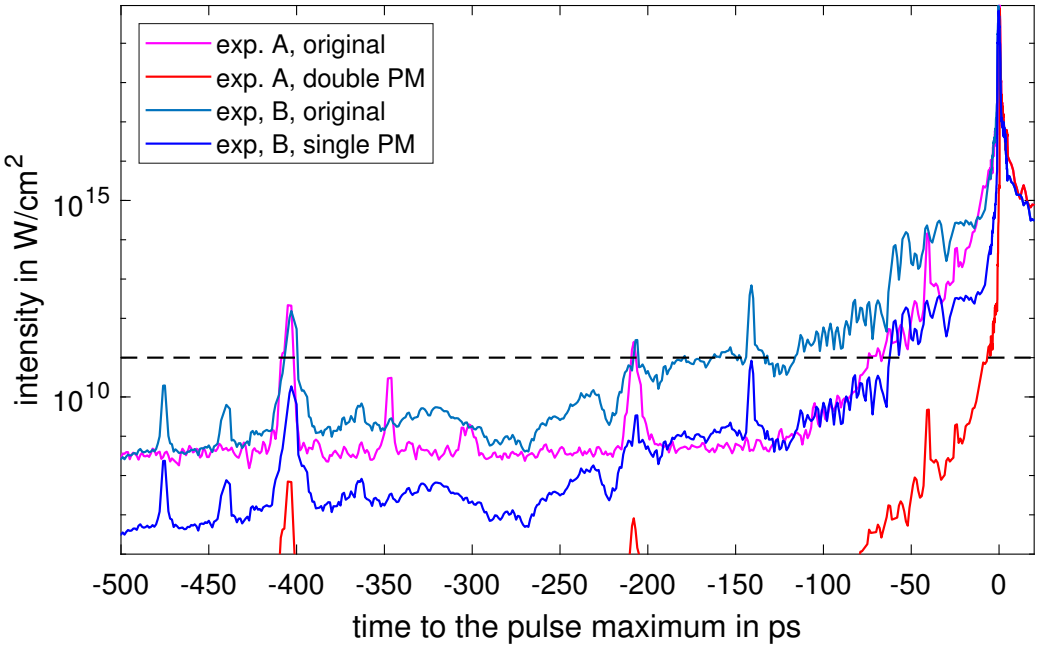

Figure 4.3: The different initial temporal contrast for the two experimental campaigns are indicated by the magenta line for experiment A and the light blue line for experiment B. The corresponding theoretical contrast curves for the double and single PM setups are given by the red and blue lines, respectively. The approximate ionization threshold is indicated by the dashed black line.

The initial temporal contrast of both campaigns are indicated by the magenta line for experiment A and the light blue line for experiment B. The red and blue lines correspond to the theoretical contrast curves for the double and single PM setup respectively. The single PM reduces the prepulses $\approx$ 140 ps and $\approx$ 400 ps prior to the maximum intensity and the laser pulse reaches the ionization threshold (black dashed line) $\approx$ 60 ps prior to the peak intensity. For the double PM, the time difference between ionization and peak intensity is even further reduced, below 5 ps.
One sees that the main difference between the experiments is given by the temporal contrast as well as the maximum possible energy on target, which is reduced by the different PM setups. These differences between both campaigns will be briefly described.

During experiment A, the double PM improved the temporal contrast on the nanosecond scale by approximately four orders of magnitude while reducing the energy on target from $\approx$150 J to $\approx$80 J. This leads to the reduction of the intensity on target from $\approx$ 2.4×10^{20} W/cm^2 to $\approx 1 \times 10^{20}$ W/cm^2. During this experimental campaign, the target material is given by polystyrene with a varying thickness between 35 nm and 1 µm, which were manufactured at the TU-Darmstadt.
The corresponding reflected pulse is measured for different laser energies and target thicknesses. To further characterize the interaction, the setup included a measurement of the transmitted light in terms of energy, spectrum and temporal pulse profile. The latter properties are measured, similar to the reflected pulse, by imaging the interaction region onto a device based on "Frequency-Resolved Optical Gating" (FROG) and a spectrometer. These diagnostics are described in Sec. 4.2. In addition to this, we placed a glass screen, with a cut-out for the time-resolved measurement, in the transmitted beam and collected the scattered light with a Fresnel lens to measure the transmitted energy with a calorimeter.
As already mentioned, a complete removal of the PM to obtain a reduced temporal contrast was not possible during experiment B, due to the additional deflection introduced by the single PM. Therefore, a high reflectivity mirror replaced the anti-reflection coated mirror to achieve a low temporal contrast for comparison. This lead to a reduction of the energy on target for both cases from $\approx$120 J to $\approx$80 J. During this experiment, the target thickness was kept above 500 nm to ensure fully opaque targets during the interaction.
For a better overview, the resulting laser parameters of the different beamtimes are summarized in Tab. 3, including the energy on target E_L and the corresponding intensity I_L, for the mentioned setups, as well as the contrast improvement within each experiment.

exp.	E_L and I_L without PM	E_L and I_L with PM	contrast enhancement
A	150 J, 2.4×10^{20} W/cm^2	80 J, 1×10^{20} W/cm^2	$\approx 2.5 \times 10^{-4}$
B	80 J, 1×10^{20} W/cm^2	80 J, 1×10^{20} W/cm^2	$\approx 4 \times 10^{-3}$

Table 3: Laser energy for the different contrast setups of both experiments, including the contrast enhancement on the nanosecond scale, introduced by the PM.

The resulting spectral and temporal properties of the laser pulse that is reflected during these experiments have to be measured. Therefore, the necessary optical diagnostics and corresponding requirements are described in the next section.

4.2 Optical diagnostics

In order for a time-resolved diagnostic to be used for the measurement of preplasma properties, it must meet several requirements. It has to be able to perform for various properties of the laser pulses to be measured, from a narrow bandwidth and short pulse duration during alignment, to spectrally- and temporally-broadened pulses during the measurement, both with a sufficient resolution. This includes a spectral bandwidth of 4 nm and a pulse duration of 500 fs when measuring the initial properties of the incoming laser pulse and up to 200 nm with a temporal measurement range of a few picoseconds after the interaction with a plasma. In addition, the diagnostics must provide a stable alignment with adjustable energy range to ensure a single-shot operation.
The time-resolved measurement of the incident laser pulse, as well as the reflection measurement during the interaction is performed with a diagnostic based on "Frequency-Resolved Optical Gating" (FROG) [99], which uses the second-harmonic generation (SHG) to acquire a time information. This diagnostic, which has been specifically designed during a master thesis by C. Schmidt and later on improved and commissioned during my master thesis, is able to cover the necessary temporal and spectral measurement range [23, 100]. In addition to this, the algorithm used for the reconstruction of the measured FROG traces has been implemented into a LabVIEW [101] program to enable a real-time analysis of the measurement. Such a diagnostic based on FROG has been used by other groups to detect the relativistic transparency [21], or at laser intensities in the range of 10^{18} W/cm^2 [19], with only minor success.
The described diagnostic can be used to characterize the laser pulse that is incident on the plasma. This is especially important when utilizing a PM, which introduces a blue shift at the beginning of the laser pulse [97]. This would mainly impact the time-resolved diagnostics, resulting in an incorrect measurement of the preplasma properties. The measurement of the incoming laser pulse was performed during experiment A without a target in the focal region and by utilizing the previously mentioned beamline to measure the transmitted pulse. These measurements of the pulse with and without PM showed an offset of the initial wavelength when the pulse intensity reached 0.1 % of its maximum. Figure 4.4 shows the measurement of the input pulse and the corresponding instantaneous wavelength with (a) and without (b) the PM.
Since the time-resolved diagnostic has a time ambiguity, the wavelength shift was measured at both ends of the pulse. This leads to a possible offset of the initial wavelength of $\Delta\lambda_{high} = ^{-0.3}_{-1.5}$ nm and $\Delta\lambda_{low} = ^{+2.8}_{+0.4}$ nm for the high and low contrast, respectively. Since the instantaneous wavelength before and after the interaction can not be directly correlated, the resulting uncertainty can not be included in the uncertainty of the reflection measurement. The impact of this uncertainty on the time-integrated spectrum should be

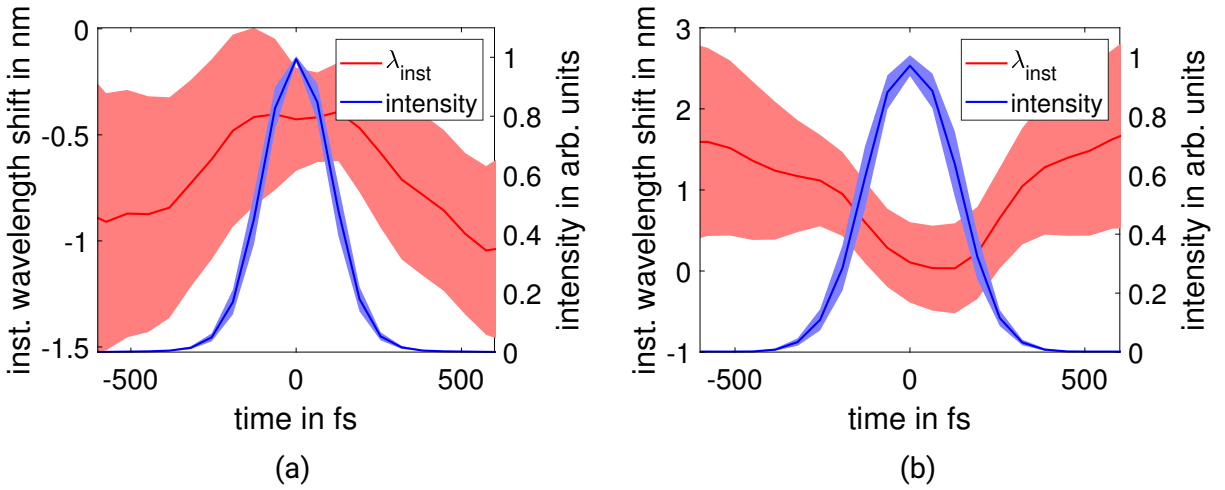

Figure 4.4: Time-resolved measurement of the incoming laser pulse in experiment A with (a) and without (b) PM. The red line shows the instantaneous wavelength shift with the corresponding uncertainty given by the shaded region. The blue line and region correspond to the intensity of the laser pulse and the uncertainty. An existing instantaneous wavelength shift is visible in both measurement which lead to an uncertainty of the reflection measurement.

comparably low since these wavelengths only contribute a small amount to the complete spectrum.

As mentioned, a drawback of this device is the time-ambiguity introduced by the second order nonlinear process. For this reason, another complementary diagnostic was developed in the framework of a master thesis which I supervised [102]. This device works with the principle of "Spectral Phase Interferometry for Direct Electric-field Reconstruction" (SPIDER) [103], which does not hold this type of ambiguity. The diagnostic was tested during the experiment B, showing a qualitative good agreement with FROG. However, a design flaw of the SPIDER implementation made it extremely alignment sensitive, but changes to the optical layout of the SPIDER are possible to alleviate this drawback. The results of the SPIDER diagnostic are therefore not part of this thesis and will be analyzed in future work.

Another time-resolved diagnostic that is used during experiment B is a Wizzler (Fastlite) to measure the laser pulse during alignment mode that is incident on the focal position without any target. This measurement is used to optimize the incoming laser pulse with a feedback to a Dazzler (Fastlite), which is placed at the beginning of the laser chain of PHELIX. This is done to flatten the initial phase of the laser pulse as much as possible. However, it is currently not possible to perform this optimization for the laser pulse on-shot with full energy.

As a complementary diagnostic, the time-integrated spectrum was measured by using a

commercially available spectrometer from OceanOptics (Maya 2000-Pro, MAYP113999) with a wide spectral range from 800 nm to 1200 nm, with a wavelength spacing of $\Delta\lambda$ = 0.2 nm. This spectrum can be used for a validation of the time-resolved diagnostics and as a stand-alone method to get information about the preplasma conditions. The analysis of these time-integrated measurements is first presented in the next section.

4.3 Time-integrated spectral analysis

The results of the time integrated spectra are now analyzed and compared for both experiments. An example for the measured spectra after the interaction with a plasma, with similar laser and target parameters of the different experimental campaigns, are shown in Fig. 4.5

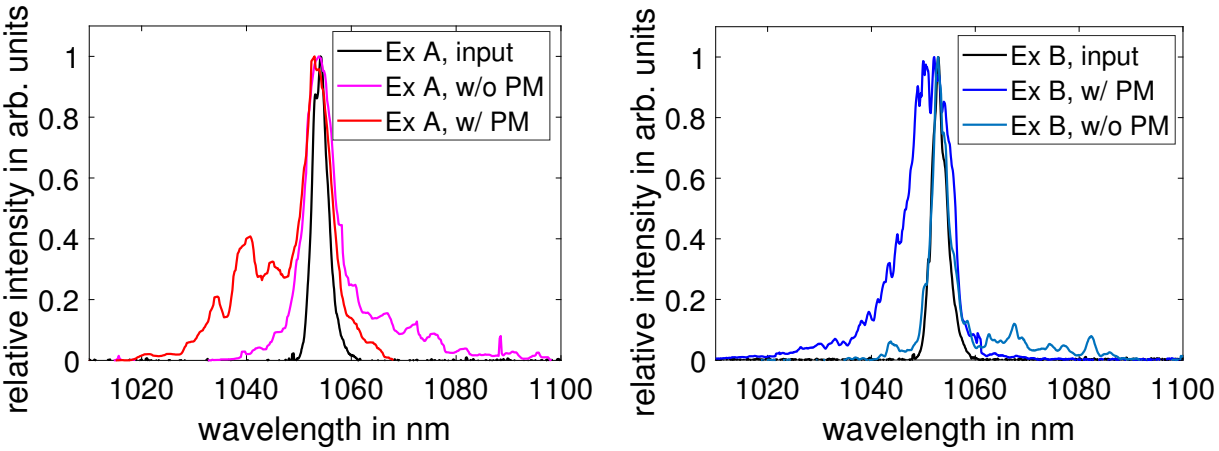

Figure 4.5: (a) Comparison of the normalized spectrum after the interaction with a plasma obtained during experiment A, with and without PM. A strong blue-shifted spectrum is obtained when a PM is used, compared to the red shift without PM. (b) A similar behavior is present in experiment B for the cases with and without PM.

The red and magenta curves represent the spectra of experiment A with and without double PM. The blue and light blue lines correspond to the spectra of experiment B, again with and without PM. This color code will be maintained for the upcoming figures in this section. One sees that the spectra without PM look similar for both beamtimes, including a strong red-shifted tail in both cases and the spectra with PM show a strong blue shift in both experiments. Most of the spectra show a dominant peak at the initial central wavelength. Our current hypothesis is that this might be introduced by scattered light from focal regions with a lower intensity, that either interacts with the plasma, or is just reflected at the surface of the target material. However, we were not able to verify this

and one should examine this feature, because its origin remains unclear. The presence of this peak leads to an offset of the central wavelength towards the initial wavelength of 1053 nm. For this reason, I removed the incoming spectral feature, by fitting a Gaussian distribution with a fixed bandwidth and central position, to ease the analysis of the data. The resulting central wavelength with and without this wavelength peak removal are used as a minimum and maximum value of the measured central wavelength, which is therefore included in the uncertainty of each measurement. Since this method does not change the maximum red-shifted part of the spectrum, this removal mainly influences the measurement of the central wavelength.
The resulting maximum wavelength of the spectrum and the shift of the central wavelength of every experiment is compared for the different contrast conditions. Because of the variation in the maximum available laser energy during both experiments, the spectral properties of the reflected pulses are compared for different laser energies. To illustrate this point, Fig. 4.6 shows the resulting central wavelength and maximum wavelength for different laser energies.

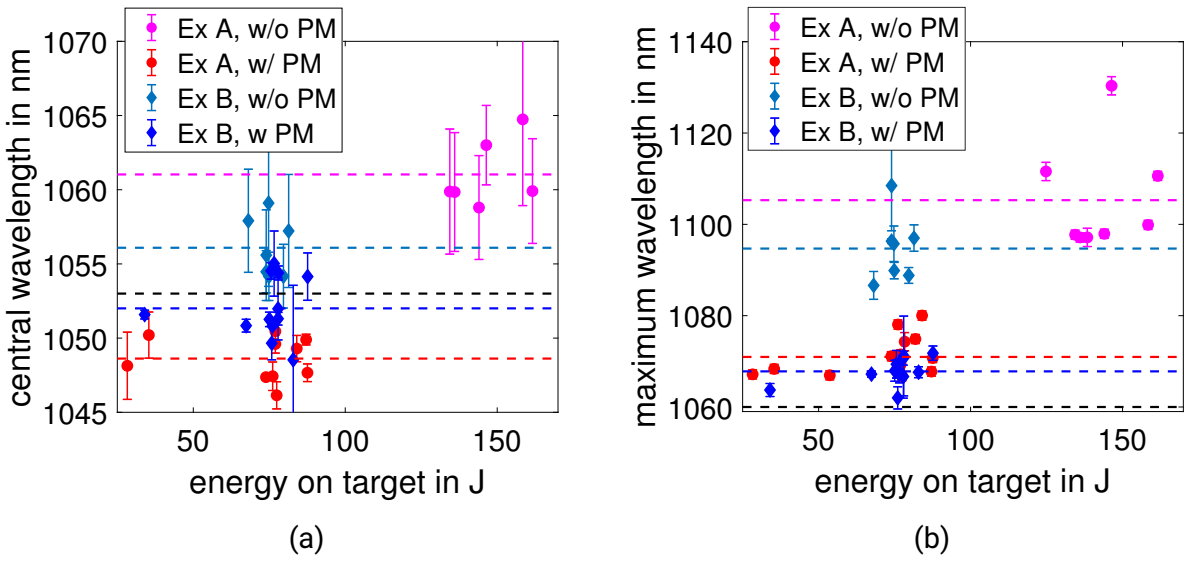

Figure 4.6: Comparison of measured spectral properties of experiments A and B for different on-target laser energies. The red and dark-blue dots correspond to the cases with a higher temporal contrast and the magenta and light blue dots show the measurement with a lower temporal contrast for the different experiments A and B. The lines in the corresponding colors represent the averaged value over all measurements. The central wavelength of the spectrum, given by its first moment, is shown by (a), whereas (b) shows the maximum wavelength at 1 % of the maximum spectral intensity. The dashed black lines indicate the central wavelength or maximum wavelength of the incoming laser pulse prior to the interaction.

Several tendencies can be seen when looking at the shift of the central wavelength in

Fig. 4.6a. First, the central wavelength is more blue shifted with respect to the initial central wavelength when a PM is used and red shifted in the case without PM, even when the energy on target is similar for both cases. It can also be seen that a stronger blue shift occurs when the double PM is used during beamtime A compared to the single PM of beamtime B. This is in agreement with the reduced expected temporal contrast when only one PM is used.
The strength of the blue shift with PM does not seem to depend on the energy on target. This is also in agreement with the simulation, which only shows an intensity dependence of the central wavelength if the scale length is above a certain threshold (Fig. 3.15). Only when the scale length is increased by removing the PM, the influence of HB starts to dominate the interaction and the central wavelengths tend to be more red-shifted when the energy of the laser pulse is increased.
A similar behavior is seen for the maximum wavelength of the spectrum as shown in Fig. 4.6b. In the presence of a high temporal contrast, the maximum wavelength does not seem to be changed within the chosen energy range. Only when removing the PM, the maximum wavelength strongly increases and an energy dependency is visible.
To determine whether the target thickness does have an impact on the spectral measurements, several target thicknesses have been tested during the experimental campaign. In addition, the transmitted laser energy for different target thicknesses is measured during experiment A, which is shown in Fig. 4.7.

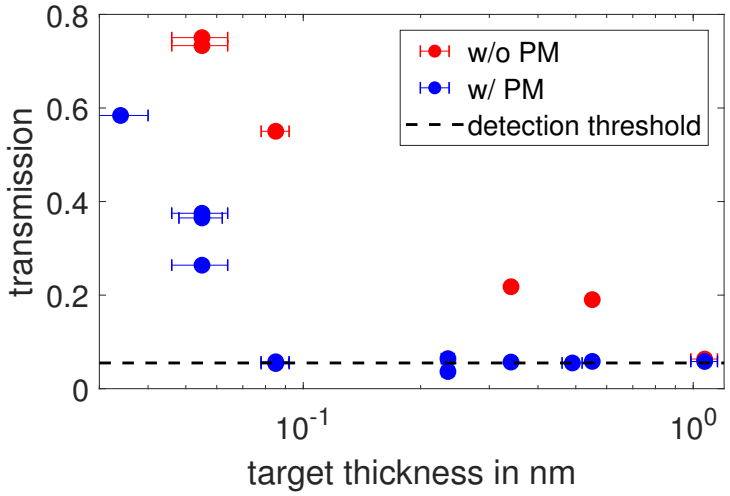

Figure 4.7: Measurement of the transmitted laser energy for different target thicknesses, with (blue) and without (red) PM, which has been performed during experiment A. The dashed black line indicates the detection threshold of the measurement setup.

Without a PM a significant amount of energy is transmitted for target thicknesses below 1 µm, ranging from 20 % for a target thickness of 550 nm up to 75 % for a 55 nm-thin target.

When using a PM, the transmission occurs only at target thicknesses below 85 nm. One would expect an increased red-shifted spectrum when reducing the target thickness, due to the possible onset of relativistic transparency.
The result of the spectral properties for the different target-thicknesses, with respect to the maximum wavelength and a shift of the central wavelength, is visible in Fig. 4.8.

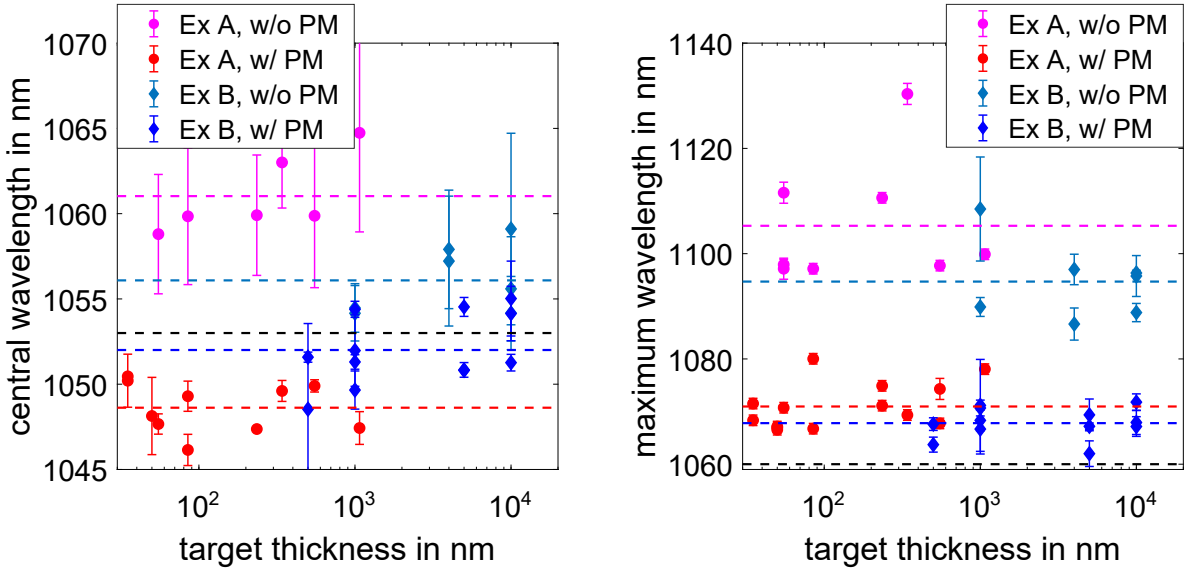

Figure 4.8: Comparison of measured spectra of experiments A and B for different target thicknesses. The red and blue dots correspond to the cases with a higher temporal contrast and the magenta and light blue dots correspond a lower temporal contrast for the different experiments A and B. The lines in the corresponding colors represent the averaged value over all measurements The central wavelength of the spectrum, given by its first moment is shown by (a), whereas (b) shows the maximum wavelength at 1 % of the spectral intensity for the different properties.

Even though the beamtimes do not share the complete range of target thicknesses and the fluctuations from shot to shot are relatively high, we did not recognize any clear correlation between the spectral properties and the thickness of the target. Even in the thickness regime where transparency occurs, no direct correlation is visible. This indicates that the spectral modulations only arise because of the different laser intensities and the temporal contrast changes, resulting in different preplasma conditions. This also indicates that even when transparency of the target occurs, the spectral modulations might mainly arise from the HB at the beginning of the interaction and the transparency effects are comparatively small.
For an upcoming comparison with the simulation in Sec. 4.5, the averaged properties for each contrast condition and beamtime are calculated, including the corresponding un-

certainties given by the PTV of the minimum and maximum measured value. This results in a central wavelength of $(1049 \pm {}^{2}_{4})$ nm and $(1062 \pm {}^{10}_{6})$ nm with and without double PM respectively, for the experiment A. The maximum wavelength behaves similarly and is up-shifted by (12 ± 6) nm with double PM and $(45 \pm {}^{17}_{16})$ nm without PM.
As for the results of experiment B, the averaged central wavelength lies at $(1052 \pm {}^{8}_{5})$ nm and $(1056 \pm {}^{9}_{4})$ nm with and without PM. The maximum wavelength is also up-shifted by $(8 \pm {}^{12}_{9})$ nm and $(35 \pm {}^{23}_{11})$ nm with and without PM, respectively.
Since the time-integrated spectrum can not be used to determine the expansion velocity and therefore the temperature of the preplasma, the time analysis of the time-resolved measurement is necessary.

4.4 Time-resolved spectral analysis

The time-resolved measurement of the spectral properties after the interaction contains much more information about the preplasma properties than just the time-integrated ones. Therefore, the complex field of the laser pulse is extracted from the recorded FROG traces and the temporal phase is used to calculate the instantaneous wavelength as described in Sec. 3.3.4.
Similar to the analysis of the previous section, I averaged the data over all shots for each temporal contrast condition and the experiments are compared against each other. Figure 4.9 shows the results of the measurement without PMs and Fig. 4.10 shows the results with the increased contrast. The dashed lines represent the instantaneous wavelength and the temporal intensity is given by the solid lines, for the experiment A (red) or experiment B (blue). The colored areas indicate the uncertainty given by the PTV values of all measurements.
The measurements are centered on the first moment of the temporal pulse intensity. Let's go at first over the measurement without PM. The comparison shows that the pulse duration is shorter in case of experiment B. In the lower intensity regions, especially at the pulse front, the discrepancy of the instantaneous wavelength between both measurements increases. The instantaneous wavelength does not reach the predicted plateau at the beginning of the interaction, but the behavior is indicated by the rising wavelength at the beginning. When moving close to the maximum of the pulse intensity the behavior of the instantaneous wavelength is similar, including the transition into a slight blue shift after the pulse maximum.
In case of the time-resolved measurement with a PM, the behavior of both experiments, including the measurement range, is similar and the instantaneous wavelength of measurement A indicates a plateau at the beginning of the pulse. It is also visible that the mean instantaneous wavelength of experiment B shows an increased maximum red shift,

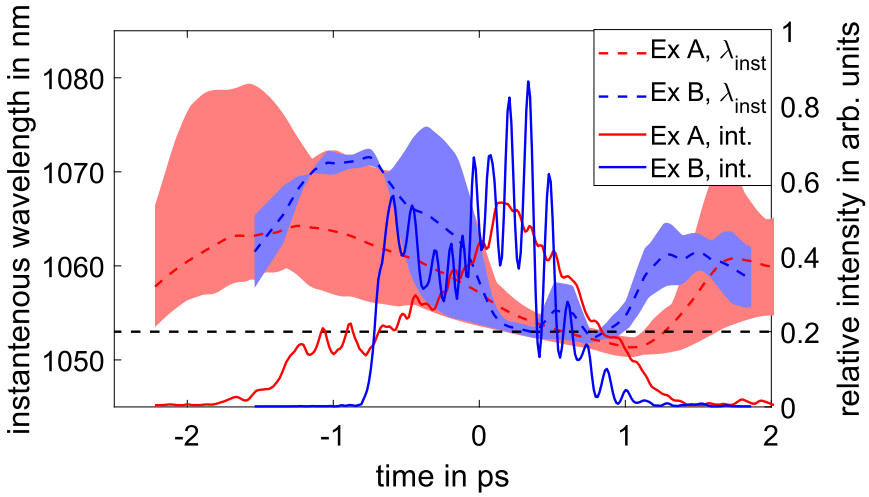

Figure 4.9: The graphs show the temporal evolution of the instantaneous wavelength for both the beamtimes A (red) and B (blue) without PM. The shaded area around the instantaneous wavelength corresponds to the uncertainty introduced by the shot-to-shot fluctuation, and the corresponding temporal pulse intensity given by the solid lines.

in combination with a reduced blue shift at the end of the interaction, in comparison to experiment A. This indicates the presence of an increased scale length during experiment B, when using a single PM. It can also be seen that the instantaneous wavelength only reaches the blue-shifted plateau of the initial plasma expansion in case of the high-contrast measurement of experiment A. Despite the high shot-to-shot fluctuations, the temporal evolution of the measured instantaneous wavelength matches the behavior predicted by the simulations, even if the plateau of the free plasma expansion is not reached by the measurement without pm.

As a cross-check the spectrum, which is reconstructed from the FROG trace, is compared to the measurement of the time-integrated spectrometer to validate the reconstruction. In case of experiment A, the reconstructed and measured spectra were in good agreement. In the case of experiment B, a large discrepancy was found for the low-wavelength region, which is shown in Fig. 4.11.

This low-wavelength region is also not observed in the measured FROG trace. The presence of a reduced wavelength range, due to a misalignment of the spectrometer within the FROG, was excluded by measuring a laser pulse which was spectrally broadened. To achieve such a broadened spectrum, the laser pulse with an energy in the micro-joule range was sent through a glass block multiple times. This lead to the effect of self-phase modulation, which spectrally broadened the laser pulse up to the regime of the missing wavelength. The measurement of this modified pulse with the FROG showed a good agreement with the separately measured time-integrated spectrum. Since the diagnostic based on SPIDER was also able to measure the full spectrum, even into the lower wave-

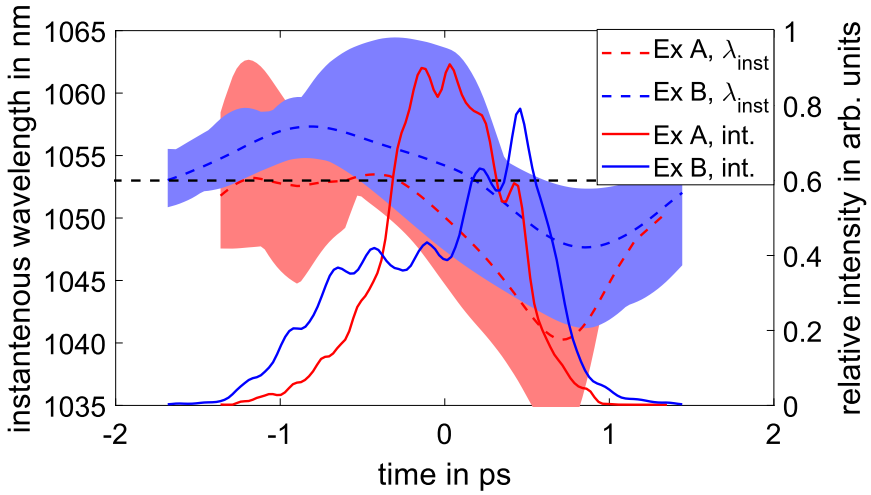

Figure 4.10: The graphs show the temporal evolution of the instantaneous wavelength for both the beamtimes A (red) and B (blue) with PM. The shaded area around the instantaneous wavelength corresponds to the uncertainty introduced by the shot-to-shot fluctuation, and the corresponding temporal pulse intensity given by the solid lines.

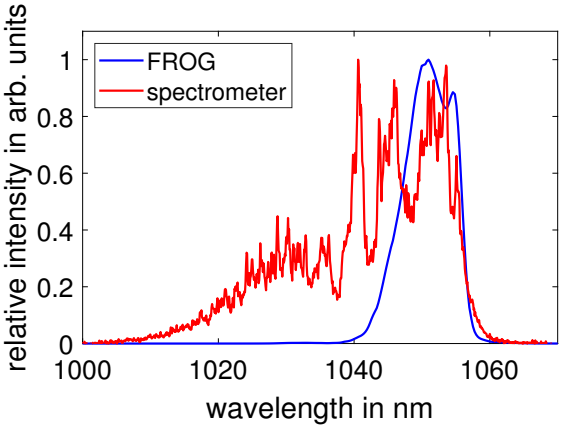

Figure 4.11: A comparison of a measurement with the time-integrated spectrometer (red) and the spectrum of the reconstructed FROG trace (blue) during experiment B. The high-pass cut-off at approximately 1040 nm for the FROG spectrum can be seen clearly.

length regime, the exact origin of the observed effect is not fully understood and has to be examined during future experiments. For this reason only the time-resolved measurements of experiment A are compared to the simulation results.

4.5 Comparison with the simulation

The experimental measurement of the reflected spectrum shows a similar behavior as seen in the simulation. Therefore, the next step would be to compare the measured time-integrated and time-resolved spectral properties with the findings of the numerical simulations. Since an as yet unexplained FROG artifact has falsified the measurement of experiment B, I only use the results of experiment A.
For a direct comparison with simulations of different preplasma scale lengths, the simulations have to use the same laser intensities as in the experimental condition. Therefore, the simulations were repeated for intensities of 1×10^{20} W/cm^2 and 2.4×10^{20} W/cm^2, which represent the intensities with and without the double PM respectively. In addition to this, the incidence angle of the simulation is adapted to 30°. The preplasma scale lengths are a result of the different initial temperatures, again ranging from 10 eV up to 7 keV, as described in Sec. 3.3.2. The time-integrated spectral properties of the conducted simulations for the various plasma scale lengths are represented by the colored dots in Fig. 4.12. These can be compared with the averaged spectral properties measured with and without the double PM, obtained from Sec. 4.3. The experimental measurements are indicated by the solid blue and red lines in Fig. 4.12 for the case with and without PM, with the corresponding uncertainty given by the PTV of the measurements.
The areas where the simulation results overlap with the measurement and corresponding uncertainty can be used to estimate the scale length. For a better comparison with the experimental results, the red shift of the spectrum is calculated from the holeboring velocity (Eq. 50), using a pulse duration of 500 fs and a fully ionized CH plasma (Z = 7, M_i = 13u). The resulting maximum wavelength for different scale lengths is given by the dashed colored lines in Fig. 4.12b, for the case with PM (blue) and without PM (red). The scale length is taken from the region that agrees best with the analytical description, giving an upper and lower limit for each temporal contrast option. This results in an estimation of the scale length of (0.18 ± 0.11) µm and (0.83 ± 0.39) µm, with and without PM respectively.
Apart from the comparison of the spectral shifts it is also interesting to compare the instantaneous wavelength of the simulation and measurements. The averaged time-resolved measurement is shown in Fig. 4.13 (left), with the uncertainty given by the PTV. For a better visibility the uncertainty of the pulse intensity is not included in the figure. The time ambiguity of the SHG-FROG is overcome by a comparison with the simulation. These showed that the highest red shift occurred prior to the maximum intensity of the reflected pulse. Accordingly, the individual experimental traces were time-flipped before averaging to match this observation from the simulation.
As an example, the right hand side of Fig. 4.13 therefore shows simulations with a scale length of of L_c = 0.02 µm (blue) and L_c = 0.26 µm (red). Even though the time range

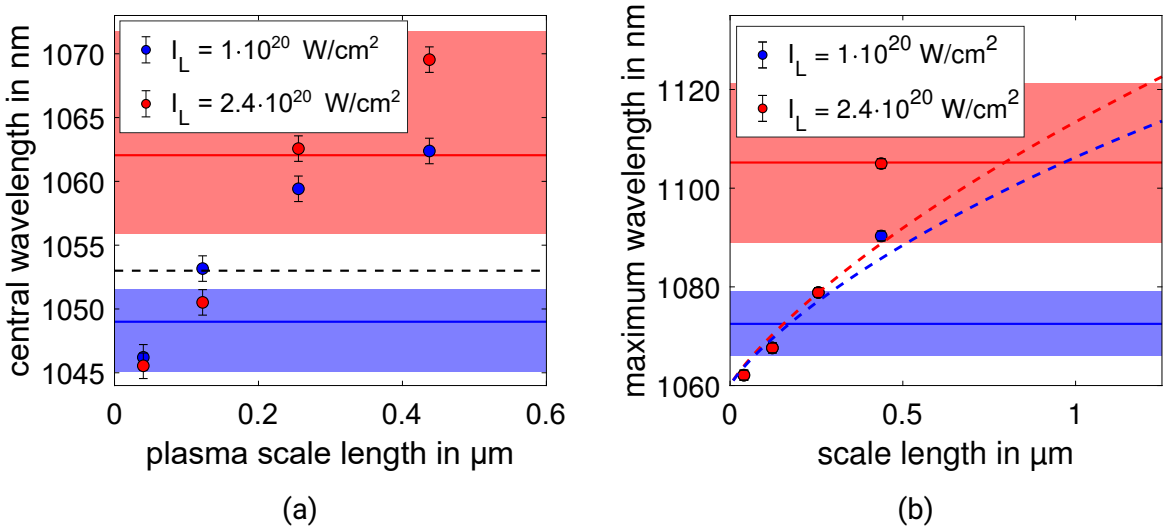

Figure 4.12: (a) The colored dots represent the central wavelength of the reflected spectrum for the PIC simulations with intensities of 1×10^{20} W/cm^2 and 2.4×10^{20} W/cm^2, as a function of the preplasma scale length. The blue and red solid lines correspond to the mean central wavelength of all experimental shots with and without double PM, whereas the shaded region indicates the range between the found PTV. The dashed black line corresponds to the central wavelength of the incoming laser pulse. (b) The plot shows the maximum wavelength after the interaction for the PIC simulation and the averaged experimental values and the calculated maximum wavelength from the analytical model (colored dashed lines).

is shortened, because of the pulse-duration reduction, it can be seen that the behavior between the experimental measurement and the simulation is similar. A reduced red shift is visible in the presence of a high temporal contrast or low scale length, respectively. Close to the maximum of the reflected intensity, the wavelength tends to be more and more blue shifted, which corresponds to the later expansion of the heated plasma in the simulation. The strength of the blue shift at later times is much lower than predicted by the simulation, which might correspond to a much lower pressure of the heated plasma. In contrast to the simulation results, the initial blue shift introduced by the expansion of the preplasma is not visible for the low contrast measurements. As already described in Sec. 3.3.10, this region can not be resolved if the dynamic range of the measurement is too low. This would mean that the measurement starts at a time where the laser pulse is already within the HB regime and a red shift is observed. Therefore, the measurement without PM at $\approx$-2 ps might correspond to a region at $\approx$-0.2 ps in case of the simulation. A possibility for the large time difference might be given by the laser-pulse shape that is present within the experiment. This is visible when calculating the instantaneous wavelength from the analytical description of the HB velocity (Eq. 50), for different laser pulse

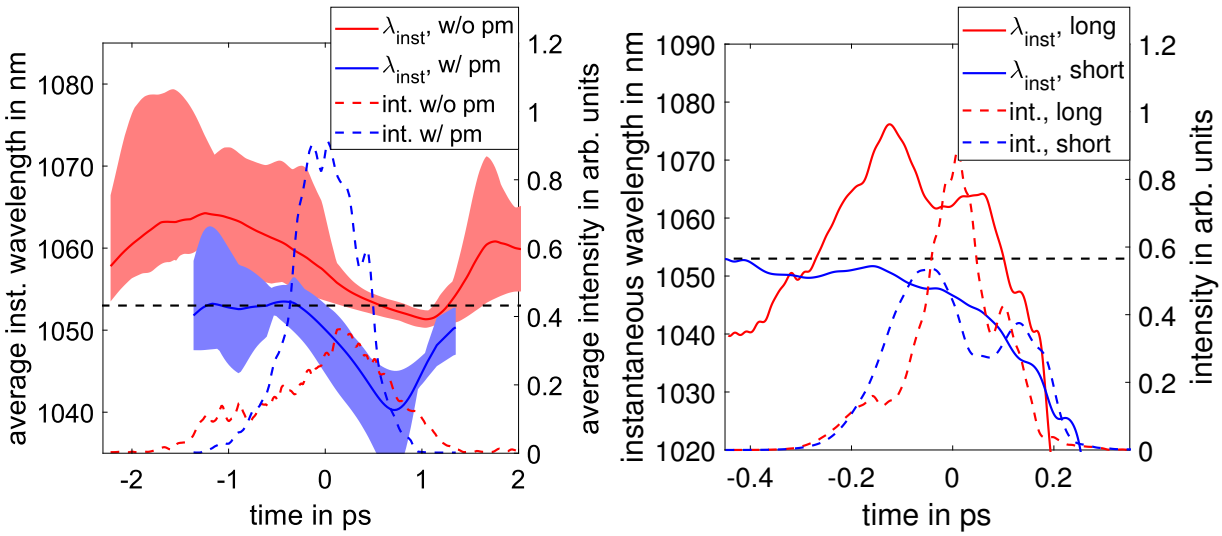

Figure 4.13: Comparison of the experimental instantaneous wavelength with and without PM in the temporal domain (left). The solid lines represent the mean value of all shots with the corresponding uncertainty, given by the PTV values. The dashed blue and red line show the averaged pulse intensity for each condition, normalized to its integral and the dashed black line shows the central wavelength of the incoming laser pulse. The right hand side image shows the PIC simulation for a scale length of L_C = 0.02 µm (short) and L_C = 0.26 µm (long) showing a similar evolution for both cases. Additionally, the calculated maximum wavelength is given by the colored dashed lines for the two laser intensities.

shapes which are shown in the right hand side of Fig. 4.14.
This includes an ideal Gaussian pulse, with a pulse duration (FWHM) of 500 fs (yellow), the experimentally measured incoming laser pulse as described in Sec. 4.2 (blue) and an example for a non-ideal intensity distribution (black). The left hand side of Fig. 4.14 shows the resulting instantaneous wavelength for the different pulse shapes with an arbitrary velocity offset of 0.01 c, including the measurement of the instantaneous wavelength without PM (red dashed line). This shows that a rather small deviation from the ideal Gaussian pulse shape already changes the instantaneous wavelength evolution, which might be the reason for the relatively high shot-to-shot fluctuation in the measurements. Since only a small part of the beam is used for the measurement of the incoming laser pulse, such a difference in the pulse shape might be possible. A further possibility is the uncertainty of the instantaneous wavelength of the incoming laser pulse described in Sec. 4.2, which would be either compensated or enhanced by the initial shift during the laser plasma interaction. With an increased dynamic range and control of the incoming laser pulse, this type of measurement will also yield a lot of information that can be extracted and used to determine the preplasma conditions.

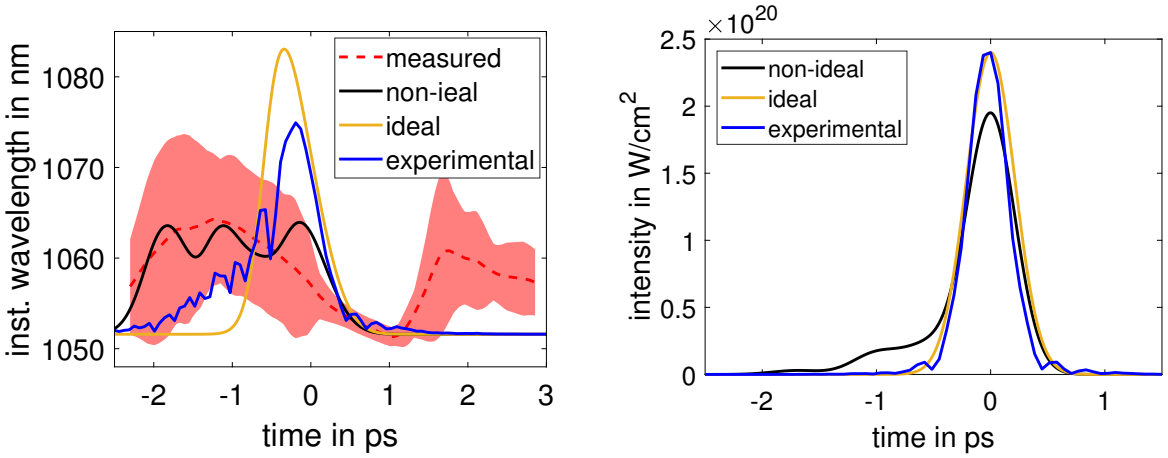

Figure 4.14: (left) Comparison of the experimentally measured instantaneous wavelength without PM (dashed red) with the wavelength shift calculated from the analytical description of the HB velocity for different laser pulse shapes. (right) The different laser pulses used for the calculation are an ideal Gaussian pulse (yellow), the experimentally measured incoming laser pulse (blue) and a assumed non-ideal intensity distribution (black).

4.6 Conclusion

The previous sections have shown that the spectral modulation of the laser pulse after the interaction with a plasma is strongly influenced by the state of the preplasma, which is again influenced by the temporal contrast of the laser pulse. The setup to determine the preplasma properties by measuring the spectral modulation may seem easy to set up, but the implementation is not straightforward and the laser conditions have to be exactly known. To ensure a stable measurement of the reflected pulse, the interaction region of the laser and target has to be imaged onto the diagnostics. In addition to this, the knowledge of the incoming temporal phase is very important, since any initial shift at the beginning of the laser pulse might enhance or compensate the spectral shift, which is introduced by the preplasma expansion.

To be able to see the effect of different scale lengths on the spectral properties of the reflected laser pulse in the experiment, the preplasma conditions had to be varied. The chosen way to do this within the experiment was to tune the temporal contrast by the use of a single or a double PM setup in two different experimental campaigns. By measuring the time-integrated spectrum during both experiments for the different preplasma states, many of the predictions given by the numerical simulation were observed.

The measured spectrum is either blue-shifted if the temporal contrast is increased, or red-shifted if no PM is used. Additionally, when the single PM is used, the spectrum is less blue-shifted in comparison to the double PM, which matches the increased temporal contrast in the second case. For both experiments, the strength of the blue shift did not

increase when the laser energy on target is increased. This indicates the existence of a threshold scale length, at which the HB starts to be capable of dominating the interaction, which is also in agreement with the numerical simulation.
In contrast to this, an energy dependency is observed when the PMs are removed, which leads to the formation of a more extent preplasma because of the lower temporal contrast, allowing a stronger HB. These spectral properties did not correlate with the used target thickness, even into the regime where a significant amount of transparency occurs. This indicates that the spectral modulation might mainly arise from the HB at the beginning of the interaction, and the transparency effects are comparatively small.
A direct comparison of the experimental time-integrated spectra with the analytical description of the holeboring velocity enabled the possibility to measure the preplasma scale length during the experiment. The corresponding scale length is determined to be (0.18 ± 0.11) µm and (0.83 ± 0.39) µm, with and without the PM respectively. This might correspond to a lower limit, since simulations in a similar regime indicate that the HB is less dominant in 3-D compared to 2-D [104]. This would lead to an increased red shift and acceleration within the simulation and therefore indicate that a higher scale length is present in the experimental conditions.
In addition, the reflected light could be successfully measured using the time-resolved diagnostic FROG. The corresponding wavelength-change shows a reduced maximum red shift in case of an increased temporal contrast. This red shift is then compensated by the following expansion of the heated plasma, until a blue shift occurs. The blue shift at later interaction times is much lower than predicted by the simulations. One reason for this could be an larger spatial distribution of the laser energy, again due to the difference between 2-D, in the simulation, and 3-D, which yields a lower temperature and electron density ahead of the pulse, therefore lowering the plasma pressure. The dynamic range was not sufficient to resolve the velocity of the freely expanding plasma and the acceleration a the beginning of the interaction to determine the preplasma temperature and scale length.
Nevertheless, the tendency towards lower wavelengths is indicated by the instantaneous wavelengths and the general behavior shows a qualitatively good agreement with the simulation. By increasing the dynamic range of the measurement and better controlling the incoming laser pulse in future experiments, the necessary region can be resolved and the gathered information used to confirm the simulation, and afterwards use the initial shift and acceleration to gather information about the preplasma properties. This suits such type of measurement as a diagnostic tool for the preplasma properties in LPI experiments.

5 Enhancement of the ion acceleration at PHELIX

The study of the preplasma properties during LPI is embedded in the wider theme of laser-driven ion acceleration at PHELIX. As presented in Sec. 2.3, not only does the preplasma condition have a strong influence on the particle beam in terms of maximum reachable energy and particle number, but one must also pay attention to other experimental parameters like the target thickness, absorption and laser intensity. In the following sections, two methods to enhance the energy yield in laser particle acceleration will be discussed. The results obtained when applying these methods to the PHELIX facility will be presented afterwards.
For this study, two experimental campaigns were conducted with a different emphasis each. The first experiment focuses on the enhancement of the laser absorption, while utilizing fully opaque targets in the thickness regime of 1 µm and above, which showed no transmission (Sec. 4.3). The second experiment prioritizes the interaction in the relativistic transparency regime with a target thickness of 300 nm, while enhancing the laser intensity. Both campaigns featured a similar setup and laser parameters, which will be described first, followed by the results.

5.1 Experimental setup and laser performance

The schematic setup of the conducted experiments is shown in Fig. 5.1. The system provides an s-polarized beam, which is able to deliver a maximum on-target energy of 180 J. This beam is focused to a spot size of ≈ 4 µm (FWHM) on the target, by using a f/1.7 off-axis diamond turned copper parabola. With a laser pulse duration equal to 500 fs, this corresponds to a maximum achievable intensity of 5×10^{20} W/cm^2. The laser interacts with a micrometer or sub-micrometer-thick target with varying incidence angle.
To detect the accelerated ions, a stack of radiochromic film (RCF), which are layered between mylar sheets, is placed behind the target. These RCFs are stained during the interaction with an ion, whereby the intensity of the color is directly correlated to the deposited energy in the film. The position of this stack is changed depending on the experimental campaign. For the first experiment, which uses an interaction angle of 45°, the stack is placed in TNSA-direction at a distance of 5 cm. During the second experiment, the interaction angle is decreased to 5° and the stack is placed at a distance of 10 cm in laser direction to avoid the pollution of the target chamber, induced by a strong ablation of the first layer of the stack by the light leaking through the thin target.
In addition to the RCF stack, a Thomson parabola [105] is used as a complementary ion diagnostic during the second experiment. Since it requires a direct line of sight to the ion source, a 5-mm hole is drilled into the RCF stack and the diagnostic is placed at a distance

of 50 cm in laser direction (0°). The Thomson parabola uses an electric and magnetic field to deflect the incoming ions onto an image plate. Depending on the energy and charge-to-mass ratio of the ions, this deflection results in separated traces on the image plate, which enables an evaluation of the ion spectrum in terms of ion energy and species. This can be used to detect protons with energies up to 90 MeV with an uncertainty of 5 %, for this Thomson parabola. For a subsequent energy calibration and to shield the image plate from heavy ions, copper plates, with a thickness ranging from 0.5 mm at lower energies, up to 5 mm for the higher proton energies, are mounted directly onto the image plate.

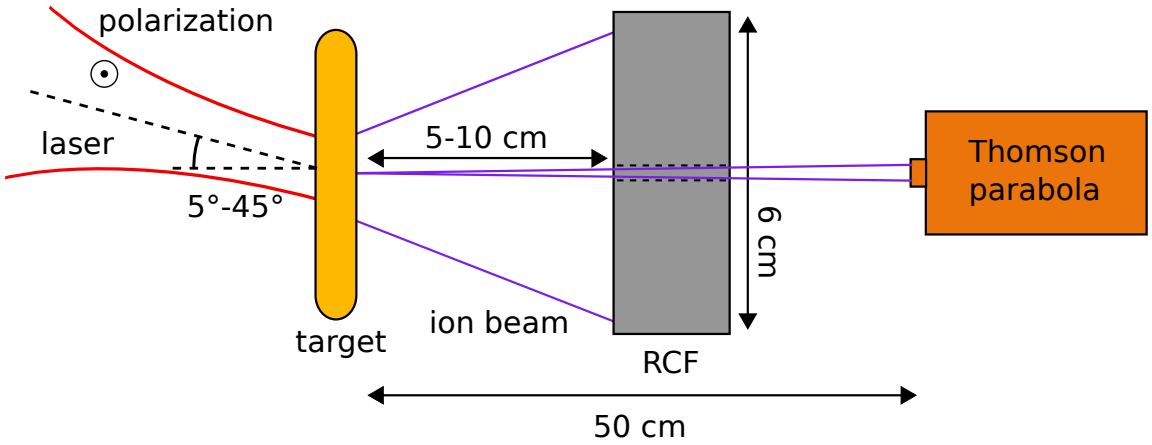

Figure 5.1: Schematic top view of the setup that is used for the laser-ion acceleration. The laser is focused onto a thin target with varying incidence angle. In the first setup, the RCF stack is placed in direction of the target normal at an angle of 45° and a distance of 5 cm, to detect the ions. In the second experiment, the incidence angle is changed to 5° and the RCFs, together with the Thomson parabola, are placed in laser direction.

The target-foils are attached to a small 500 µm-thin supporting-plate with an opening of 5 mm which enables the possibility to mount the targets at an incidence angle of 45° without perturbing the accelerated ions. The target thickness and material is changed between the different setups. In the case of an incidence angle close to normal, which aims at the ion acceleration in the regime of relativistic transparency as described in Sec. 2.3.2, 300-nm-thin polystyrene targets are used. For the second setup, which focuses on staying within the regime of TNSA, the target material is changed to gold and the target thickness is increased up to 1 µm and 10 µm. As described in Sec. 2.3 the maximum energy of the accelerated ions increases for higher laser intensities, independent on the acceleration mechanism. Since the laser intensity can not be measured directly, it has to be inferred from the measurement of the pulse duration, the pulse energy and the focal-spot fluence distribution after the last focusing optic.

The measurement of the on-shot laser energy is performed with a pyroelectric detector which is placed behind a leaky mirror, located at the output of the main amplifier of the system. This energy measurement is cross-calibrated with a second detector that can be moved into the full-aperture beam. Since the compressor of the system, which is placed between the main amplifier and the target chamber, introduces additional losses, the reduction of energy is calibrated by a measurement within the target chamber. This enables a measurement of the on-target laser pulse energy with an uncertainty of $\approx 5\,\%$.
A larger uncertainty is given by the measurement of the focal spot. The on-shot distribution has to be deduced from separate measurements, because of the inaccessibility of a direct measurement. In case of the PHELIX system, the focal spot is measured during alignment mode, which is performed by directly image-relaying the focal plane to the center of a 16-bit camera (Hamamatsu ORCA-flash4.0 LT), which is located outside of the target chamber. The corresponding spatial distribution of the fluence is recorded prior to each shot, in addition to a measurement of this distribution at a diagnostic that is located at the compressor. At this location, the focal distribution can also be measured on-shot. The difference between both measurements can be used to define an on-shot correction factor, which compares the fluence of both locations. The correction factor is given by the ratio between the maximum of the measured signal on-shot and the maximum that is measured prior to the shot, whereas both distributions have been normalized to the integral of the signal. The measurement of this ratio shows that the on-shot intensity reduces to $(75 \pm 7)\,\%$ of the initially estimated intensity during the alignment mode. The reason for this difference is given by the on-shot aberrations occurring in the laser chain, as well as a change of the beam profile from being close to Gaussian during the alignment, to a flat-top profile on-shot.
Another uncertainty is introduced by the measurement of the pulse duration by the FROG-device, which was presented in Sec. 4.2. The measurement during alignment mode, which is also compared to a measurement with full laser energy, results in a pulse duration of 500 fs FWHM. The uncertainty is mainly given by the fluctuation of the reconstruction algorithm, which results in a variation of the pulse duration by $\approx 15\,\%$ (PTV). Besides the knowledge of temporal pulse shape at the maximum, the knowledge of the temporal profile of the pulse on a high dynamic range is essential for the interaction. As described in Sec. 2.5 the composition of the temporal contrast may alter the target condition and influences the ion acceleration. The properties of the temporal contrast of PHELIX has been described in Sec. 4.1, showing an ASE-contrast of 10^{-12} on the ns-scale which can be reduced to 10^{-6}.
The mentioned parameters of the laser pulse have a strong impact on the process of laser-ion acceleration and therefore influence the maximum reachable proton energy. Most of these parameters, like the pulse duration and maximum laser energy, are difficult to

improve without making large changes to the laser system itself. Therefore, the first goal is to increase the maximum proton energy by increasing the absorption of the laser energy on the target, with an incidence angle of 45°.

5.2 Effect of increased laser absorption on the maximum proton energy

There are two strategies that can be implemented to increase the laser absorption. As described in Sec. 2.2.3 many absorption mechanisms at relativistic intensities arise if the laser pulse contains a p-polarized component with respect to the target. The polarization of the system is given by the pulse compressor of the system, which only works for an s-polarized beam at PHELIX. A rotation of the polarization using a waveplate after the compressor is not straightforward, mainly due to the large size of the beam of 28 cm which complicates the manufacturing and implementation. The easiest way to achieve this is by rotating the target along the horizontal axis, perpendicular to the laser direction. This setup has been used in combination with a high temporal contrast of 10^{-12} and 1 µm-thick gold targets.
Another possibility is to increase the extent and therefore scale length of the preplasma, which has been described in Sec. 2.3.1, by decreasing the temporal contrast on the nanosecond scale. Such technique has been tested during previous experiments at the PHELIX laser [12]. In the presence of a nanosecond temporal contrast of 10^{-6}, a density of $\approx 10^{20}$ cm^{-3} is reached $\approx$ 30-40 µm in front of the initial target surface. As a comparison, this density is reached approximately 5 µm before the initial target surface in case of the highest available temporal contrast [12]. When using this method, the target thickness has to be increased to prevent the laser from burning through the foil. In this case, the thickness of the targets is increased to 10 µm.
Since the rotation of the target changes the direction of the accelerated protons out of the horizontal laser plane, only the RCF stack can be used as an ion diagnostic and the Thomson parabola is removed from the setup.
These two setups are compared with a standard setup using the s-polarized beam, a high temporal contrast and 1 µm-thick gold targets. The intensity on-target is changed by reducing the laser pulse energy and the maximum proton energy is recorded, with the corresponding results that are shown in Fig. 5.2.
With the low temporal contrast in combination with the 10 µm-thick target, proton energies up to 38 MeV are achieved (green), which is systematically lower than the standard option with approximately 15 % higher proton energies (red). This indicates that the increased preplasma formation does not compensate for the increased target thickness. This might be overcome if the target thickness is slightly decreased, which has not been tested during this experiment.

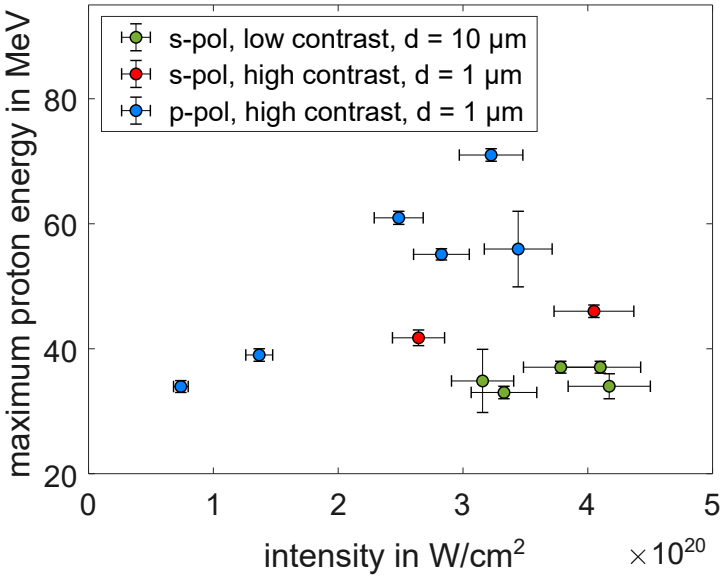

Figure 5.2: Intensity-dependent maximum proton energy for the different contrast levels, target thicknesses and laser polarization, with an incidence angle of 45°.

On the contrary, when changing only the laser polarization, the maximum proton energy is increased by ≈ 60 % up to 71 MeV (blue), whereas an increase of the maximum energy was visible for all shots of this condition at similar intensity. One possible reason for this might be the increased effect of vacuum heating [106] because of the small plasma scale length during the interaction. This would lead to an increased electron temperature and therefore enhance the amount of particles that are accelerated via the TNSA mechanism and energies that are reachable. This increase of the accelerated particles is also shown by the proton spectra, which have been reconstructed from the RCF stack, for each configuration (Fig. 5.3). The detection threshold of the RCFs
The reconstructed proton spectra not only show an increased maximum proton energy, but also an enhanced number of accelerated protons. This in turn is associated with an increased conversion from laser to particle energy. This conversion efficiency for protons above 10 MeV is increased from 3.9 % up to 5.2 %. A similar behavior is visible when calculating the total number of accelerated particles in this region, which increases by ≈ 57 % up to 3.2×10^{12} particles. To achieve even higher proton energies, the intensity of the laser can be increased. The procedure to increase the laser intensity and the limits will be discussed in the following section.

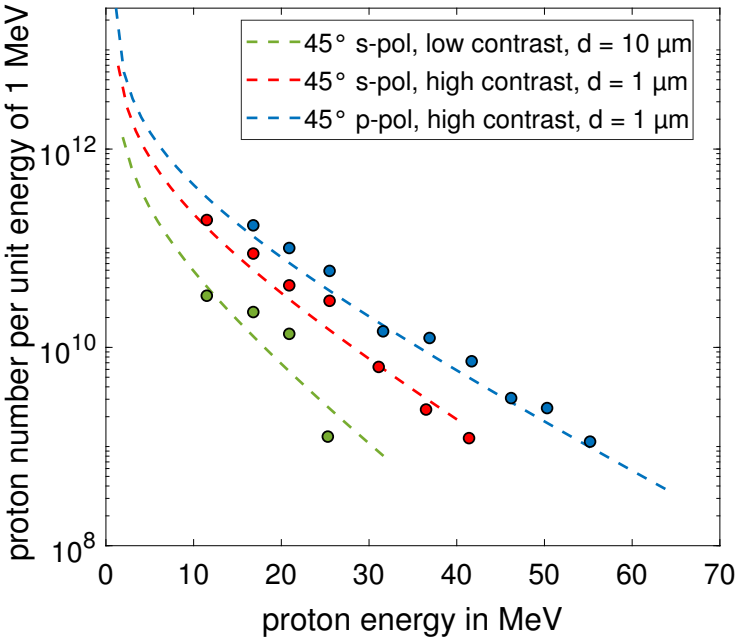

Figure 5.3: Proton spectrum for each configuration with comparable on-target laser intensity in the range of 3×10^{20} W/cm^2, whereby the dashed lines correspond to an exponential function that is obtained by a fit to the deposited energy in the RCF layers. The data given by the circles is obtained by sequential deconvolution of the signal from the last layer from the previous ones. The detection threshold of the RCFs in this configuration is $\approx 2 \times 10^8$ protons/sr.

5.3 Intensity scaling of the maximum proton energy

Another possibility to enhance the maximum reachable proton energy is to use the $I^{1/2}$-scaling [47] by increasing the maximum laser intensity. Since the pulse duration can not be reduced easily and the energy limit of 200 J, given by the damage threshold of the system, can not be exceeded, the only remaining possibility is to increase the focal spot quality. In order to do this, it is useful to divide the focal-spot degradation into two components, namely static and dynamic contributions. A closed-loop system using a deformable mirror located at the output of the pre-amplifier ensures a compensation of the wavefront distortion in the low- and mid-spatial frequencies up to the compressor input. In addition, low-spatial-order on-shot aberrations from the amplifier are pre-compensated for, instants before the shot. As a consequence, the Strehl ratio of the beam is very good up to the compressor input.

Therefore, the static degradation is mostly dominated by the wavefront error of the compressor gratings and the copper parabola with surface form tolerances of λ/3-λ/2 and λ/2 (PTV), respectively. Since the quality of the compressor grating is among the highest that is currently available, the diamond-turned parabola is exchanged by a dielectrically-coated

high-quality parabolic mirror with the same geometrical properties but a decreased wavefront error of λ/36 root mean square (RMS). The comparison of both focal spots before and after the exchange is shown in Fig. 5.4 (top). Both distributions have been normalized to the integral of the corresponding distribution.

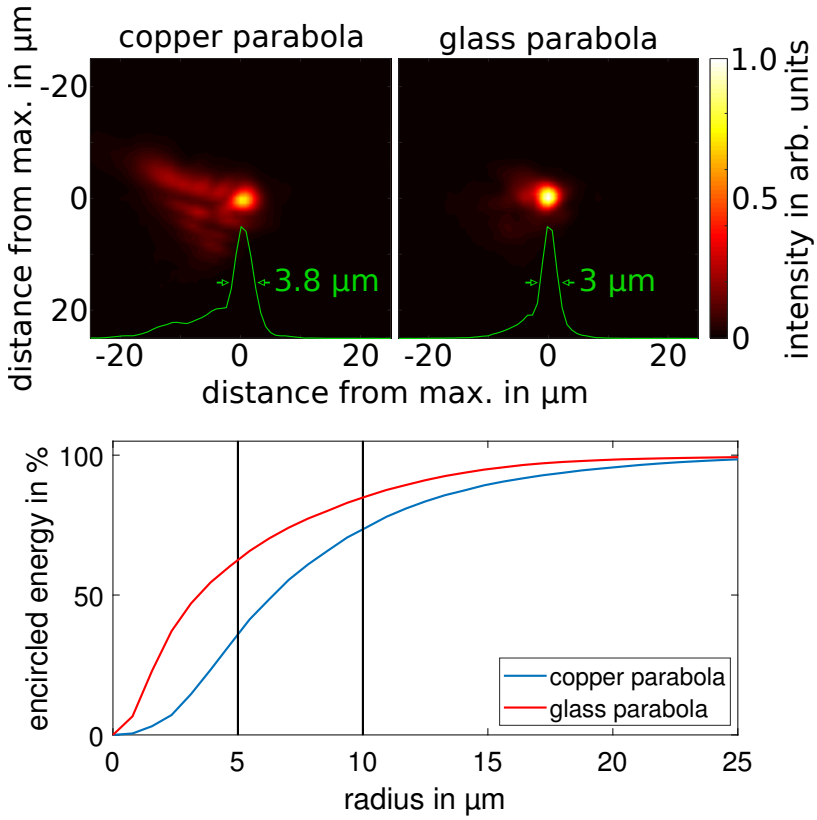

Figure 5.4: (Upper half) Comparison of the focal spot obtained with the copper parabola and glass parabola. The measurement is performed during alignment mode inside the target chamber, which shows the improvement of the focal spot. The green curve corresponds to the sum of the distribution in the vertical axis, with the corresponding FWHM of the foci. The lower part of the figure shows the encircled energy for both parabolas.

The implementation of the glass parabola reduces the energy distribution in the outer focal regions, while increasing the peak fluence. This is also indicated by the sum of the distribution in the vertical axis, given by the green line, showing a reduced width of the focal spot.

This improvement can be quantified by calculating the encircled energy of the focus (Fig. 5.4, bottom), showing the energy contained in the focal spot at a certain distance from the center. It can be seen that the energy increases from 35 % up to 62 % within a radius of 5 µm and from 74 % to 85 % at a distance of 10 µm. This increased energy within the center of the focus raises the intensity by a factor of 2.8, up to $\approx 8 \times 10^{20}$ W/cm^2.

To observe the influence of the increased intensity on the ion acceleration, a second experiment has been performed. The effect of this enhanced intensity should result in an increased maximum proton energy, while maintaining the same scaling with the intensity as for the copper parabola. This is done by varying the laser energy on-target and measure the corresponding maximum proton energy for the different focusing parabolas. As mentioned, the laser pulse of varying intensity interacts with a 300 nm-thick polystyrene target at an incidence angle of 5°. At increased laser intensities the interaction with these thin targets showed signs of HB which is indicated by a strong blurred electron background on the RCFs [55], without any increase in the maximum proton energy. Therefore, the target thickness is increased to 1.5 µm, while maintaining the target material. The resulting maximum proton energies for the different conditions are shown in Fig. 5.5.

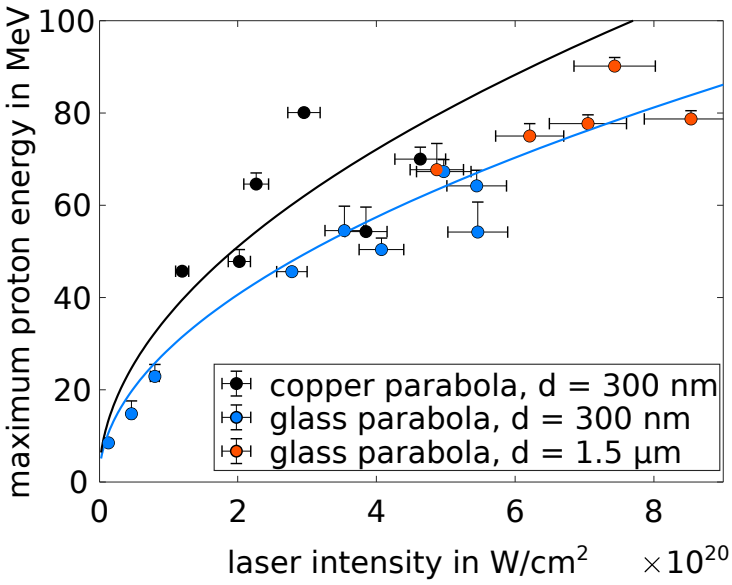

Figure 5.5: The scaling of the maximum proton energy is shown for different laser intensity, different focusing optics and target thicknesses. The black dots represent the energies obtained while using the copper parabola and a target thickness of 300 nm. The blue and red dots correspond to the energies obtained with the glass parabola and target thicknesses of 300 nm and 1.5 µm, respectively. The solid black and blue lines correspond to a square-root fit for the different scaling with the copper and glass parabola respectively.

With the setup of the glass parabola and the thick targets, a maximum proton energy of $90 \pm^{3}_{0}$ MeV has been reached for an intensity of 7×10^{20} W/cm^2. This proton energy is comparable to the maximum proton energy of other facilities for similar laser intensities [67, 70], whereas these facilities used much thinner targets in the nanometer range. The corresponding last five RCF layers of this shot can be seen in Fig. 5.6a. The signal of the protons, which is indicated by the green arrow at the penultimate layer, is blurred due to straggling of the proton beam within the RCF stack. The resulting proton signal can

not be easily distinguished from the electron signal, which is usually done by looking for sharp features on the RCF. Instead, the gradient of the signal between each RCF layer is used to differentiate between the signals, which is lower for the electron signal than for signal generated by the protons. As a comparison the signal at the Thomson parabola is analyzed, measured within the white region in the middle of the RCFs in Fig. 5.6a. The measured trace is shown in Fig. 5.6b with the corresponding analyzed spectrum given by Fig. 5.6c. The spectrum indicates a cut-off at approximately 85-90 MeV, which is consistent with the energy that is observed around the hole in the RCF stack.

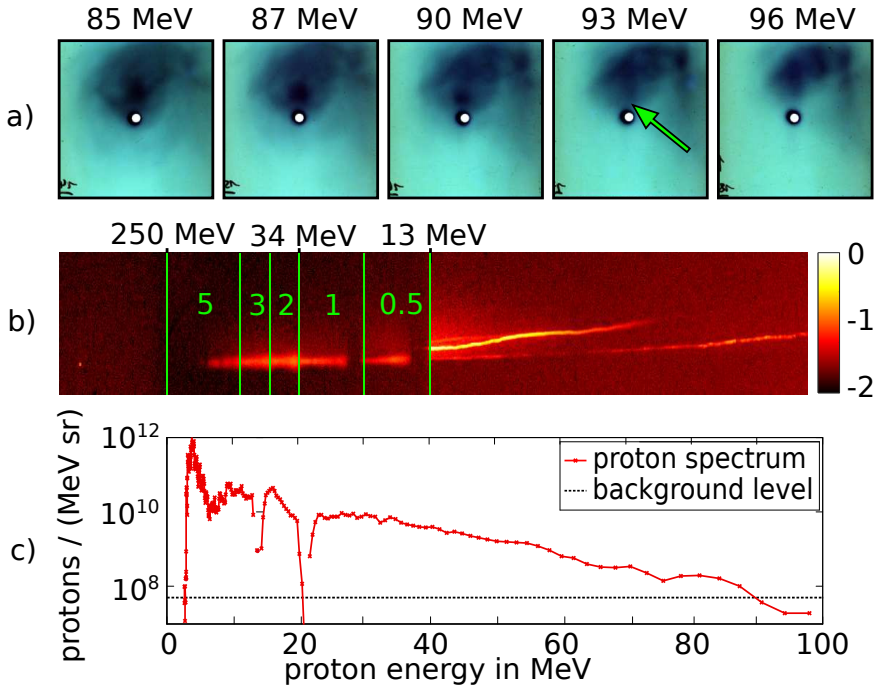

Figure 5.6: Image a) shows the signal at the last five RCF-layers, with an enhanced contrast to increase the visibility of the protons with the highest energy, indicated by the green arrow. This shows a maximum proton energy of at least 90 MeV, with a possible extent to 93 MeV. Image b) shows the trace obtained from the Thomson parabola, that is generated by the protons that passed the hole within the RCF stack. The lines indicate the position of the copper filters used to block heavier ions, with the corresponding thickness in mm. Image c) shows the spectrum that is extracted from the Thomson-parabola trace with a transition into the background level at approximately 85-90 MeV.

Besides reaching a new record for the accelerated protons at PHELIX, the maximum energy is only a slight improvement to the one measurement by Wagner *et al.* [107], which was also performed at the PHELIX facility. To examine the reason for this behavior, the scaling of the maximum proton energy with the on-target laser intensity is calculated. This is done by a square-root fit with the laser intensity, for the different setups, which is given by solid black line for the copper parabola and the blue line for the glass parabola,

including all target thicknesses (Fig. 5.5). First, a scattering of the measurement points with respect to the found curve is visible, which reaches a deviation of more than 20 % for the copper parabola. Additionally, the two conditions show a different intensity scaling, in contrast to the assumption of one scaling with an extension to higher proton energies when the intensity is increased by the glass parabola.
One possible explanation could be a systematic error in the calculation of the laser intensity, which results in a deviation from the expected behavior. This would occur if the improvement that is introduced by the glass parabola is covered by on-shot aberrations occurring within the system. One of these aberrations could be given by a defocus that changes the position of the focal spot. Since the glass parabola only improves the beam quality in the diffraction limited regime of the focus, but not in the outer regions, this effect of the improvement would be lost if the beam is defocused. Such a defocus is easy to introduce, because of the short Rayleigh range of ≈ 10 µm, and might also be given by the pre-expansion of the target which moves the position of the interaction region. On the contrary, the necessity to increase the target thickness when changing the parabola from copper to glass, is a validation of the increased laser intensity in the second case.
Since the glass parabola leads to a redistribution of the energy, from the outer regions of the focal spot into its center, the gain for the ion acceleration might not be as high as expected. A redistribution would therefore increase the impact in the center and reduce the contribution from the outer region. In total, the effect on the ion acceleration would only be marginally improved.
As a validation, the measured maximum proton energies are compared to a scaling with the laser peak power instead of the laser intensity. The result of the maximum proton energy for the laser power is shown in Fig. 5.7, which corresponds to a variation of laser energy. As already shown by Robson *et al.* [108], this shows a better agreement of the measurements for the different conditions, especially in the lower or energy range. The blue and black lines, which almost perfectly match each other, correspond to a power scaling of the maximum proton energy, given by Zeil *et al.* [53], with a conversion efficiency from laser energy to electron energy of 14 %. The found scaling agrees very well with the measured proton energies. Only in the region of high laser power, the deviation increases up to 34 %, which might indicate that the acceleration process might not be purely dominated by TNSA. Different acceleration mechanisms might be enabled in this regime, even though no direct evidence for this assumption can be given.
The conclusion is that the use of a better optical focusing element only slightly improves the ion acceleration, reaching a new proton energy record of $90 \pm^{3}_{0}$ MeV, that are accelerated with PHELIX. This slight improvement is backed up by the finding that the maximum ion energy rather scales with the laser peak power, instead of the laser intensity, showing that laser-ion acceleration in the TNSA regime does not strongly depend on the quality of

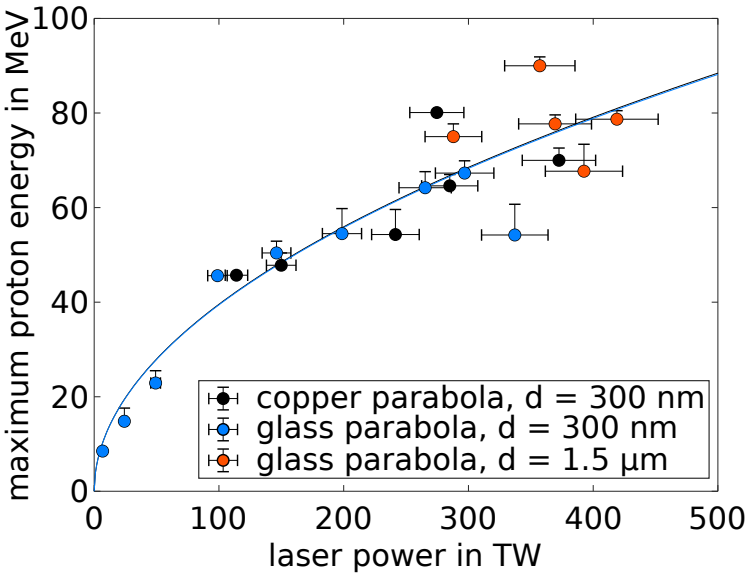

Figure 5.7: The maximum proton energy in dependence on the laser power is shown for the the copper parabola (black dots) and the glass parabola for the target thickness of 300 nm (blue) and 1.5 µm (red). Since the pulse duration is kept constant, this corresponds to a change of the laser energy, which results in a better agreement between the different conditions [108]. The colored lines, which almost perfectly match each other, represent the corresponding scaling with the laser-power-scaling, given by Zeil *et al.* [53].

the focal spot.
This indicates that the maximum proton energy rather scales with the laser power on-target than the laser intensity and an improvement to the focal spot does not strongly influence the acceleration process. Therefore, the proton energy scaling from the first experiment can also be compared to the ones of the second experiment. The corresponding power scaling of the maximum proton energy for these two cases are shown in Fig. 5.8. The blue dots represent the interaction with an s-polarized laser and an incidence angle of 5°, and the red dots correspond to the setup with an incidence angle of 45° and the p-polarization. The corresponding fit to the scaling is given by the solid lines.
Despite the reduced laser intensity, which is introduced by the increased incidence angle, the scaling with the laser power is similar in both cases. This shows that the increased absorption while using the p-polarization cancels out the reduced intensity, and similar maximum proton energies can be achieved while utilizing completely different laser and target setups.

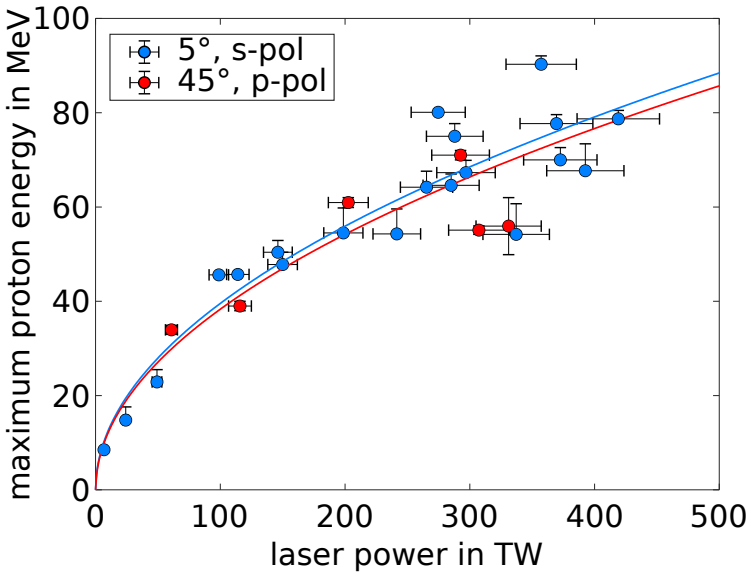

Figure 5.8: Comparison of the scaling for the maximum proton energy with the laser peak power, for the first beamtime with a p-polarized laser pulse and an incidence angle of 45° (red) and the beamtime close to normal incidence with s-polarization (blue). Both experiments, which were conducted with a high temporal contrast, show a good agreement between the different scaling.

5.4 Conclusion

During this sections, two experimental campaigns have been presented which focused on the improvement of the maximum proton energy at PHELIX. The first campaign focused on the improvement of the laser absorption, first by changing the polarization of the laser pulse from s- to p-polarization, while using 1-µm-thin targets and second by reducing the temporal contrast on the nanosecond scale to 10^{-6}, and increasing the target thickness to 10 µm. The latter method showed no improvement compared to the standard setup with high contrast, s-polarization and a target thickness of 1 µm. Changing the laser polarization on the other hand, lead to an increase in the maximum proton energy by ≈ 60 % up to 71 MeV, while increasing the amount of particles by ≈ 57 % up to 3.2×10^{12} protons above 10 MeV.

The second campaign focused on the improvement of the focal spot to achieve an increased intensity on-target, which is done by exchanging the last focusing optics to a glass parabola. With that, an increased laser intensity of up to 8×10^{20} W/cm^2 could be achieved. Even though the intensity could be improved by almost a factor of 3, the resulting maximum proton energy increased only by a small amount. This was backed up by the finding that the maximum ion energy does not scale with the laser intensity, but with the laser peak power in case of the conducted experiments. Nevertheless, a new

record for protons accelerated with PHELIX could be achieved with a maximum energy of $90 \pm^{3}_{0}$ MeV. The found scaling also matched the measurements of the previous experiment with a p-polarized laser pulse, despite the completely different incident angles. The results presented within these sections were published in the journal "High-Power Laser Science and Engineering" [96].

6 Summary and conclusion

The goal of this work was to develop and verify a principle to determine the preplasma properties by measuring the light that is reflected during the laser-plasma interaction. This has been done with the help of numerical simulations, as well as the measurement of the reflected laser pulse during two experimental campaigns.
The findings of the numerical modeling and reflection measurements will be summarized in the following, including the additional part of this work which focused on the enhancement of the ion-acceleration at PHELIX.

6.1 Numerical simulation results

The numerical 2-D PIC simulations have shown that the reflected light contains plenty of information about the preplasma. The influence of the preplasma properties on the reflected light has been simulated for various laser intensities from 10^{18} W/cm^2 to 10^{21} W/cm^2 at a pulse duration of 250 fs and different preplasma conditions. With the help of a time-resolved analysis of the Doppler shift, the movement of the critical density can be tracked throughout the interaction.
A clear correlation between spectral laser-pulse properties and the preplasma parameters has been found, especially at early interaction times, where the light pressure is smaller than the pressure of the expanding plasma. This region contains information about the preplasma state picoseconds prior to the arrival of the peak laser intensity.
The initial blue shift of the pulse spectrum can be correlated to the expansion velocity of the plasma. With the assumption of a one-dimensional expansion, following the Samir model, this expansion velocity can be used to calculate the electron temperature of the preplasma. The comparison with the two-dimensional preplasma expansion obtained from the numerical simulation shows a good agreement with the 1-D Samir model for the conditions met at modern laser facilities like PHELIX. This early-interaction region additionally contains information about the scale length of the preplasma. When the intensity rises and the light pressure overcomes the plasma pressure, holeboring occurs and the critical density is pushed into the higher density region. The initial acceleration of this movement increases for higher laser intensities, as well as in the presence of longer scale length plasmas.
An analytical description of the HB velocity, which included the assumption of a density change during the HB, and the corresponding acceleration was derived which enabled the possibility to calculate the maximum HB acceleration between 400 fs and 200 fs prior to the initial peak intensity. The resulting dependence of the acceleration on the laser intensity as well as the scale length is in very good agreement with the 2-D PIC simulation

results, even for an oblique incidence angle. As a remaining task, the influence of the dimensionality of the interaction on the correlation between scale length and acceleration has to be investigated. Nevertheless, the simulations indicate that the preplasma scale length in the micrometer to sub-micrometer regime can be determined by analyzing the temporally resolved spectral shift that is created at early interaction times.
Even when only analyzing the time-integrated spectrum after the interaction in terms of maximum wavelength and central wavelength, the scale length of the preplasma can be estimated. The presence of an increased maximum red shift in combination with a red-shifted central wavelength indicates a higher scale length of the preplasma. On the contrary, a blue-shifted central wavelength in combination to a low maximum red shift shows the presence of a plasma with a strong density gradient.
The simulations therefore indicate that this non-invasive single-shot method, which does not require any secondary probe beam, is able to measure scale length regimes currently not accessible by other types of diagnostics.

6.2 Reflection measurement results

The presented method to measure the preplasma properties has been investigated experimentally at the PHELIX facility during two experimental campaigns which features laser intensities up to 5×10^{20} W/cm^2 with on-target pulse energies up to 180 J, a laser pulse duration of 500 fs and an ASE contrast of 10^{-12}. Both campaigns featured a similar experimental setup in which the reflected light has been successfully measured in specular direction, with the help of a specifically designed time-resolved diagnostic based on FROG. Setting up the measurement is not straightforward and the laser conditions have to be exactly known to determine the spectral change of the laser pulse because of the interaction with the plasma. Therefore, the knowledge of the incoming temporal phase is very important, since any initial shift at the beginning of the laser pulse might enhance or compensate the spectral shift, which is introduced by the preplasma expansion. To ensure a stable measurement of the reflected pulse, the interaction region of the laser and target has to be imaged onto the diagnostics.
To validate the influence of the preplasma properties on the reflected light, the temporal contrast has been enhanced to reduce the formation of the preplasma. This has been done by implementing a single or double plasma mirror (PM) in the two experimental campaigns respectively.
The enhancement of the temporal contrast lead to a strong blue shifted spectrum after the interaction, in contrast to a red-shifted spectrum if no PM is used. Even the small difference of the temporal contrast between the single and double PM could be observed, which lead to a less blue-shifted spectrum when only one PM is used.

In the presence of a high temporal contrast, the strength of the blue shift did not increase when the on-target laser energy is increased, which has been observed for both experimental campaigns. This indicates the existence of a threshold scale length, at which the HB starts to be capable of dominating the interaction, which is also in agreement with the numerical simulation. When removing the PMs the preplasma formation is enhanced and a stronger HB is possible, resulting in an energy dependency of the spectral shift. The measurement of the time-integrated spectrum for the different preplasma states confirmed the behavior of the spectral changes, that were predicted on the basis of the numerical simulations.
It was also found that the spectral properties did not correlate with the used target thickness, even into the regime where a significant amount of transparency occurs. This indicates that the spectral modulation might mainly arise from the HB at the beginning of the interaction, and the spectral changes induced by the transparency of the target are comparatively small.
The time-integrated spectra were compared to the simulation, which enabled the possibility to estimate the preplasma scale length during the experiment. The corresponding scale length is determined to be (0.18 ± 0.11) µm and (0.83 ± 0.39) µm, with and without the PM respectively.
The time-resolved measurement of the laser pulse also showed a reduced maximum red shift in case of an increased temporal contrast. This red shift changes to a blue shift, which is introduced by the following expansion of the heated plasma. The behavior of the measured instantaneous wavelength showed a qualitatively good agreement with the simulation. By increasing the dynamic range of the measurement in future experiments and improving the measurement of the incoming laser pulse, the region to extract the initial wavelength shift and acceleration can be resolved and the gathered information used to additionally determine the preplasma properties with the time-resolved measurement.

6.3 Laser-ion acceleration

Besides the study of the correlation between preplasma properties and the spectral modulation of the reflected laser pulse, another part of this work focused on the enhancement of the laser-ion acceleration.
Our group conducted two experimental campaigns which focused on the improvement of the maximum proton energy at PHELIX. This has been done by improving the laser absorption, for an incidence angle between laser and target of 45°, first by changing the polarization of the laser pulse from s- to p-polarization, while using 1 µm-thin targets. The second method focused on the enhancement of the preplasma formation by reducing the temporal contrast on the nanosecond scale to 10^{-6}, and increasing the target thickness

to 10 µm. The latter method showed no improvement compared to the standard setup with high contrast, s-polarization and a target thickness of 1 µm. When the laser polarization has been changed, the maximum proton energy has been increased by ≈ 60 % up to 71 MeV, while increasing the amount of particles by ≈ 57 % up to 3.2×10^{12} protons above 10 MeV.

During the second campaign, the on-target intensity was increased by improving the focal spot distribution, which has been done by exchanging the last focusing optics from a copper parabola to a glass parabola. This lead to an improvement of the laser intensity by almost a factor of 3, of up to 8×10^{20} W/cm^2. Despite this increase in intensity, the resulting maximum proton energy was only enhanced by a small amount. This was backed up by the fact that the recorded maximum proton energies were much better represented by a scaling of the peak power instead of a scaling with the intensity. The found scaling also matched the measurements of the previous experiment with a p-polarized laser pulse, despite the completely different incident angles and therefore reduced laser intensity. During these campaigns a new record for protons accelerated with PHELIX could be achieved with a maximum energy of $90 \pm^{3}_{0}$ MeV.

7 Future prospects

There are several possibilities to extend this work on the correlation between preplasma properties and the spectral behavior of the reflected laser pulse.
For example, the precise influence of an initially non-zero temporal phase on the instantaneous wavelength after the interaction can be monitored. This might help to understand how an altered phase influences the measurement in experimental conditions. This can be done in combination to a temporally resolved measurement of the full-aperture incoming beam to use this measurement as an input for the calculation of the HB velocity.
In addition, the dimensionality of the interaction has to be taken into account within the analytical solution for the HB velocity, which could also be supported by three-dimensional PIC simulations.
However, the computationally-expensive 3-D simulation is accompanied by the need to reduce the amount of data and computation time, which could be achieved by strongly reducing the simulation box and picking off the EM field at the boundaries for each time step. A further possibility to reduce the computational resources time is offered by a current project in which I am involved. It deals with the on-line data reduction of the numerical simulation, which is currently developed for the PIC code EPOCH and later tested at the Kronos cluster of GSI.
These improvements might lead to the possibility of computing the presented simulation scheme in three dimensions.
The experimental realization of the presented method can also be improved in future work. Especially, the time-resolved diagnostics can be enhanced by utilizing a third-order non-linear effect. This would enable the measurement of the spectral shift at the beginning of the pulse by comparing the incoming and reflected pulses without ambiguity.
Additionally, the dynamic range of the FROG device could be increased by acquiring a saturated and unsaturated FROG trace at the same time. The combination of both measurements would increase temporal and spectral range that can be reconstructed.
This could be used to resolve the low intensity regime that contains most of the information about the preplasma properties.
To further validate the presented measurement method and to study the limits of observable properties, a designated prepulse can be used to create preplasmas of different extent and expansion velocity.
To ensure that the preplasma expansion only occurs because of the introduced prepulse, the influence of the rising slope of the laser pulse on the preplasma generation must be negligible. Even though it was shown that the implementation of a double plasma mirror is able to strongly reduce the rising slope, the corresponding laser-energy losses are relatively high. This shows that a improvement of the temporal contrast is absolutely

necessary to avoid the use of a PM. A possibility to ensure a similar rising slope might be given by an upgrade of the pulse stretcher, which currently seems to be the major reason for an imperfect rising slope [80].
The presented method might also be applied to the study of RPA, provided that a time-resolved measurement method for circularly polarized light is available. The reflection spectroscopy could therefore be used to determine if the necessary regime of an unperturbed and cold plasma is present in experimental conditions.

References

[1] A. W. Ehler. High-energy ions from a CO_2 laser-produced plasma. J. Appl. Phys., 46(6):2464–2467, 1975.

[2] D. C. Slater. Pinhole imaging of fast ions from laser-produced plasmas. Appl. Phys. Lett., 31(3):196–198, 1977.

[3] R. Decoste and B. H. Ripin. High-energy ion expansion in laser-plasma interactions. Phys. Rev. Lett., 40:34–37, 1978.

[4] E. L. Clark, K. Krushelnick, J. R. Davies, M. Zepf, M. Tatarakis, F. N. Beg, A. Machacek, P. A. Norreys, M. I. K. Santala, I. Watts, and A. E. Dangor. Measurements of energetic proton transport through magnetized plasma from intense laser interactions with solids. Phys. Rev. Lett., 84:670–673, 2000.

[5] R. A. Snavely, M. H. Key, S. P. Hatchett, T. E. Cowan, M. Roth, T. W. Phillips, M. A. Stoyer, E. A. Henry, T. C. Sangster, M. S. Singh, S. C. Wilks, A. MacKinnon, A. Offenberger, D. M. Pennington, K. Yasuike, A. B. Langdon, B. F. Lasinski, J. Johnson, M. D. Perry, and E. M. Campbell. Intense high-energy proton beams from petawatt-laser irradiation of solids. Phys. Rev. Lett., 85(14):2945, 2000.

[6] J. Schreiber, F. Bell, F. Grüner, U. Schramm, M. Geissler, M. Schürer, S. Ter-Avetisyan, B. M. Hegelich, J. Cobble, E. Brambrik, J. Fuchs, P. Audebert, and D. Habs. Analytical model for ion acceleration by high-intensity laser pulses. Phys. Rev. Lett., 97(4):045005, 2006.

[7] L. Yin, B. J. Albright, B. M. Hegelich, K. J. Bowers, K. A. Flippo, T. J. T. Kwan, and J. C. Fernández. Monoenergetic and GeV ion acceleration from the laser breakout afterburner using ultrathin targets. Phys. Plasmas, 14(5):056706, 2007.

[8] H. Daido, M. Nishiuchi, and A. S. Pirozhkov. Review of laser-driven ion sources and their applications. Rep. Prog. Phys., 75(5):056401, 2012.

[9] J. Schreiber, P. R. Bolton, and K. Parodi. Invited review article:“Hands-on” laser-driven ion acceleration: A primer for laser-driven source development and potential applications. Rev. Sci. Instrum., 87(7):071101, 2016.

[10] A. J. Mackinnon, M. Borghesi, S. Hatchett, M. H. Key, P. K. Patel, H. Campbell, A. Schiavi, R. Snavely, S. C. Wilks, and O. Willi. Effect of plasma scale length on multi-MeV proton production by intense laser pulses. Phys. Rev. Lett., 86:1769–1772, 2001.

[11] M. L. Zhou, J. H. Bin, D. Haffa, X. Q. Yan, and J. Schreiber. The impact of femtosecond pre-pulses on nanometer thin foils for laser-ion acceleration. Plasma Phys. Control. Fusion, 59(5):055020, 2017.

[12] F. Wagner, C. P. João, J. Fils, T. Gottschall, J. Hein, J. Körner, J. Limpert, M. Roth, T. Stöhlker, and V. Bagnoud. Temporal contrast control at the PHELIX petawatt laser facility by means of tunable sub-picosecond optical parametric amplification. Appl. Phys. B, 116(2):429–435, 2014.

[13] S. Feister, J. A. Nees, J. T. Morrison, K. D. Frische, C. Orban, E. A. Chowdhury, and W. M. Roquemore. A novel femtosecond-gated, high-resolution, frequency-shifted shearing interferometry technique for probing pre-plasma expansion in ultra-intense laser experiments. Rev. Sci. Instrum., 85(11):11D602, 2014.

[14] J. P. Geindre, P. Audebert, A. Rousse, F. Falliès, J. C. Gauthier, A. Mysyrowicz, A. Dos Santos, G. Hamoniaux, and A. Antonetti. Frequency-domain interferometer for measuring the phase and amplitude of a femtosecond pulse probing a laser-produced plasma. Opt. Lett., 19(23):1997–1999, 1994.

[15] S. Kahaly, S. Monchocé, H. Vincenti, T. Dzelzainis, B. Dromey, M. Zepf, Ph. Martin, and F. Quéré. Direct observation of density-gradient effects in harmonic generation from plasma mirrors. Phys. Rev. Lett., 110:175001, 2013.

[16] B. H. Ripin, J. M. McMahon, E. A. McLean, W. M. Manheimer, and J. A. Stamper. Time-resolved laser-plasma backscatter studies. Phys. Rev. Lett., 33:634–637, 1974.

[17] M. Zepf, M. Castro-Colin, D. Chambers, S. G. Preston, J. S. Wark, J. Zhang, C. N. Danson, D. Neely, P. A. Norreys, A. E. Dangor, A. Dyson, P. Lee, A. P. Fews, P. Gibbon, S. Moustaizis, and M. H. Key. Measurements of the hole boring velocity from doppler shifted harmonic emission from solid targets. Phys. Plasmas, 3(9):3242–3244, 1996.

[18] R. Sauerbrey. Acceleration in femtosecond laser-produced plasmas. Phys. Plasmas, 3(12):4712–4716, 1996.

[19] R. Häßner, W. Theobald, S. Niedermeier, K. Michelmann, T. Feurer, H. Schillinger, and R. Sauerbrey. Measurement of acceleration in femtosecond laser-plasmas. AIP Conf. Proc., 426(1):213–220, 1998.

[20] R. J. Kingham, P. Gibbon, W. Theobald, L. Veisz, and R. Sauerbrey. Phase modulation of intense ultrashort laser pulses reflected from steep, dense plasmas. Phys. Rev. Lett., 86:810–813, 2001.

[21] S. Palaniyappan, B. M. Hegelich, H.-C. Wu, D. Jung, D. C. Gautier, L. Yin, B. J. Albright, R. P. Johnson, T. Shimada, S. Letzring, D. T. Offermann, J. Ren, C. Huang, R. Hörlein, B. Dromey, J. C. Fernandez, and R. C. Shah. Dynamics of relativistic transparency and optical shuttering in expanding overdense plasmas. Nature Phys., 8:763–769, 2012.

[22] V. Bagnoud, B. Aurand, A. Blazevic, S. Borneis, C. Bruske, B. Ecker, U. Eisenbarth, J. Fils, A. Frank, E. Gaul, et al. Commissioning and early experiments of the PHELIX facility. Appl. Phys. B, 100(1):137–150, 2010.

[23] F. Wagner, J. Hornung, C. Schmidt, M. Eckhardt, M. Roth, T. Stöhlker, and V. Bagnoud. Backreflection diagnostics for ultra-intense laser plasma experiments based on frequency resolved optical gating. Rev. Sci. Instrum., 88(2):023503, 2017.

[24] F. F. Chen. Introduction to Plasma Physics and Controlled Fusion. Springer International Publishing, 2016.

[25] S. Eliezer. The interaction of high-power lasers with plasmas. CRC Press, 2002.

[26] S. C. Wilks. Simulations of ultraintense laser–plasma interactions. Phys. Fluids B: Plasma Physics, 5(7):2603–2608, 1993.

[27] P. Gibbon. Short Pulse Laser Interactions with Matter: An Introduction. Imperial College Press, London, 2005.

[28] G. Cristoforetti, A. De Giacomo, M. Dell'Aglio, S. Legnaioli, E. Tognoni, V. Palleschi, and N. Omenetto. Local thermodynamic equilibrium in laser-induced breakdown spectroscopy: Beyond the McWhirter criterion. Spectrochim. Acta B, 65(1):86 – 95, 2010.

[29] http://physics.nist.gov/PhysRefData/ASD/ionEnergy.html. The ionization energies for cesium can extracted from the NIST database - Accessed: 12/2020.

[30] P. Mulser and D. Bauer. High Power Laser-Matter Interaction. Springer Tracts in Modern Physics, Springer, 2010.

[31] P. Kaw and J. Dawson. Relativistic nonlinear propagation of laser beams in cold overdense plasmas. Phys. Fluids, 13:472–481, 1970.

[32] S. C. Wilks and W. L. Kruer. Absorption of ultrashort, ultra-intense laser light by solids and overdense plasmas. IEEE J. Quantum Electron., 33(11):1954–1968, 1997.

[33] J. P. Freidberg, R. W. Mitchell, R. L. Morse, and L. I. Rudsinski. Resonant absorption of laser light by plasma targets. Phys. Rev. Lett., 28:795–799, 1972.

[34] F. Brunel. Not-so-resonant, resonant absorption. Phys. Rev. Lett., 59:52–55, 1987.

[35] P. Gibbon and A. R. Bell. Collisionless absorption in sharp-edged plasmas. Phys. Rev. Lett., 68:1535–1538, 1992.

[36] W. L. Kruer and K. Estabrook. Laser light absorption due to self-generated magnetic fields. Phys. Fluids, 20(10):1688–1691, 1977.

[37] S. C. Wilks, W. L. Kruer, M. Tabak, and A. B. Langdon. Absorption of ultra-intense laser pulses. Phys. Rev. Lett., 69:1383–1386, 1992.

[38] A. P. L. Robinson, P. Gibbon, M. Zepf, S. Kar, R. G. Evans, and C. Bellei. Relativistically correct hole-boring and ion acceleration by circularly polarized laser pulses. Plasma Phys. Control. Fusion, 51(2):024004, 2009.

[39] Y. Ping, A. J. Kemp, L. Divol, M. H. Key, P. K. Patel, K. U. Akli, F. N. Beg, S. Chawla, C. D. Chen, R. R. Freeman, D. Hey, D. P. Higginson, L. C. Jarrott, G. E. Kemp, A. Link, H. S. McLean, H. Sawada, R. B. Stephens, D. Turnbull, B. Westover, and S. C. Wilks. Dynamics of relativistic laser-plasma interaction on solid targets. Phys. Rev. Lett., 109:145006, 2012.

[40] N. Iwata, S. Kojima, Y. Sentoku, M. Hata, and K. Mima. Plasma density limits for hole boring by intense laser pulses. Nat. Commun., 9(623), 2018.

[41] A. Gjurchinovski. The doppler effect from a uniformly moving mirror. Eur. J. Phys., 26(4):643–646, 2005.

[42] M. Roth, T. E. Cowan, M. H. Key, S. P. Hatchett, C. Brown, W. Fountain, J. Johnson, D. M. Pennington, R. A. Snavely, S. C. Wilks, K. Yasuike, H. Ruhl, F. Pegoraro, S. V. Bulanov, E. M. Campbell, M. D. Perry, and H. Powell. Fast ignition by intense laser-accelerated proton beams. Phys. Rev. Lett., 86:436–439, 2001.

[43] S. V. Bulanov, T. Zh. Esirkepov, V. S. Khoroshkov, A. V. Kuznetsov, and F. Pegoraro. Oncological hadrontherapy with laser ion accelerators. Phys. Lett. A, 299(2):240–247, 2002.

[44] S. S. Bulanov, A. Brantov, V. Y. Bychenkov, V. Chvykov, G. Kalinchenko, T. Matsuoka, P. Rousseau, S. Reed, V. Yanovsky, K. Krushelnick, D. W. Litzenberg, and A. Maksimchuk. Accelerating protons to therapeutic energies with ultraintense, ultraclean, and ultrashort laser pulses. Med. Phys., 35:1770–1776, 2008.

[45] P. Boller, A. Zylstra, P. Neumayer, L. Bernstein, C. Brabetz, J. Despotopulos, J. Glorius, J. Hellmund, E. A. Henry, J. Hornung, J. Jeet, J. Khuyagbaatar, L. Lens, S. Roeder,

T. Stoehlker, A. Yakushev, Y. A. Litvinov, D. Shaughnessy, V. Bagnoud, T. Kuehl, and D. H. G. Schneider. First on-line detection of radioactive fission isotopes produced by laser-accelerated protons. Sci. Rep., 10:17183, 2020.

[46] D. Doria, M.O. Cernaianu, P. Ghenuche, D. Stutman, K.A. Tanaka, C. Ticos, and C.A. Ur. Overview of ELI-NP status and laser commissioning experiments with 1 PW and 10 PW class-lasers. J. Instrum., 15(09):C09053–C09053, 2020.

[47] M. Borghesi, J. Fuchs, S. V. Bulanov, A. J. MacKinnon, P. K. Patel, and M. Roth. Fast ion generation by high-intensity laser irradiation of solid targets and applications. Fusion Sci. Technol., 49(3):412–439, 2006.

[48] M. Passoni, V. T. Tikhonchuk, M. Lontano, and V. Yu. Bychenkov. Charge separation effects in solid targets and ion acceleration with a two-temperature electron distribution. Phys. Rev. E, 69:026411, 2004.

[49] S. C. Wilks, A. B. Langdon, T. E. Cowan, M. Roth, M. Singh, S. Hatchett, M. H. Key, D. Pennington, A. MacKinnon, and R. A. Snavely. Energetic proton generation in ultra-intense laser-solid interactions. Phys. Plasmas, 8(2):542–549, 2001.

[50] P. Mora. Plasma expansion into a vacuum. Phys. Rev. Lett., 90(18):185002, 2003.

[51] J. Fuchs, P. Antici, E. d'Humières, E. Lefebvre, M. Borghesi, E. Brambrink, C. A. Cecchetti, M. Kaluza, V. Malka, M. Manclossi, et al. Laser-driven proton scaling laws and new paths towards energy increase. Nat. Phys., 2(1):48, 2006.

[52] J. Schreiber, F. Bell, F. Grüner, U. Schramm, M. Geissler, M. Schnürer, S. Ter-Avetisyan, B. M. Hegelich, J. Cobble, E. Brambrink, J. Fuchs, P. Audebert, and D. Habs. Analytical model for ion acceleration by high-intensity laser pulses. Phys. Rev. Lett., 97:045005, 2006.

[53] K. Zeil, S. D. Kraft, S. Bock, M. Bussmann, T. E. Cowan, T. Kluge, J. Metzkes, T. Richter, R. Sauerbrey, and U. Schramm. The scaling of proton energies in ultrashort pulse laser plasma acceleration. New J. Phys., 12(4):045015, 2010.

[54] D. Batani, R. Jafer, M. Veltcheva, R. Dezulian, O. Lundh, F. Lindau, A. Persson, K. Osvay, C.-G. Wahlström, D. C. Carroll, P. McKenna, A. Flacco, and V. Malka. Effects of laser prepulses on laser-induced proton generation. New J. Phys., 12(4):045018, 2010.

[55] R. Nuter, L. Gremillet, P. Combis, M. Drouin, E. Lefebvre, A. Flacco, and V. Malka. Influence of a preplasma on electron heating and proton acceleration in ultraintense laser-foil interaction. J. Appl. Phys., 104(10):103307, 2008.

[56] D. Neely, P. Foster, A. Robinson, F. Lindau, O. Lundh, A. Persson, C.-G. Wahlström, and P. McKenna. Enhanced proton beams from ultrathin targets driven by high contrast laser pulses. Appl. Phys. Lett., 89(2):021502, 2006.

[57] M. Kaluza, J. Schreiber, M. I. K. Santala, G. D. Tsakiris, K. Eidmann, J. Meyer-ter Vehn, and K. J. Witte. Influence of the laser prepulse on proton acceleration in thin-foil experiments. Phys. Rev. Lett., 93:045003, 2004.

[58] A. J. Mackinnon, Y. Sentoku, P. K. Patel, D. W. Price, S. Hatchett, M. H. Key, C. Andersen, R. Snavely, and R. R. Freeman. Enhancement of proton acceleration by hot-electron recirculation in thin foils irradiated by ultraintense laser pulses. Phys. Rev. Lett., 88:215006, 2002.

[59] L. Yin, B. J. Albright, B. M. Hegelich, and J. C. Fernández. GeV laser ion acceleration from ultrathin targets: The laser break-out afterburner. Laser Part. Beams, 24(2):291–298, 2006.

[60] A. Henig, D. Kiefer, K. Markey, D. C. Gautier, K. A. Flippo, S. Letzring, R. P. Johnson, T. Shimada, L. Yin, B. J. Albright, K. J. Bowers, J. C. Fernández, S. G. Rykovanov, H.-C. Wu, M. Zepf, D. Jung, V. Kh. Liechtenstein, J. Schreiber, D. Habs, and B. M. Hegelich. Enhanced laser-driven ion acceleration in the relativistic transparency regime. Phys. Rev. Lett., 103:045002, 2009.

[61] A. P. L. Robinson, M. Zepf, S. Kar, R. G. Evans, and C. Bellei. Radiation pressure acceleration of thin foils with circularly polarized laser pulses. New J. Phys., 10(1):013021, 2008.

[62] A. A. Sahai, F. S. Tsung, A. R. Tableman, W. B. Mori, and T. C. Katsouleas. Relativistically induced transparency acceleration of light ions by an ultrashort laser pulse interacting with a heavy-ion-plasma density gradient. Phys. Rev. E, 88:043105, 2013.

[63] F. Wagner. Kontrolle des zeitlichen Kontrastes am Lasersystem PHELIX. PhD thesis, TU Darmstadt, 2014.

[64] O. Buneman. Dissipation of currents in ionized media. Phys. Rev., 115:503–517, 1959.

[65] B. J. Albright, L. Yin, Kevin J. Bowers, B. M. Hegelich, K. A. Flippo, T. J. T. Kwan, and J. C. Fernández. Relativistic Buneman instability in the laser breakout afterburner. Phys. Plasmas, 14(9):094502, 2007.

[66] F. Wagner, S. Bedacht, V. Bagnoud, O. Deppert, S. Geschwind, R. Jaeger, A. Ortner, A. Tebartz, B. Zielbauer, D. H. H. Hoffmann, and M. Roth. Simultaneous observation of angularly separated laser-driven proton beams accelerated via two different mechanisms. Phys. Plasmas, 22(6):063110, 2015.

[67] A. Higginson, R. J. Gray, R. J. Dance, S. D. R. Williamson, N. M. H. Butler, R. Wilson, R. Capdessus, C. Armstrong, J. S. Green, S. J. Hawkes, P. Martin, W. Q. Wei, S. R. Mirfayzi, X. H. Yuan, M. Borghesi, R. J. Clarke, D. Neely, and P. McKenna. Near-100 MeV protons via a laser-driven transparency-enhanced hybrid acceleration scheme. Nat. Commun., 9:724, 2018.

[68] B. M. Hegelich, D. Jung, B. J. Albright, M. Cheung, B. Dromey, D. C. Gautier, C. Hamilton, S. Letzring, R. Munchhausen, S. Palaniyappan, R. Shah, H. C. Wu, L. Yin, and J. C. Fernández. 160 MeV laser-accelerated protons from CH_2 nano-targets for proton cancer therapy. arXiv, 1310.8650[physics.plasm-ph], 2013.

[69] O. Klimo, J. Psikal, J. Limpouch, and V. T. Tikhonchuk. Monoenergetic ion beams from ultrathin foils irradiated by ultrahigh-contrast circularly polarized laser pulses. Phys. Rev. ST Accel. Beams, 11:031301, 2008.

[70] I. J. Kim, Ki. H. Pae, Il. W. Choi, C.-L. Lee, H. T. Kim, H. Singhal, J. H. Sung, S. K. Lee, H. W. Lee, P. V. Nickles, T. M. Jeong, C. M. Kim, and C. H. Nam. Radiation pressure acceleration of protons to 93 Mev with circularly polarized petawatt laser pulses. Phys. Plasmas, 23(7):070701, 2016.

[71] T. Esirkepov, M. Borghesi, S. V. Bulanov, G. Mourou, and T. Tajima. Highly efficient relativistic-ion generation in the laser-piston regime. Phys. Rev. Lett., 92:175003, 2004.

[72] A. P. L. Robinson, D.-H. Kwon, and K. Lancaster. Hole-boring radiation pressure acceleration with two ion species. Plasma Phys. Control. Fusion, 51(9):095006, 2009.

[73] B. Qiao, M. Zepf, M. Borghesi, B. Dromey, M. Geissler, A. Karmakar, and P. Gibbon. Radiation-pressure acceleration of ion beams from nanofoil targets: The leaky lightsail regime. Phys. Rev. Lett., 105:155002, 2010.

[74] X. Q. Yan, C. Lin, Z. M. Sheng, Z. Y. Guo, B. C. Liu, Y. R. Lu, J. X. Fang, and J. E. Chen. Generating high-current monoenergetic proton beams by a circularlypolarized laser pulse in the phase-stableacceleration regime. Phys. Rev. Lett., 100:135003, 2008.

[75] G. Lapenta, J. U. Brackbill, and P. Ricci. Kinetic approach to microscopic-macroscopic coupling in space and laboratory plasmas. Phys. Plasmas, 13(5):055904, 2006.

[76] T. D. Arber, K. Bennett, C. S. Brady, A. Lawrence-Douglas, M. G. Ramsay, N. J. Sircombe, P. Gillies, R. G. Evans, H. Schmitz, A. R. Bell, and C. P. Ridgers. Contemporary particle-in-cell approach to laser-plasma modelling. Plas. Phys. Contr. Fus., 57(11):1–26, 2015.

[77] D. Strickland and G. Mourou. Compression of amplified chirped optical pulses. Opt. Commun., 55(6):447–449, 1985.

[78] V. A. Schanz, C. Brabetz, D. J. Posor, D. Reemts, M. Roth, and V. Bagnoud. High dynamic range, large temporal domain laser pulse measurement. Appl. Phys. B, 125(4):61, 2019.

[79] N. V. Didenko, A. V. Konyashchenko, A. P. Lutsenko, and S. Yu. Tenyakov. Contrast degradation in a chirped-pulse amplifier due to generation of prepulses by postpulses. Opt. Express, 16(5):3178–3190, 2008.

[80] V. A. Schanz, M. Roth, and V. Bagnoud. Picosecond contrast degradation by surface imperfections in chirped-pulse-amplification stretchers. J. Opt. Soc. Am. A, 36(10):1735–1742, 2019.

[81] V. Zamfir, K. Tanaka, and C. Ur. Extreme light infrastructure nuclear physics (eli-np). Europhys. News, 50(2):23–25, 2019.

[82] T. Zh. Esirkepov, J. K. Koga, A. Sunahara, T. Morita, M. Nishikino, K. Kageyama, H. Nagatomo, K. Nishihara, A. Sagisaka, H. Kotaki, T. Nakamura, Y. Fukuda, H. Okada, A. S. Pirozhkov, A. Yogo, M. Nishiuchi, H. Kiriyama, K. Kondo, M. Kando, and S. V. Bulanov. Prepulse and amplified spontaneous emission effects on the interaction of a petawatt class laser with thin solid targets. Nucl. Instrum. Meth. A, 745:150 – 163, 2014.

[83] U. Samir, K. H. Wright, and N. H. Stone. The expansion of a plasma into a vacuum: Basic phenomena and processes and applications to space plasma physics. Rev. Geophys., 21(7):1631–1646, 1983.

[84] V. Bagnoud, J. Hornung, T. Schlegel, B. Zielbauer, C. Brabetz, M. Roth, P. Hilz, M. Haug, J. Schreiber, and F. Wagner. Studying the dynamics of relativistic laser-plasma interaction on thin foils by means of fourier-transform spectral interferometry. Phys. Rev. Lett., 118:255003, 2017.

[85] V. L. J. Phung, M. Kim, J. Kim, H. S. Uhm, and H. Suk. Characteristics of the preplasma formation using an uncompressed picosecond-long laser pulse with a large spot size on Al and mylar targets. Curr. Appl. Phys., 19(7):829 – 834, 2019.

[86] K. Adumi, K. A. Tanaka, T. Matsuoka, T. Kurahashi, T. Yabuuchi, Y. Kitagawa, R. Kodama, K. Sawai, K. Suzuki, K. Okabe, T. Sera, T. Norimatsu, and Y. Izawa. Characterization of preplasma produced by an ultrahigh intensity laser system. Phys. Plasmas, 11(8):3721–3725, 2004.

[87] K. L. Lancaster, J. Pasley, J. S. Green, D. Batani, S. Baton, R. G. Evans, L. Gizzi, R. Heathcote, C. Hernandez Gomez, M. Koenig, P. Koester, A. Morace, I. Musgrave, P. A. Norreys, F. Perez, J. N. Waugh, and N. C. Woolsey. Temperature profiles derived from transverse optical shadowgraphy in ultraintense laser plasma interactions at $6x10^{20}$ Wcm^{-2}. Phys. Plasmas, 16(5):056707, 2009.

[88] S. Patankar, E. T. Gumbrell, T. S. Robinson, H. F. Lowe, S. Giltrap, C. J. Price, N. H. Stuart, P. Kemshall, J. Fyrth, J. Luis, J. W. Skidmore, and R. A. Smith. Multiwavelength interferometry system for the orion laser facility. Appl. Opt., 54(36):10592–10598, 2015.

[89] R. W. Boyd. Nonlinear Optics, Second Edition. Academic Press, 2nd Edition, 2003.

[90] I. Watts, M. Zepf, E. L. Clark, M. Tatarakis, K. Krushelnick, A. E. Dangor, R. Allott, R. J. Clarke, D. Neely, and P. A. Norreys. Measurements of relativistic self-phase-modulation in plasma. Phys. Rev. E, 66:036409, 2002.

[91] F. Pedrotti, L. Pedrotti, W. Bausch, and H. Schmidt. Optik für Ingenieure, Grundlagen, Third Edition. Springer, 3rd Edition, 2005.

[92] T. Claasen and W. Mecklenbrauker. The Wigner distribution - A tool for time-frequency signal analysis. Philips Res. Rep., 35:217033, 1980.

[93] C. Thaury and F. Quéré. High-order harmonic and attosecond pulse generation on plasma mirrors: Basic mechanisms. J. Phys. B-At. Mol. Opt., 43(21):213001, 2010.

[94] A. J. Kemp, Y. Sentoku, and M. Tabak. Hot-electron energy coupling in ultraintense laser-matter interaction. Phys. Rev. E, 79:066406, 2009.

[95] A. Giulietti and D. Giulietti. Self-phase modulation in various regimes of intense laser–plasma interactions. J. Plasma Phys., 81(6):495810608, 2015.

[96] J. Hornung, Y. Zobus, P. Boller, C. Brabetz, U. Eisenbarth, T. Kühl, Zs. Major, J. B. Ohland, M. Zepf, B. Zielbauer, and et al. Enhancement of the laser-driven proton source at PHELIX. High Power Laser Sci. Eng., 8:e24, 2020.

[97] B. Dromey, S. Kar, M. Zepf, and P. Foster. The plasma mirror — A subpicosecond optical switch for ultrahigh power lasers. Rev. Sci. Instrum., 75(3):645–649, 2004.

[98] Ch. Ziener, P. S. Foster, E. J. Divall, C. J. Hooker, M. H. R. Hutchinson, A. J. Langley, and D. Neely. Specular reflectivity of plasma mirrors as a function of intensity, pulse duration, and angle of incidence. J. Appl. Phys, 93(1):768–770, 2003.

[99] D. J. Kane and R. Trebino. Single-shot measurement of the intensity and phase of an arbitrary ultrashort pulse by using frequency-resolved optical gating. Opt. Lett., 18(10):823–825, 1993.

[100] J. Hornung. Zeitaufgelöste Messung der Wechselwirkung von ultra-intensiven Laserpulsen mit sub-mikrometer dicken Targets. Masterarbeit, TU Darmstadt, 2017.

[101] R. Bitter, T. Mohiuddin, and M. Nawrocki. LabVIEW: Advanced programming techniques. Crc Press, 2006.

[102] S. Röder. Design of a SPIDER for time-resolved plasma characterization. Masterarbeit, TU Darmstadt, 2020.

[103] C. Iaconis and I. A. Walmsley. Spectral phase interferometry for direct electric-field reconstruction of ultrashort optical pulses. Opt. Lett., 23(10):792–794, 1998.

[104] David J. Stark, Lin Yin, Brian J. Albright, William Nystrom, and Robert Bird. A detailed examination of laser-ion acceleration mechanisms in the relativistic transparency regime using tracers. Phys. Plasmas, 25(4):043114, 2018.

[105] N. Schroeter. Development and calibration of a high-dispersive Thomson parabola for laser-driven ion beams. Masterarbeit, Technische Universität Darmstadt, 2017.

[106] D. Bauer and P. Mulser. Vacuum heating versus skin layer absorption of intense femtosecond laser pulses. Phys. Plasmas, 14:023301, 2007.

[107] F. Wagner, V. Bagnoud, C. Brabetz, T. Stoehlker, S. Bedacht, O. Deppert, M. Roth, and A. Tebartz. Towards 100 MeV maximum energy for laser-accelerated proton beams. Bull. Am. Phys. Soc., 60, 2015.

[108] L. Robson, P. T. Simpson, R. J. Clarke, K. W. D. Ledingham, F. Lindau, O. Lundh, T. McCanny, P. Mora, D. Neely, C.-G. Wahlström, M. Zepf, and P. McKenna. Scaling of proton acceleration driven by petawatt-laser-plasma interactions. Nature Phys., 3:58–62, 2007.

List of abbreviations

PIC particle-in-cell

PHELIX Petawatt High-Energy Laser for Heavy-Ion eXperiments

EM electromagnetic

eV electron Volt

MPI multi-photon ionization

HB holeboring

TNSA "Target-Normal Sheath Acceleration"

RITA "Relativistically Induced Transparency Acceleration"

BOA "Breakout Afterburner"

RPA "Radiation Pressure Acceleration"

CPA chirped-pulse amplification

ASE amplified spontaneous emission

FWHM full width at half maximum

SPM self-phase modulation

WVD Wigner-Ville distribution

EMP electromagnetic pulse

PM plasma mirror

SHG second-harmonic generation

RCF radiochromic film

PTV peak to valley

RMS root mean square

LPI laser-plasma interaction

FROG "Frequency-Resolved Optical Gating"

SPIDER "Spectral Phase Interferometry for Direct Electric-field Reconstruction"

List of publications

[1] F. Wagner, **J. Hornung**, C. Schmidt, M. Eckhardt, M. Roth, T. Stöhlker and V. Bagnoud, Backreflection diagnostics for ultra-intense laser plasma experiments based on frequency resolved optical gating, Rev. Sci. Instrum. 88, 023503, 2017

[2] V. Bagnoud, **J. Hornung**, T. Schlegel, B. Zielbauer, C. Brabetz, M. Roth, P. Hilz, M. Haug, J. Schreiber and F. Wagner, Studying the Dynamics of Relativistic Laser-Plasma Interaction on Thin Foils by Means of Fourier-Transform Spectral Interferometry, Phys. Rev. Lett. 118, 2017

[3] A. Kleinschmidt, V. Bagnoud, O. Deppert, A. Favalli, S. Frydrych, **J. Hornung**, D. Jahn, G. Schaumann, A. Tebartz, F. Wagner, G. Wurden, B. Zielbauer and M. Roth, Intense, directed neutron beams from a laser-driven neutron source at PHELIX, Phys. Plasmas 25, 053101, 2018

[4] V. Bagnoud, **J. Hornung**, M. Afshari, U. Eisenbarth, C. Brabetz, Zs. Major and B. Zielbauer, Implementation of a phase plate for the generation of homogeneous focal-spot intensity distributions at the high-energy short-pulse laser facility PHELIX, High Power Laser Sci. Eng. 7, 2019

[5] M. Afshari , **J. Hornung** , A. Kleinschmidt, P. Neumayer, D. Bertini and V. Bagnoud, Proton acceleration via the TNSA mechanism using a smoothed laser focus, AIP Adv. 10, 035023, 2020

[6] **J. Hornung**, Y. Zobus, P. Boller, C. Brabetz, U. Eisenbarth, T. Kühl, Zs. Major, J. B. Ohland, M. Zepf, B. Zielbauer and V. Bagnoud, Enhancement of the laser-driven proton source at PHELIX, High Power Laser Sci. Eng. 8, E24, 2020

[7] P. Boller, A. Zylstra, P. Neumayer, L. Bernstein, C. Brabetz, J. Despotopulos, J. Glorius, J. Hellmund, E. A. Henry, **J. Hornung**, J. Jeet, J. Khuyagbaatar, L. Lens, S. Roeder, T. Stoehlker, A. Yakushev, Y. A. Litvinov, D. Shaughnessy, V. Bagnoud, T. Kuehl and D. H. G. Schneider, First on-line detection of radioactive fission isotopes produced by laser-accelerated protons, Sci. Rep. 10, 17183, 2020

[8] M. Zimmer, V. Bagnoud, S. Scheuren, **J. Hornung**, T. Ebert, G. Schaumann, C. Rödel, M. Roth, Analysis of Laser-Proton Acceleration Experiments for the Development of Empirical Scaling Laws, submitted to Phys. Rev. E

[9] **J. Hornung**, Y. Zobus, S. Röder, A. Kleinschmidt, D. Bertini, M. Zepf and V. Bagnoud, Characterization of the plasma scale length using time-resolved reflection spectroscopy, in preparation

Appendix

Convergence test for PIC simulations

A convergence test for the one-dimensional scenario of the simulation presented in Sec. 3.3.2. The test has been done for the lowest temperature of 10 eV and a laser intensity of 10^{20} W/cm^2.
The simulation has been conducted for different grid resolutions, ranging from 24 nm to 3 nm and different number of particles per cell (ppc). In the following, a denotation of "12nmN8" refers to a simulation with a resolution of 12 nm and 8 ppc.
Since the conducted simulations focused on the reflected pulse, the resulting laser pulse intensity and instantaneous frequency were used as the physical quantity that has to converge. An example for the calculation of the intensity difference Δ between two simulations is given by

$$\Delta = |I_{24nmN8} - I_{12nmN4}|^2, \tag{52}$$

where the simulation with the higher resolution (12nmN4) has been reduced to the same number of cells as the simulation with the lower resolution (24nmN8). This is done by averaging the values of every two cells. The resulting convergence curves are shown in Fig. A.1, for the instantaneous frequency, and Fig. A.2 for the pulse intensity. The horizontal axis shows the parameter of the simulations, whereas the first entry $^{12nmN4}_{24nmN8}$ corresponds to Eq. 52.

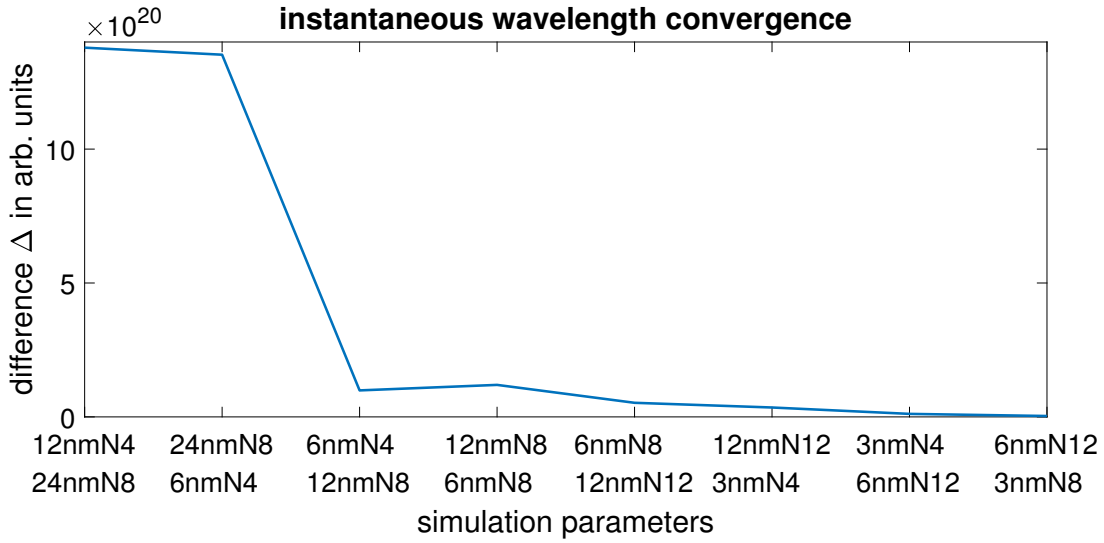

Figure A.1: Convergence of the instantaneous frequency.

It is visible that the difference between the simulations does only slowly change after the simulation with a resolution of 6 nm and 4 ppc, or 12 nm and 8 ppc. Therefore a resolution

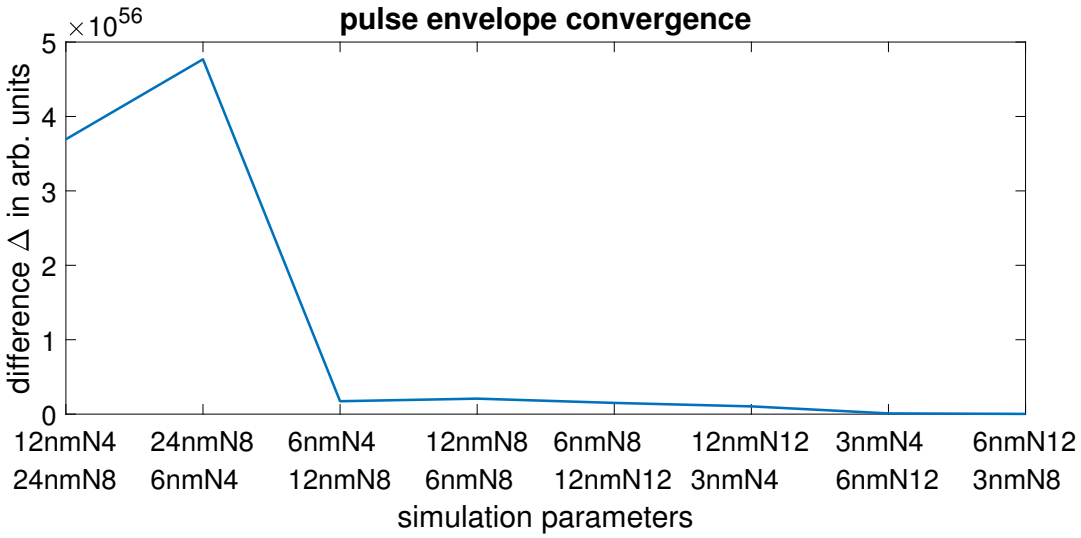

Figure A.2: Convergence of the pulse intensity.

of 12 nm seems to be sufficient when the number of cells is accordingly high.

Intensity dependence of the holeboring acceleration

The holeboring velocity $v_f(t)$ can be connected to the laser intensity I(t) by [40].

$$(1+R)\frac{I(t)}{c} = 2n_i M_i v_f(t)^2, \tag{53}$$

with the speed of light c, the reflectivity of the plasma R, the number of ions n_i and the corresponding mass M_i. By resolving this for the front velocity with the ion density at the critical density $n_i = \gamma n_c/Z$, one obtains:

$$v_f(t) = \sqrt{\frac{Z(1+R)I(t)}{2cn_c M_i}}. \tag{54}$$

To obtain the acceleration of this holeboring front $a_f(t)$, the temporal derivative of v_f is calculated:

$$a_f(t) = \frac{d}{dt}v_f(t) = \sqrt{\frac{Z(1+R)}{2cM_i n_c}}\frac{d}{dt}\sqrt{I(t)}. \tag{55}$$

The pre-factor will be summarized by X. This leads to a derivative of

$$a_f(t) = \sqrt{\frac{Z(1+R)}{2cM_i n_c}}\frac{I(t)'}{2\sqrt{I(t)}}, \tag{56}$$

when assuming a Gaussian distribution of I(t). The derivative of the laser intensity is given by $I(t)' = -\frac{8\log(2)t}{\Delta t^2}I(t)$, where Δt corresponds to the laser pulse duration (FWHM), which

can be used to resolve Eq. 56 to:

$$a_f(t) = -\sqrt{\frac{Z(1+R)}{2cM_i n_c}}\frac{8\log(2)t}{2\Delta t^2}\sqrt{I(t)}. \tag{57}$$

This leads to a dependency between the acceleration and interaction parameters such as the interaction time t, the laser intensity at this time I(t) and the pulse duration Δt, given by:

$$a_f(t) \propto \frac{t}{\Delta t^2}\sqrt{I(t)}. \tag{58}$$

This shows an increased acceleration if the laser pulse duration is shorter, or the laser intensity is increased. The point in time at which the acceleration is determined has to be taken into account as well.

Holeboring in a plasma of varying density

For this description of the holeboring velocity, I consider a spatially expanded plasma and that the initial interaction of the laser pulse with the plasma occurs at the critical density n_c. Besides the necessity that the plasma stay opaque during the whole interaction, the only requirement for the density profile is, that the function follows:

$$n_e(t) = n_e(x(t)), \text{and} \quad \frac{dn_e(x(t))}{dt} = v(t)\frac{dn_e(x(t))}{dx}, \text{whereas} \quad x(t) = \int_{-\infty}^{t} v(t')dt'. \tag{59}$$

The equation for the momentum balance between laser and ion flux is used as a starting point:

$$2n_i(t)M_i v(t)^2 = (1+R)\frac{I(t)}{c}. \tag{60}$$

The first step is to replace the ion density n_i with the electron density n_e and the corresponding charge state of the ion Z.

$$\frac{2n_e(t)}{Z}M_i v(t)^2 = (1+R)\frac{I(t)}{c} \tag{61}$$

Calculating the temporal derivative of this equation, results in:

$$\frac{2M_i c}{(1+R)Z}\left(v(t)^3\frac{dn_e(t)}{dx} + 2\frac{dv(t)}{dt}v(t)n_e(t)\right) = \frac{dI(t)}{dt}. \tag{62}$$

The electron density and the square of the velocity is factorized from the left hand side.

$$\frac{2M_i c}{(1+R)Z}v(t)^2 n_e(t)\left(v(t)\frac{1}{n_e(t)}\frac{dn_e(t)}{dx} + 2\frac{dv(t)}{dt}\frac{1}{v(t)}\right) = \frac{dI(t)}{dt} \tag{63}$$

Using Eq. 60 to replace the pre-factor with the description of the laser intensity. In addition, $\frac{1}{n_e(t)}\frac{dn_e(t)}{dx}$ is re-written as $\rho(t)$, which results in:

$$I(t)\left(v(t)\rho(t) + 2\frac{dv(t)}{dt}\frac{1}{v(t)}\right) = \frac{dI(t)}{dt}. \tag{64}$$

This can be rearranged to form a differential equation:

$$v'(t) - \frac{v(t)}{2}\frac{I'(t)}{I(t)} + v(t)^2\frac{\rho(t)}{2} = 0, \tag{65}$$

which can be reduced to a linear differential equation of the first degree, by dividing the equation with $v(t)^2$:

$$-\frac{v'(t)}{v^2(t)} + \frac{1}{2v(t)}\frac{I'(t)}{I(t)} - \frac{\rho(t)}{2} = 0, \tag{66}$$

while substituting the velocity by $\omega(t) = 1/v(t)$, which results in:

$$\omega'(t) + \omega(t)\frac{I'(t)}{2I(t)} - \frac{\rho(t)}{2} = 0 \tag{67}$$

This differential equation of the form $y' + p(t)y = q(t)$, with $p(t) = \frac{I'(t)}{2I(t)}$ can be solved using standard methods. Defining a function $\mu(p(t))$, given by:

$$\mu(t) = \exp\left(\int p(t)dt\right) = \exp\left(\int \frac{I'(t)}{2I(t)}dt\right) = \exp\left(\frac{1}{2}\ln(I(t))\right) = \sqrt{I(t)}, \tag{68}$$

helps to solve the equation. Multiplying Eq. 67 with $\mu(t)$ results in:

$$\mu(t)\omega'(t) + \mu(t)\omega(t)\frac{I'(t)}{2I(t)} - \mu(t)\frac{\rho(t)}{2} = 0 \tag{69}$$

$$\mu(t)\omega'(t) + \mu'(t)\omega(t) = \mu(t)\frac{\rho(t)}{2} \tag{70}$$

$$(\mu(t)\omega(t))' = \mu(t)\frac{\rho(t)}{2} \tag{71}$$

This equation can now be integrated and divided by $\mu(t)$, which leads to a description for $\omega(t)$:

$$\omega(t) = \frac{1}{\mu(t)}\int_{-\infty}^{t} \mu(t')\frac{\rho(t')}{2}dt' + c_1. \tag{72}$$

By resubstituting $\omega(t)$ and using the description of $\mu(t)$ and $\rho(t)$, one gets:

$$v(t) = \sqrt{I(t)}\left(\int_{-\infty}^{t} \frac{1}{2n_e(t')}\frac{dn_e(t')}{dx}\sqrt{I(t')}dt' + c_1\right)^{-1} \tag{73}$$

The constant c_1 can be found by using Eq. 60 for the found velocity:

$$\sqrt{\frac{(1+R)I(t)Z}{2cn_e(t)M_i}} = \sqrt{I(t)}\left(\int_{-\infty}^{t}\frac{1}{2n_e(t')}\frac{dn_e(t')}{dx}\sqrt{I(t')}dt' + c_1\right)^{-1} \tag{74}$$

which can be rearranged to:

$$\sqrt{\frac{2cn_e(t)M_i}{(1+R)Z}} = \int_{-\infty}^{t}\frac{1}{2n_e(t')}\frac{dn_e(t')}{dx}\sqrt{I(t')}dt' + c_1 \tag{75}$$

For $t \to -\infty$, the electron density tends towards the critical density $n_e(-\infty) = n_c$ and the constant is given by:

$$c_1 = \sqrt{\frac{2cn_cM_i}{(1+R)Z}}. \tag{76}$$

This results in the description of the holeboring velocity for an arbitrary laser intensity profile and density profile:

$$v(t) = \sqrt{I(t)}\left(\int_{-\infty}^{t}\frac{1}{2n_e(t')}\frac{dn_e(t')}{dx}\sqrt{I(t')}dt' + \sqrt{\frac{2cn_cM_i}{(1+R)Z}}\right)^{-1} \tag{77}$$

Now follows the assumption of an exponential density profile $n_e(x) = n_c\exp(\frac{x}{L_c})$, with scale length $L_c = n_e(dn_e/dx)^{-1}$, which does not change over time.

$$v(t) = \sqrt{I(t)}\left(\frac{1}{2L_c}\int_{-\infty}^{t}\sqrt{I(t')}dt' + \sqrt{\frac{2cn_cM_i}{(1+R)Z}}\right)^{-1} \tag{78}$$

A temporal derivative of the previous equation results in a description of the holeboring acceleration:

$$a(t) = L_c\frac{\frac{I'(t)}{2\sqrt{I(t)}}\left(\int\sqrt{I(t')}dt' + 2L_c\sqrt{\frac{2cn_cM_i}{(1+R)Z}}\right) - I(t)}{\left(\int\sqrt{I(t')}dt' + 2L_c\sqrt{\frac{2cn_cM_i}{(1+R)Z}}\right)^2} \tag{79}$$

These equations can be used to calculate the maximum holeboring velocity and acceleration. An example for the readout of these quantities is visible in the following. At first, one calculates the temporal velocity and acceleration evolution Eq. 78 and Eq. 79 for different scale lengths. This results in a data set, shown in Fig. A.3a and Fig. A.3b.
We take the corresponding maximum velocity and acceleration from this data set, which is indicated by the red crosses, which results in the scaling shown in Sec. 3.3.8.

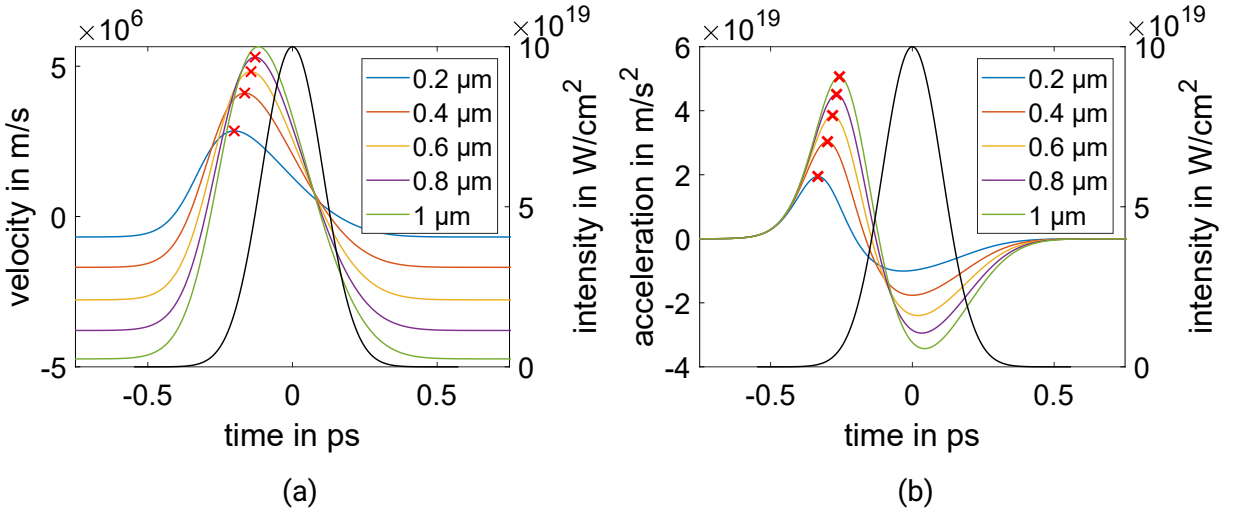

Figure A.3: Example for the calculation of velocity (a) and acceleration (b) for different preplasma scale lengths, which is used to determine the corresponding maximum values, given by the red crosses.

Characterization of the plasma mirrors

The setups for the characterization of the plasma mirrors is similar for both experiments. First, the reflectivity for different incidence angles has been measured using a continuous-wave laser with the same central wavelength as the laser pulse during the experiment of 1053 nm. For this, the power of the incoming and reflected laser beam has been measured for various incidence angles and the corresponding reflectivity calculated. The results are shown in Fig. A.4a for a single plasma mirror of experiment A and Fig. A.4b for the plasma mirror of experiment B.

The red lines correspond to the minimum and maximum angle of the incident beam during the experimental conditions, which are given by the focusing parabola for a central incidence angle on the plasma mirror of 45°. The dashed black lines show the averaged reflectivity over the whole angular range. It is visible that the averaged reflectivity in Fig. A.4a strongly increases for increasing incidence angles, reaching $\approx 8\,\%$ for the highest angle. This increases the average reflectivity to $\approx 1.6\,\%$. The high angular range of the incident beam has been considered for the second plasma mirror of experiment B, which shows a much lower average reflectivity of $\approx 0.4\,\%$, shown in Fig. A.4b. The uncertainty is quite large due to the low reflectivity and the low power of the used test laser. During the experiment, the response curve of the plasma mirror is measured for each setup. For this, the laser pulse after the interaction with the plasma mirrors was reflected by an uncoated glass plate and afterwards focused onto a calorimeter to measure the transmitted energy. This setup was cross calibrated with a direct measurement of the full beam at low energy before the glass plate to account for the corresponding losses. The energy of the laser

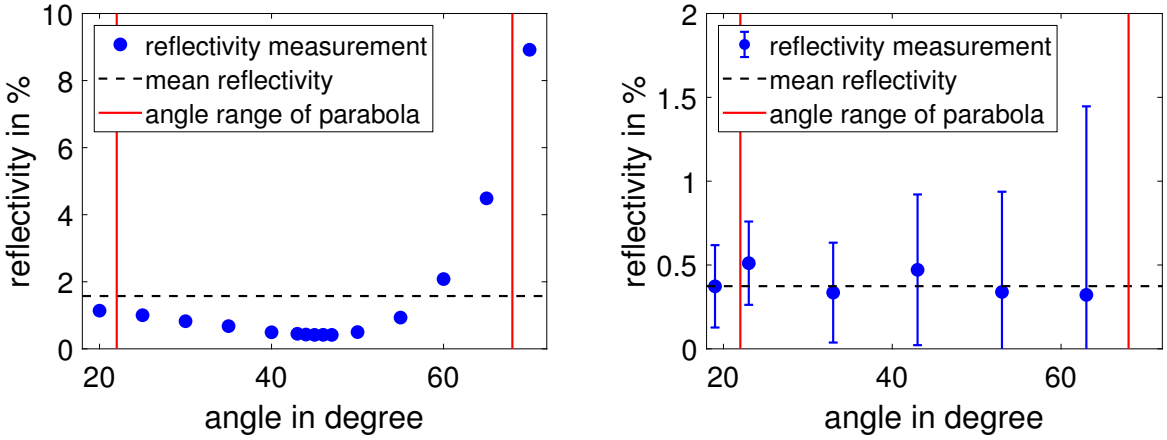

Figure A.4: Reflectivity curves for the different plasma mirrors of experiment A (a) and experiment B (b) given by the blue dots. The dashed black lines corresponds to the averaged reflectivity and the red lines show the minimum and maximum angle of incident on the plasma mirror during the experiment.

pulse was varied and the resulting transmitted energy measured. Since a double plasma mirror was used in experiment A, the laser energy was varied to measure the response instead of the laser intensity for experiment B. The result, including an error-function fit (blue), is shown in Fig. A.5a. The minimum reflectivity at low laser energy is fixed by the averaged reflectivity that was previously measured. The same procedure has been performed during the second beamtime. The resulting response curve for the different laser intensities on the plasma mirror, including the error-function fit is shown in Fig. A.5b. These fit functions are later used to determine the theoretical contrast which has been shown in Sec. 4.1.

Lesson learned

This section will introduce a short guideline for a successful time-resolved optical measurement during the laser-plasma interaction, with respect to certain key aspects. All of these tips hold apply for the measurement of the reflected light as well as the measurement of the transmitted laser pulse.

Incoming pulse

- Measure the incoming laser pulse in a time-resolved manner for similar energy conditions as during the execution of the experiment, especially when using a plasma mirror.

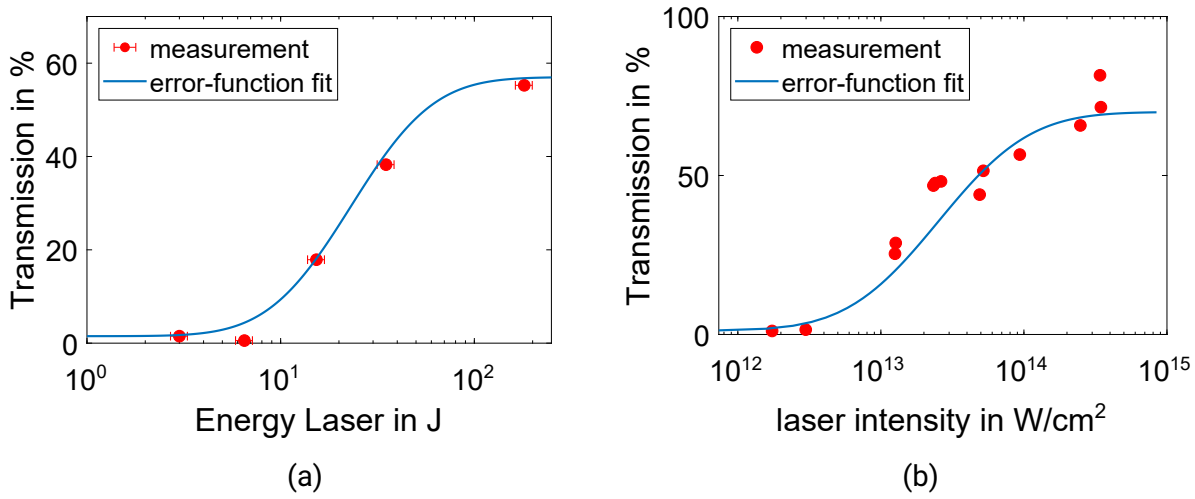

Figure A.5: Response curve of the experiment A (a) and experiment B (b) including the coresponding error-function fit.

- Ensure that the phase of the incoming laser pulse is as flat as possible, even for laser pulses with full energy and with the use of a plasma mirror.

Plasma mirror

- Design the plasma mirrors for the full range of incidence angles of the focusing parabola.

Diagnostic beamline

- Monitor the nearfield and farfield of the diagnostic beamline to trace any fluctuations of the beam path which might disturb your measurement.
- Check the stability of the imaging system by monitoring the impact of a target position or rotation change during the alignment on the measurement by your diagnostics. The near- and farfield measurement might help to identify any difficulties later on.
- Reduce the fluence of the pulse before the first transmission optics as much as possible and choose materials with a low n_2, to avoid any nonlinear effects like self-phase-modulation within the optics that further modulate the spectrum of the pulse after the interaction. This is especially important for the measurement of the incoming pulse without any target.
- Use spatial filters in the diagnostic beamline to suppress the impact of scattered light, which is critical for the time-integrated diagnostics like spectrometer.

- Use well-defined broadband spectral filters and optics and if possible characterize the whole beamline using a light source with a known broadband spectrum.

Reducing interferences

- The interaction of a high intensity laser pulse with matter produces a lot of x-rays that disturb the cameras and sensors of the optical diagnostics. Especially in the laser-propagation direction or opposing this. Therefore the diagnostics should not be placed in these directions, or should be placed outside of the laser-target-interaction level. In addition, the diagnostics should be placed as far as possible from the interaction region and shielded by lead or other heavy materials to further reduce the influence of the generated x-rays.
- The increased distance also reduced the impact of the electromagnetic pulse (EMP) that is generated during the laser-plasma interaction. The impact is also decreased by actively shielding the detectors with EMP cages. in order to reduce the EMP itself, the use of metals in the focus region should be avoided and the target, including its mount and holder, should be made out of plastics.

Ehrenwörtliche Erklärung

Ich erkläre hiermit ehrenwörtlich, dass ich die vorliegende Arbeit selbständig, ohne unzulässige Hilfe Dritter und ohne Benutzung anderer als der angegebenen Hilfsmittel und Literatur angefertigt habe. Die aus anderen Quellen direkt oder indirekt übernommenen Daten und Konzepte sind unter Angabe der Quelle gekennzeichnet.
Bei der Auswahl und Vorbereitung dieser Arbeit haben mir meine Betreuer und die Koautoren oben genannter Publikationen unentgeltlich geholfen.
Weitere Personen waren an der inhaltlich-materiellen Erstellung der vorliegenden Arbeit nicht beteiligt. Insbesondere habe ich hierfür nicht die entgeltliche Hilfe von Vermittlungs- bzw. Beratungsdiensten (Promotionsberater oder andere Personen) in Anspruch genommen. Niemand hat von mir unmittelbar oder mittelbar geldwerte Leistungen für Arbeiten erhalten, die im Zusammenhang mit dem Inhalt der vorgelegten Dissertation stehen.
Die Arbeit wurde bisher weder im In- noch im Ausland in gleicher oder ähnlicher Form einer anderen Prüfungsbehörde vorgelegt.
Die geltende Promotionsordnung der Physikalisch-Astronomischen Fakultät ist mir bekannt.
Ich versichere ehrenwörtlich, dass ich nach bestem Wissen die reine Wahrheit gesagt und nichts verschwiegen habe.

Ort, Datum Unterschrift d. Verfassers

Danksagung

Zuletzt möchte ich mich natürlich bei allen bedanken die mich während der Promotion betreut, begleitet und unterstützt haben.

Zunächst geht mein Dank an Matt, der mich in seiner Gruppe aufgenommen hat und ohne den die Ausarbeitung dieser Arbeit nicht möglich gewesen wäre. Ich bin dankbar dass er meine Arbeit, trotz des großen räumlichen Abstands, immer unterstützt hat und mir mit guten Ideen zur Seite stand.

Besonders bedanken möchte ich mich auch bei Vincent, dafür dass er durchgehend Interesse an meiner Arbeit gezeigt und mich dabei auf die best möglich Art unterstützt hat. Außerdem dafür, dass er mich auch nach meiner dritten Arbeit immer noch in seiner Arbeitsgruppe behalten möchte und mich nicht nur im Bereich der Physik, sondern auch in der kulinarischen Küche weitergebildet hat.

Ich möchte mich bei Denis bedanken, der mich bei Problemen mit dem Cluster immer beraten hat und durch die Weiterentwicklung und Fehlerbehebung des Systems die durchgeführten Simulationen überhaupt erst möglich gemacht hat.

Natürlich möchte ich mich auch bei der gesamten PHELIX-Crew bedanken, die mir immer mit Rat und Tat zur Seite stand und mich während all meinen Experimenten unterstützt und vor allem ausgehalten hat.

Mein Dank gilt auch dem gesamten Container, dafür dass die Arbeitsatmosphäre immer klasse war und das die Stimmung immer wieder mit den ein oder anderen Blödeleien oder Streichen angehoben wurde.

Natürlich auch ein extra großes danke schön an alle die mich bei dem Korrekturlesen dieser Arbeit unterstützt haben: Jonas, Kadda, Matt, Victor, Vincent, Yannik.

Ich bedanke mich bei meiner treuen Begleiterin, die mich über die ganzen Jahre, jeden Morgen aufgemuntert hat und mich selten im Stich gelassen hat. Danke liebe Kaffeemaschine.

Bei Yannik möchte ich mich vor allem für die Gainz bedanken und in diesem Zug natürlich auch bei der gesamten Meeting-Gruppe. Ohne euch wäre die Promotionszeit nicht ansatzweise so schön gewesen.

Ganz besonders möchte ich mich natürlich bei meinem Papa, meiner Mama und meiner Schwester bedanken, die mich immer auf meinem Weg unterstützt haben, ganz egal wohin er auch ging.

Zuletzt möchte ich mich bei einem ganz besonderen Menschen bedanken.
Danke Janine dass du mich all die Jahre mit voller Kraft unterstützt und mir immer zur Seite gestanden hast. Ich liebe dich.